Compound Drops

Michael James Neeson

Submitted in total fulfilment
of the requirements of the degree of
Doctor of Philosophy

February 2015

Department of Mathematics and Statistics
The University of Melbourne

Produced on archival quality paper

Abstract

Compound drops comprise two or more immiscible phases or particles that share a common interface, surrounded by a third, mutually immiscible phase. Such drops have applications in wider-ranging fields, such as soft optics, surface encapsulation, powder processing and ink deposition. In this thesis, a detailed investigation into a variety of compound drops is provided. Comparing the presented theory to experimental drop photographs facilitates the extraction of physically relevant quantities, providing important insight into the physics of compound drops.

Declaration

This is to certify that:

(i) the thesis comprises only my original work towards the PhD except where indicated in the Preface,

(ii) due acknowledgement has been made in the text to all other material used,

(iii) the thesis is fewer than 100,000 words in length, exclusive of tables, bibliographies and appendices

Michael Neeson

Preface

This work investigates the configurational behaviour of compound drops. It begins with a comprehensive theoretical analysis of these configurations, together with a series of experiments that demonstrate this behaviour. Fitting the presented theory to experimental photographs allows important physical quantities to be extracted. Based on this principle, we introduce a compound pendant drop tensiometer which provides an experimentally simple method to measure the interfacial tension for previously inaccessible regimes.

Chapters 2, 3 and 5 have previously been published, and are reproduced with permission. A reference to the relevant article is included at the beginning of each chapter. This work has been a collaboration between experimentalists and theoreticians. I performed each of these experiments under the supervision of Rico Tabor, and I derived the presented theory under the supervision of Derek Chan. Additional guidance was provided by Ray Dagastine and Franz Grieser.

The work presented in Chapter 4 discusses pendant drop tensiometry. Although this method is well known, a comprehensive derivation and discussion of the accuracy provides important additional insight.

This thesis is original, except where acknowledgements and references are made to previous work.

Acknowledgements

First and foremost, I would like to thank my supervisors. I have been extremely fortunate to have worked with such brilliant researchers. I would like to thank Derek Chan for his supervision during my undergraduate and postgraduate research. His excitement, enthusiasm and humour has made this research extremely enjoyable.

I would also like to thank Rico Tabor who has supervised my experimental work. I have really enjoyed working with him, and carrying out experiments helped my understanding enormously. I am very grateful for his guidance and mentoring both in and out of the lab.

I would like to thank my co-supervisors Ray Dagastine and Franz Grieser. I am fortunate to have had such supportive and friendly co-supervisors. I am immensely grateful for their assistance.

I gratefully acknowledge the Department of Mathematics and Statistics for providing the resources that enabled me to undertake this work, and for the staff and students who made this time so enjoyable. I am similarly thankful for the financial support provided through an Australian Postgraduate Award.

Finally, I would like to thank my family and friends for their good humour and endless encouragement. In particular, I would like to thank Nikita for her incredible support. And to my parents, I appreciate you both enormously.

Publications and conference presentations

Michael J. Neeson, Rico F. Tabor, Franz Grieser, Raymond R. Dagastine and Derek Y. C. Chan, *Compound sessile drops*, Soft Matter, 2012, **8**, 11042–11050

Michael J. Neeson, Raymond R. Dagastine, Derek Y. C. Chan and Rico F. Tabor, *Evaporation of a capillary bridge between a particle and a surface*, Soft Matter, 2014, **10**, 8489–8499

Michael J. Neeson, Derek Y. C. Chan and Rico F. Tabor, *Compound pendant drop tensiometry for surface tension measurement at zero Bond number*, Langmuir, 2014, **30**, 15388–15391

Michael J. Neeson, Raymond R. Dagastine, Rico F. Tabor and Derek Y. C. Chan, *Evaporation of a capillary bridge between a particle and a surface*, Oral presentation, ACS Colloid and Interface Symposium, University of Pennsylvania, 22–25 June 2014

Michael J. Neeson, Raymond R. Dagastine, Derek Y. C. Chan and Rico F. Tabor, *Evaporation of a capillary bridge between a particle and a surface*, Oral presentation, UK Colloids, London, 6–9 July 2014

Contents

List of Figures **xvii**

List of Tables **xxi**

1 Introduction **1**

1.1 Historical overview . . . 2
1.2 Applications and motivations . . . 4
1.3 Thesis outline . . . 5
1.4 Bibliography . . . 8

2 Compound sessile drops **13**

2.1 Introduction . . . 14
2.2 Materials and methods . . . 15
2.3 Theoretical considerations . . . 16
2.3.1 Sessile drop with a lens . . . 18
2.3.2 Sessile drop with a collar . . . 20
2.4 Results and discussion . . . 21
2.4.1 Sessile drop with total encapsulation . . . 22
2.4.2 Sessile drop with a lens . . . 23
2.4.3 Sessile drop with an evaporating collar . . . 25
2.4.4 Janus compound drops and collars . . . 28
2.5 Conclusions . . . 29
2.6 Bibliography . . . 32
2.A Mathematical details . . . 34
2.A.1 Sessile drop with a lens . . . 34
2.A.2 Sessile drop with a collar . . . 34

2.B Supplementary videos . . . 36

3 Particle–drop–substrate systems 39
3.1 Theory . . . 41
3.1.1 Spherical drop interface . . . 42
3.1.2 Axisymmetric collar . . . 44
3.1.3 Evaporation dynamics . . . 46
3.2 Materials and methods . . . 48
3.3 Results and discussion . . . 49
3.3.1 Initial configuration . . . 51
3.3.2 Boundary conditions . . . 53
3.3.3 Capillary force . . . 55
3.3.4 Evaporation dynamics . . . 57
3.3.5 Implications and opportunities for surface chemistry . . . 59
3.4 Conclusion . . . 60
3.5 Bibliography . . . 61
3.A Particle position . . . 64
3.B Supplementary videos . . . 67

4 Pendant drop tensiometry 69
4.1 Measuring interfacial tension . . . 70
4.1.1 Wilhelmy plate . . . 71
4.1.2 Du Noüy ring . . . 71
4.1.3 Maximum bubble pressure . . . 72
4.1.4 Capillary rise . . . 73
4.1.5 Spinning drop . . . 74
4.1.6 Pendant drop . . . 74
4.1.7 Summary of tensiometers . . . 75
4.2 Pendant drop tensiometry . . . 77
4.2.1 Theory . . . 77
4.2.2 Method overview . . . 79
4.2.3 Expressions for the residual vector and Jacobian matrix . . . 80
4.2.4 Pendant drop tensiometry example . . . 83
4.2.5 Limitations . . . 84
4.3 Conclusion . . . 86
4.4 Bibliography . . . 88

5 Compound pendant drop tensiometry 91
5.1 Introduction . . . 92
5.2 Theory and experiment . . . 92

5.3 Results and discussion . . . 96
5.4 Conclusion . . . 97
5.5 Bibliography . . . 99
5.A Compound pendant drop theory . . . 101
5.B Fitting experimental and theoretical profiles . . . 103
5.B.1 Image analysis . . . 103
5.B.2 Levenberg–Marquardt algorithm . . . 104
5.C Experimental details . . . 107
5.D Sensitivity . . . 107
5.E Analogy with Hookean springs . . . 108

6 Theoretical foundations **111**
6.1 Surfaces and interfaces . . . 112
6.2 Surface and interfacial tension . . . 112
6.2.1 Surface tension . . . 112
6.2.2 Interfacial tension . . . 113
6.3 The Young–Laplace equation . . . 114
6.3.1 Calculus of variations . . . 115
6.3.2 Axisymmetric Young–Laplace equation . . . 117
6.3.3 Three-phase contact conditions . . . 117
6.3.4 The Bond number and capillary length . . . 119
6.3.5 Axisymmetric Young–Laplace equation . . . 120
6.4 Fitting theory and experiments . . . 121
6.4.1 Edge detection . . . 122
6.4.2 Fitting routine . . . 122
6.4.3 Gauss–Newton algorithm . . . 123
6.4.4 Levenberg–Marquardt–Fletcher algorithm . . . 125
6.5 Bibliography . . . 129

7 Conclusion **131**
7.1 Conclusions . . . 132
7.2 Further work . . . 134
7.3 Concluding remarks . . . 135

List of Figures

2.1 Possible multiphase compound sessile drop configurations 16
2.2 Schematic representation of a lens on a sessile drop 18
2.3 Schematic representation of an axisymmetric collar formed around the base of a sessile drop 21
2.4 Experimental photographs demonstrating the fully encapsulated compound drop configuration 22
2.5 Experimental photographs demonstrating the compound drop lens configuration for two different systems 24
2.6 Interfacial energy ratio phase diagram that demonstrates the possible geometry of a compound sessile drop with a lens 25
2.7 Time-lapse images of an evaporating axisymmetric water collar around a mercury drop 26
2.8 Time-lapse images of an evaporating axisymmetric water collar around a mercury drop 26
2.9 Time variations of physical quantities associated with the water collar presented in Fig. 2.8 27
2.10 Experimental photographs demonstrating the asymmetric Janus configuration 29
2.11 Time-lapse images of an evaporating asymmetric water-mercury Janus drop 30

3.1 Schematic representation of a spherical capillary bridge between a particle and a substrate 43
3.2 Schematic representation of an axisymmetric collar around a particle substrate contact 45

3.3 Time-lapse photographs of the evaporation of an axisymmetric capillary bridges between a particle and a substrate 50
3.4 A series of experimental photographs together with the corresponding fitted drop profile for each 50
3.5 Time-lapse photographs of the evaporation of an asymmetric capillary bridge between a particle and a substrate, together with the evolution of the extracted contact radius 51
3.6 Time variations of physical quantities for three axisymmetric capillary bridges presented in Fig. 3.3 52
3.7 Time variations of physical quantities for the asymmetric capillary bridge presented in Fig. 3.5 53
3.8 Substrate contact angle evolution compared to a sessile drop 58
3.9 Schematic representation of a spherical particle attached to a drop in free space 64
3.10 Schematic illustrating integration domains to determine the system's centre of mass 65

4.1 A schematic illustrating a variety of commonly used interfacial tensiometers 70
4.2 Schematic of a pendant drop below a capillary 78
4.3 Illustration of a pendant drop that is fitted by the Young–Laplace equation 84
4.4 A schematic demonstrating the loss in sensitivity associated with pendant drop tensiometry in the low Bond number regime 85
4.5 Standard deviation of the relative error in the interfacial tension measured by the numerical routine, for varying Bond number 86

5.1 Schematic representation of a compound pendant drop deformed by gravity 93
5.2 Experimental photographs of a variety of compound pendant drops with varying volume 94
5.3 Density of the silica particle, measured from the compound pendant drop method 97
5.4 Interfacial tension for each of the four experimental systems, measured from compound pendant drop tensiometry 98
5.5 Schematic representation of a particle attached to the interface of a pendant drop 101
5.6 An example of an experimental photograph that has been fitted with the theoretical solution presented 104

5.7 Illustration of the residuals used to fit the theoretical profile to experimental data . . . 105
5.8 An illustration of the sensitivity of the compound pendant drop tensiometer compared to the conventional pendant drop tensiometer . . 108

6.1 Schematic of the interface between two phases . . . 112
6.2 Schematic of the intermolecular forces within a condensed liquid phase 113
6.3 Schematic of an axisymmetric drop deposited on a surface, surrounded by a continuous phase . . . 114
6.4 Schematic of the three-phase contact between three mutually immiscible fluid interfaces . . . 119
6.5 A schematic illustrating the principal radii of curvature for an axisymmetric drop . . . 121
6.6 Schematic illustrating the residuals that are minimised in the optimisation routine . . . 123
6.7 Flow chart for the Levenberg–Marquardt–Fletcher algorithm . . . 128

List of Tables

2.1 Specific gravity, refractive index and interfacial tensions of fluids used in making compound sessile drops 22

3.1 Diffusion rate parameters used in modelling droplet evaporation rate 57

4.1 Summary of methods commonly used to measure surface and interfacial tension 76

CHAPTER 1

Introduction

This thesis provides a comprehensive investigation into multiphase droplet systems, known as compound drops. When these drops are immobilised on a solid surface, they can form a variety of different configurations, depending on the interfacial tensions, densities and volumes of the phases involved.

Compound drops formed from continuous phases have applications in surface encapsulation, drug delivery vehicles and soft lenses, while particle-drop composites are relevant to powder processing, ink deposition and, as developed in this thesis, interfacial tensiometry.

This chapter begins with a discussion of the early historical developments that led to our understanding of the physics and geometries of immiscible fluid interfaces. We then motivate the current work by introducing compound drops and discussing the associated applications, before providing a thesis outline.

1.1 Historical overview

The first accurate scientific experiments into capillary related phenomena were performed over three centuries ago when, in 1706, Francis Hauksbee (appointed by Isaac Newton as an experimentalist for the Royal Society) demonstrated that the capillary rise of water within a small capillary tube was the same in a vacuum as in air [1]. Over the next decade Hauksbee performed a series of important experiments into capillary action.

Although the capillary rise of a liquid inside a thin tube was well known (Leonardo da Vinci investigated the phenomena two centuries earlier [2]), Hauksbee set about systematically studying the phenomena. He showed capillary rise to occur between two parallel glass plates (showing the phenomena was not specific to the cylindrical geometry), and that the effect was still present for differing liquids (alcohol and oils) and surfaces (marble and brass). Most importantly, he showed that the height that a fluid rises within a capillary was the same for two capillary tubes of equal inner diameter, but with one *"at least ten times as thick as the other"*. This, he argued, demonstrated that the attraction is limited to a very small region near the surface of the solid [3].

In a letter to the Secretary of the Royal Society, Brook Taylor, who later developed the Taylor series, investigated the capillary rise between two glass planes inclined at a slight angle to each other. By marking the shape the meniscus formed on the glass, he noted *"it seems to approach very near to the common Hyperbola. But my apparatus was not nice enough to discover this exactly"* [4]. Hauksbee repeated this experiment, confirming Taylor's earlier hypothesis [5, 6, 7].

Following the pioneering work of Hauksbee, Jurin [8] further investigated capillary rise. Later, Segner [9] introduced the concept of surface tension. In addition, he considered the curvature of the meridian of the surface, but neglected to consider the curvature perpendicular to it. Just after the turn of the 19th century, Leslie [10] provided the first correct explanation for the capillary rise within a tube. Importantly he did not suppose the capillary force to act vertically, but rather to act perpendicular to the liquid surface. Almost a century after Hauksbee's initial experiments the British polymath Thomas Young provided the first accurate theoretical account of capillarity.

On December 20, 1804, Young read a paper to the Royal Society which laid the theoretical foundations for the shape of a fluid interface [11]. In addition, he observed that the contact angle formed between a liquid and a solid is a property of the liquid and the solid involved (the Young–Dupré equation), as well as derived the governing equation for the shape of an immiscible fluid interface (the Young–Laplace equation) from a force balance between the pressure and surface tension.

His derivation notably omits the use of any equations. James Clerk Maxwell's entry on Capillary Action in Encyclopædia Britannica [12] remarked of Young,

> *"his methods of demonstration, though always correct, and often extremely elegant, are sometimes rendered obscure by his scrupulous avoidance of mathematical symbols."*

The following year, the French mathematician Pierre-Simon Laplace published the fourth volume of his five-volume treatise Mécanique Céleste [13], in which he too gave a derivation of the same equation as provided by Young. However unlike Young's earlier work, Laplace's approach was entirely mathematical.

Following the earlier work of Young and Laplace, the German mathematician Carl Friedrich Gauss derived the same result by minimising the free energy of a volume of fluid [14]. In addition to the Young–Laplace equation, his derivation showed that the global minimum energy occurs when the Young–Dupré equation is also satisfied.

The second half of the 19th century saw an explosion in the depth and breadth of investigations into surface related phenomena.

In 1873, the Belgian experimentalist Joseph Plateau provided a comprehensive investigation into the shape of immiscible fluid interfaces [15]. Plateau formed a mixture of alcohol and water with a density that matched that of olive oil. By creating an oil drop in this mixture, he was able to eliminate the effects of gravity. This allowed him to create immiscible fluid interfaces of significant size. Since gravity no longer affects the shape of the drop the interfacial tension results in the drop forming a sphere. By placing a solid (either a wire ring or a disk) into the tank that the oil adhered to, he was able to investigate the various geometries the drop can assume under interfacial tension alone [15]. Impressively, Plateau was blind during these experiments [12].

Francis Bashforth and John Adams numerically investigated the shape of an axisymmetric drop. Bashforth provided a scaling of the axisymmetric Young–Laplace equation, showing that the shape of an interface depended on a single 'shape' parameter. Adams developed a numerical routine to solve this differential equation, based on Taylor series expansions, from which they compiled (by-hand) extensive tables for the drop shapes for different Bond numbers [16].

Around this time, physicists were beginning to explain physical systems according to thermodynamic principals. In 1878, J. Willard Gibbs published a thermodynamic derivation the Young–Laplace equation by minimising the 'available energy' (now known as the Gibbs free energy) associated with two phases [17, 18]. Soon after this work, the Dutch physicist Johannes Diderik van der Waals considered the attractive intermolecular forces in an attempt to explain why gases do not obey the

ideal gas law [19], leading to the van der Waals equation of state, and ultimately to van der Waals forces.

The work outlined above forms the basis of the classical ideas of interfaces that are investigated in this thesis. Several detailed, and very interesting, historical accounts on capillarity can be found, including [2, 12, 20, 21].

1.2 Applications and motivations

Throughout this thesis we investigate compound drops comprised of two immiscible phases, surrounded by a third mutually immiscible phase. The discussion focuses on two different compound drops. The first class of drops is formed from two immiscible fluid phases, while in the second we consider compound drops where one of the fluid phases has been replaced by a solid spherical particle. We now provide a discussion of the applications and motivations of this study.

The geometry of a compound drop is determined via a minimisation of the total energy of the compound drop system [2], which is the sum of the interfacial energy and the gravitational energy. When these drops are sufficiently small, the interfacial forces dominate the gravitational forces, resulting in an interface that is not deformed by gravity.

Compound drops formed from two fluid phases, surrounded by a third, mutually immiscible liquid are often referred to as multiple emulsions [22], or 'Janus droplets' [23, 24], while drops surrounded by a vapour phase are known as aerosol droplets.

When these drops are formed in free space, the resulting geometry can be determined from a relatively straightforward application of the Young–Laplace equation [23, 25, 26, 27, 28, 29]. This allows the geometry of a given compound drop to be expressed in terms of the relative interfacial tensions and drop volumes.

When one of the drop volumes is smaller than the other volume, the smaller drop forms a liquid lens which shares similarities with a lens formed at a planar fluid interface [30, 31, 32]. The shape of this lens is largely dependant on the local geometry of the three-phase contact line [30]. Finally, the case where one drop is completely engulfed by another is a particular case of these compound drops. The drops are known as double emulsions. Such emulsions are important in functionalised foods and cosmetic products [33].

A related class of compound drops are formed when a fluid phase partially engulfs a solid spherical particle, with this drop in turn surrounded by an outer immiscible phase. These particle-drop composites are important to a variety of diverse areas, from particle adsorption to capillary bridges.

In the limit where the particle radius is much larger than the drop radius, these

configurations share similarities with Ramsden or Pickering emulsions [34, 35] and liquid marbles [36, 37, 38], where many small particles are adsorbed at a liquid interface to provide stability [39, 40].

The opposing limit, where the volume of liquid is much smaller than the particle, is of interest in understanding capillary bridges. When a small capillary bridge is formed between two solid surfaces, such as a particle and a surface, the capillary bridge exerts a strongly attractive capillary force between the two surfaces. This capillary force is important in the study of particle adhesion [41, 42, 43].

These capillary bridges are also important in understanding water retention in granular media [44, 45] and powder processing [46, 47]. Furthermore, when a small amount of liquid is added to dry particles, capillary bridges are able to form large networks that greatly affect the associated rheological behaviour [48].

The configurational behaviour of compound drops depends greatly on the geometry of the three-phase contact line. This geometry is defined in terms of the interfacial tensions associated with each of the three interfaces. Thus, the magnitudes of the associated interfacial tensions are of critical importance.

One method to measure the interfacial tension is the pendant drop tensiometer. In this technique the interfacial tension is determined by measuring the gravitational deformation of a pendant drop, and matching that to a solution of the Young–Laplace equation, from which the interfacial tension can be determined. This idea was first presented well over a century ago [49, 50, 51], however quantifying the Bond number proved difficult.

Half a century later, Andreas *et al.* [52] developed a simple method based on the ratio of two easily measured quantities. Computational routines have since been developed to perform this fitting routine automatically [53, 54, 55, 56]. However, when the interfacial forces dominate gravitational forces, the sensitivity of the method greatly decreases.

This work provides an in-depth analysis of the configurational behaviour associated with the compound drops discussed here. In addition, we show that these drops offer an important extension to pendant drop tensiometry that circumvents the limitation outlined above.

1.3 Thesis outline

This thesis investigates the configurational behaviour of a variety of compound drop systems. In each case, we develop the theoretical framework necessary to analyse and quantify experimental observations.

The first two chapters provide a comprehensive theoretical and experimental discussion of compound drops in the limit where interfacial forces dominate gravi-

tational forces.

In Chapter 2, we investigate compound drops immobilised on a solid surface. The theoretical discussion begins by outlining four possible drop configurations. We then proceed to derive the theory associated with each configuration, before comparing the theory to a series of experimental drops. Importantly, we demonstrate that even when the interfacial forces dominate gravitational forces, gravity plays a crucial role in determining the compound drop configuration.

Chapter 3 investigates a related system formed when a particle is added to the interface of a pendant or sessile water drop. This forms a capillary bridge between the particle and the surface. As in the previous chapter, we outline the possible configurations that the particle-drop composite can assume, and then derive the theoretical drop shape associated with each. We investigate the volume dependence of the resulting configuration by allowing the water to slowly evaporate. As before, gravity is shown to play a crucial role in determining the resulting configuration, which we further demonstrate through surface orientation.

When a three-phase contact line is formed, the resulting geometry depends on the magnitudes of each of the associated interfacial tensions. The local geometry of the three-phase contact line is particularly important in the study of compound drops since, as shown in Chapter 2 and Chapter 3, this greatly affects the resulting configuration. In addition, the interfacial tension is a fundamental quantity that is important throughout physical chemistry. The next chapter discusses the measurement of this quantity.

Chapter 4 begins with a description of a variety of methods commonly used in interfacial tensiometry, together with a summary of these methods. One of these techniques, pendant drop tensiometry, is particularly appealing as it is accurate, widely applicable and experimentally straightforward. For the remainder of this chapter, a comprehensive derivation of this method is presented.

While the pendant drop method is appealing, a fundamental physical limitation of the method occurs when the interfacial forces dominate gravitational forces. To circumvent this, Chapter 5 extends the technique by attaching a particle to the interface of a pendant drop. The theoretical framework presented allows the interfacial tension to be accurately determined. We demonstrate the applicability of this method for a series of experimental systems.

Chapter 6 presents a supplementary chapter that discusses the theoretical foundations associated with this study. The intention of this chapter is to provide additional details to aid the reader, however it is not essential to understanding the thesis. This chapter discusses several important aspects associated with the physics of interfaces, and provides a derivation of the Young–Laplace equation from a calculus of variations.

The second part of the chapter provides a comprehensive discussion of the fitting routines used throughout this thesis. These routines allow the theoretical drop profiles presented to be fitted to experimental drop photographs, which in turn allows physical quantities to be extracted from experimental photographs.

Finally, Chapter 7 concludes the thesis with a discussion and conclusion of the presented work.

1.4 Bibliography

[1] F. Hauksbee, *Phil. Trans.*, 1706, **25**, 2223–2224.

[2] P. G. de Gennes, F. Brochard-Wyatt and D. Quere, *Capillarity and Wetting Phenomena - Drops, Bubbles, Pearls, Waves*, Springer, New York, 2004.

[3] F. Hauksbee, *Phil. Trans.*, 1708, **26**, 258–266.

[4] B. Taylor, *Phil. Trans.*, 1710, **27**, 538–538.

[5] F. Hauksbee, *Phil. Trans.*, 1710, **27**, 539–540.

[6] F. Hauksbee, *Phil. Trans.*, 1713, **28**, 151–152.

[7] F. Hauksbee, *Phil. Trans.*, 1713, **28**, 153–154.

[8] J. Jurin, *Phil. Trans.*, 1718, **30**, 739–747.

[9] J. A. Segner, *Comm. Soc. Reg. Sci. Göttingensis*, 1751, **1**, 301–372.

[10] J. Leslie, *Philos. Mag.*, 1802, **14**, 193–205.

[11] T. Young, *Phil. Trans.*, 1805, **95**, 65–87.

[12] J. C. Maxwell, *Encyclopædia Britannica*, 1876, **5**, 56–71.

[13] P. S. Laplace, *Traité de Mécanique Céleste*, de l'Imprimerie de Crapelet, 1805, vol. 4.

[14] C. F. Gauss, *Principia generalia Theoriae Figurae Fluidorum in statu Aequilibrii*, Göttingen, Dieterichs, 1830.

[15] J. Plateau, *Statique Expérimentale et Théorique des Liquides Soumis aux Seules Forces Moléculaires*, Gauthier-Villars, Paris, 1873.

[16] F. Bashforth and J. C. Adams, *An attempt to test the theories of capillary action: by comparing the theoretical and measured forms of drops of fluid*, University Press, 1883.

[17] J. W. Gibbs, *Trans. Conn. Acad. Arts Sci.*, 1974–1978, **3**, 343–520.

[18] J. W. Gibbs, *The Collected Works of J. Willard Gibbs*, Longmans, Green and Company, 1928, vol. 1.

[19] J. D. van der Waals, *Z. Phys. Chem. Leipzig*, 1894, **13**, 657–725.

[20] J. Challis, *British Association for the Admancement of Science*, 1834, 253–294.

[21] W. Hardy, *Nature*, 1922, **109**, 375–378.

[22] R. E. Johnson and S. S. Sadhal, *Ann. Rev. Fluid Mech.*, 1985, **17**, 289–320.

[23] J. Guzowski, P. M. Korczyk, S. Jakiela and P. Garstecki, *Soft Matter*, 2012, **8**, 7269–7278.

[24] T. Nisisako and T. Torii, *Adv. Mater.*, 2007, **19**, 1489–1493.

[25] S. Torza and S. G. Mason, *J. Colloid Interface Sci.*, 1970, **33**, 67–83.

[26] M. Aratono, T. Toyomasu, N. Ikeda and T. Takiue, *J. Colloid Interface Sci.*, 1999, **218**, 412–422.

[27] Y. Shao and T. G. M. van de Ven, *Langmuir*, 1989, **5**, 1234–1241.

[28] O. M. Lavrentevea, L. Rosenfeld and A. Nir, *Phys. Rev. E*, 2011, **84**, 056323.

[29] L. Rosenfeld, O. M. Lavrentevea and A. Nir, *J. Fluid Mech.*, 2009, **626**, 263–289.

[30] R. Aveyard and J. H. Clint, *J. Chem. Soc., Faraday Trans.*, 1997, **93**, 1397–1403.

[31] J. C. Burton, F. M. Huisman, P. Alison, D. Rogerson and P. Taborek, *Langmuir*, 2010, **26**, 15316–15324.

[32] C. M. Phan, B. Allen, L. B. Peters, T. N. Le and M. O. Tade, *Langmuir*, 2012, **28**, 4609–4613.

[33] D.-H. Lee, Y.-M. Goh, J.-S. Kim, H.-K. Kim, H.-H. Kang, K.-D. Suh and J.-W. Kim, *J. Disp. Sci. Technol.*, 2002, **23**, 491–497.

[34] S. U. Pickering, *J. Chem. Soc., Trans.*, 1907, **91**, 2001–2021.

[35] W. Ramsden, *Proc. R. Soc. Lond.*, 1903, **72**, 156–164.

[36] P. Aussillous and D. Quéré, *Nature*, 2001, **411**, 924–927.

[37] E. Bormashenko, *Curr. Opin. Colloid Interface Sci.*, 2011, **16**, 266–271.

[38] G. McHale and M. I. Newton, *Soft Matter*, 2011, **7**, 5473–5481.

[39] R. Aveyard, B. D. Beake and J. H. Clint, *J. Chem. Soc., Faraday Trans.*, 1996, **92**, 4271–4277.

[40] S. Komura, Y. Hirose and Y. Nonomura, *J. Chem. Phys.*, 2006, **124**, 241104.

[41] J. S. McFarlane and D. Tabor, *Proc. R. Soc. Lond. A*, 1950, **202**, 224–243.

[42] H. Schubert, *Powder Technol.*, 1984, **37**, 105–116.

[43] Y. I. Rabinovich, J. J. Adler, M. S. Esayanur, A. Ata, R. K. Singh and B. M. Moudgil, *Adv. Colloid Interface Sci.*, 2002, **96**, 213–230.

[44] T. K. Tokunaga, *Water Resour. Res.*, 2011, **47**, 8514.

[45] R. K. Niven, *J. Pet. Sci. Eng.*, 2006, **52**, 1–18.

[46] Z. Fournier, D. Geromichalos, S. Herminghaus, M. Kohonen, F. Mugele, M. Scheel, M. Schulz, B. Schulz, C. Schier, R. Seemann and A. Skudelny, *J. Phys. Condens. Matter*, 2005, **17**, S477.

[47] C. Gögelein, M. Brinkmann, M. Schröter and S. Herminghaus, *Langmuir*, 2010, **26**, 17184–17189.

[48] N. Mitarai and F. Nori, *Adv. Phys.*, 2006, **55**, 1–45.

[49] A. M. Worthington, *Proc. R. Soc. Lond.*, 1881, **32**, 362–377.

[50] A. M. Worthington, *Philos. Mag.*, 1885, **19**, 46–48.

[51] A. Ferguson, *Philos. Mag.*, 1911, **23**, 417–430.

[52] J. M. Andreas, E. A. Hauser and W. B. Tucker, *J. Phys. Chem.*, 1938, **42**, 1001–1019.

[53] Y. Rotenberg, L. Boruvka and A. W. Neumann, *J. Colloid Interface Sci.*, 1983, **93**, 169–183.

[54] C. Huh and R. L. Reed, *J. Colloid Interface Sci.*, 1983, **91**, 472–484.

[55] J. W. Jennings and N. R. Pallas, *Langmuir*, 1988, **4**, 959–967.

[56] O. I. del Río and A. W. Neumann, *J. Colloid Interface Sci.*, 1997, **196**, 136–147.

CHAPTER 2

Compound sessile drops

Compound drops arise from the contact of three immiscible fluids and can assume various geometric forms based on the interfacial chemistry of the phases involved. Here we present a study of a new class of compound drops that is sessile on a solid surface. The possible geometries are demonstrated experimentally with appropriate fluid combinations and accounted for with a quantitative theoretical description. Although such systems are broadly controlled by relative interfacial energies, subtleties such as the van der Waals force and effects of micro-gravity, despite drop sizes being well below the capillary length, come into play in determining the equilibrium state that is achieved. The drying of a compound sessile drop was measured experimentally, and the process revealed a novel transition between different characteristic configurations of compound sessile drops. Such drops may prove useful for the development of functional surfaces in applications such as soft optics, photonics and surface encapsulation.

This chapter has been published as Michael J. Neeson, Rico F. Tabor, Franz Grieser, Raymond R. Dagastine and Derek Y. C. Chan, *Compound sessile drops*, Soft Matter, 2012, **8**, 11042–11050 — Reproduced by permission of The Royal Society of Chemistry.

2.1 Introduction

Compound or multiphase drops comprise two (or more) immiscible fluid drops that share an interface with one another, surrounded by a third, mutually immiscible fluid. In the case of free drops surrounded by a liquid, they are often referred to as multiple emulsions [1], whereas in a continuous vapour phase they are aerosol droplets. Such drops exist in areas as diverse as multiphase processing, biological interactions within cells and atmospheric chemistry. The geometry of such states at equilibrium is dictated by minimisation of the interfacial energy of the system as a whole [2]. In some cases, one phase may be totally engulfed by another, whereas in others, an asymmetric geometry may result, recently termed 'Janus droplets' [3, 4]. Such systems are further complicated by the possibility of local minima in interfacial energy states causing history-dependent geometries to become available, particularly if surface forces are involved in the assembly of drops to form compound bodies. The concept of multiphase droplet systems has been of interest, initially as a curiosity for almost a hundred years [5], but recent developments in droplet handling have re-kindled research into these compound drops [6, 7, 8].

Multiple emulsions, a special case of compound drops where the internal phase is entirely engulfed by an outer droplet [1, 9], have gained considerable attention due to their potential uses in functionalised foods, pharmaceutical formulations and drug delivery vehicles [10]. The advent of microfluidics has provided a particularly adventitious platform for generating multiple emulsions under well-controlled conditions, providing highly monodisperse and regular systems for synthesis of core-shell particles, for instance, and in other applications [6, 7, 8].

The theoretical description of such multiphase systems share similarities with the case of a floating liquid lens at the air-water interface [11, 12, 13]. A large number of studies have dealt with this problem experimentally and theoretically. A complete description of lenses at planar fluid interfaces has been given by Aveyard [11]. However, by adding curvature to the supporting interface, such as a lens on a droplet or similar configuration, additional complexity arises. Of the few available studies that considered such systems, invariably the case of free drops has been considered, wherein the compound drops are entirely surrounded by the continuous phase fluid [3, 14, 15, 16, 17]. In such a scenario, describing the geometry of equilibrium states becomes a comparatively simple solution of the Young-Laplace equation that accounts for the relative energies of the interfaces and drop volumes.

In this chapter, we present a new class of small compound drops that are immobilised on planar solid substrates. The equilibrium drop shapes are now complicated by the drop-substrate contacts, and hence a larger range of geometries can exist depending on the surface chemistry of the solid-fluid and fluid-fluid interfaces involved,

as well as the volume ratios and density differences of phases. In our regime of interest, the dimensions of the drops are well below their capillary length, so the shapes of the interfaces are unaffected by gravity. Nonetheless, because of differences in fluid densities, micro-gravity effects still play a role in determining the minimum energy configurations of such compound sessile drops. Indeed, this is a unique circumstance wherein van der Waals forces of quantum mechanical origin compete with the gravitational force to determine soft structures on a micro- to nano-scale. A theoretical model is developed that can account for the geometries that are observed experimentally, and that offers insight into 'design rules' for obtaining compound sessile drops from common material combinations. By observing the evaporation dynamics of a compound water/mercury drop on a surface, competition between fluid-fluid and fluid-solid interfacial energies is seen, the balance of which determines the configuration of the compound drop. Such drops may have interesting properties as tuneable micro-lenses for the modification of interfacial photonic properties, as well as providing a unique system to interrogate evaporation dynamics, which is fundamental to the novel technique of evaporative lithography [18, 19].

Herein, we give a brief description of possible compound sessile drops on a planar substrate and introduce the theoretical framework required to provide quantitative descriptions of such drops in Section 2.3. Examples of experimental realisations of different characteristic compound sessile drops are given in Section 2.4. These are chosen to be at key locations of the drop parameter phase diagram that would be useful in the design of specific drop configurations. We also explore compound drops where one liquid phase can evaporate and, in doing so, cause a transition between two pseudo-equilibrium drop configurations. Additional experimental result and ancillary details are given in the Appendix.

2.2 Materials and methods

Water was obtained from a Milli-Q system (minimum resistivity 18.2 MΩ cm). Perfluorooctane (PFO), tetradecane (TD) and 1-bromodecane (BD), all 99% purity, were obtained from Sigma and purified by column chromatography over silica (Florisil, also from Sigma). Mercury metal (99.9%) was obtained from Sigma and used as received.

Experiments were arranged and observed using an inverted microscope (Nikon Te-2000), and images from the side were obtained by using a 1.5 mm right-angle prism (MCPH-1.5, Tower Optical) that was placed on the substrate. Diffuse illumination was provided using a white LED light source and a diffuser. This setup allowed visualisation of drops from either a side-on perspective or from below by simply changing the focus position of the microscope. Drops were formed on three

types of glass substrates, that were functionalised to provide desired surface chemical properties: (i) treatment in 10% HNO_3 rendered the glass highly *hydrophilic* (water contact angle in air $< 10°$); (ii) boiling in ethanol for 4 hours made them *semi-hydrophobic* (water contact angle in air $\sim 20°$) and (iii) immersion in a 1% OTS solution in heptane for 30 minutes made the glass *hydrophobic* (water contact angle in air $\sim 95°$). Surface and interfacial tension measurements were carried out using a standard drop-shape tensiometer.

Compound drops were prepared by depositing an initial sessile droplet on the substrate using glass syringes (10 µL, Hamilton Corp.) and then adding another drop or bubble either directly with the syringe or *via* an atomic force microscope (AFM) cantilever. The AFM used was an Asylum Research MFP-3D, and the cantilevers used were specially fabricated to enable facile capture of bubbles and droplets. This process has been described in detail previously [20, 21, 22] and so is not reproduced here. Photographs of the drops were taken using a digital CCD camera, and image analysis and fitting were performed using the Wolfram *Mathematica* software.

2.3 Theoretical considerations

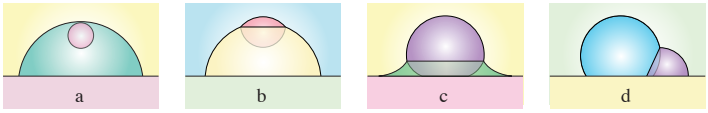

Figure 2.1: Configurations of compound sessile drops: (a) encapsulated, (b) lens, (c) collar and (d) Janus drops. The colouring scheme of different phases is simply to provide visual contrast.

We consider surface-immobilised compound sessile drops resting on a planar solid substrate as illustrated in Fig. 2.1. The compound sessile drop comprised of phases 2 and 3 is surrounded by a continuous fluid phase 1, above the substrate. Clearly such configurations are possible only if the three interfacial tensions γ_{ij} satisfy the triangular inequality

$$\gamma_{ij} < \gamma_{jk} + \gamma_{ki} \tag{2.1}$$

for all cyclic permutations of the indices $\{i, j, k\} = \{1, 2, 3\}$ in order for the 3-phase contact line to form. There are four cases that we will consider:
(a) A small drop is entirely encapsulated within a large sessile drop (Fig. 2.1a). The small drop is less dense than the sessile phase so that the buoyancy force will position it at the apex of the sessile drop where it is separated from the outer phase by a thin film of the sessile fluid.
(b) A small drop forms a lens on the top of the sessile drop with a three-phase

contact line between all three fluids (Fig. 2.1b). Again, buoyancy force positions the lighter lens at the apex of the sessile drop. If the lens dimensions are small compared to the radius of the sessile drop, this case is similar to a drop resting on a planar interface studied by Aveyard and Clint [11].
(c) A sessile drop with an axisymmetric pendular ring or collar of another fluid around it at the base [23] (Fig. 2.1c).
(d) A sessile Janus drop in contact with the substrate in an asymmetric configuration (Fig. 2.1d).

The configurations in Fig. 2.1a-c are axisymmetric. As the case in Fig. 2.1a does not contain intersecting interfaces, the small inner drop is spherical and the shape of the outer sessile drop is a portion of the spherical cap.

To describe the compound sessile drops in Fig. 2.1b and c, we identify the interfacial tension γ_{ij} of the ij-interface ($i, j = 1, 2, 3$, see Fig. 2.2 and 2.3) and the corresponding capillary length $\lambda_{ij} = \sqrt{\gamma_{ij}/\Delta\rho_{ij}\, g}$, where $\Delta\rho_{ij}$ is the density difference between the phases and g is the gravitational acceleration. For the fluid systems we consider here, $\lambda_{ij} \gtrsim 2$ mm,whereas a typical length scale L for the drops we shall consider is $L \simeq 150\mu$m, which gives corresponding Bond numbers $B_{ij} \equiv (L/\lambda_{ij})^2 \simeq 0.01 \ll 1$. This implies that the effects of gravity may be omitted when considering the equilibrium shapes of the interfaces of the immiscible fluids in Fig. 2.1. The shape of each interface is determined by the Young–Laplace equation, which relates the local mean curvature to the pressure difference across the interfaces

$$\gamma_{ij}\left(\frac{1}{R_1}+\frac{1}{R_2}\right) = P_j - P_i \equiv \Delta P_{ij} \tag{2.2}$$

with R_1 and R_2 representing the principal radii of curvature.

Using cylindrical coordinates, the axisymmetric fluid interfaces in Fig. 2.1b and c can be described by their height $z(r)$ above the substrate. The Young–Laplace equation for each interface can be written as

$$\frac{\gamma}{r}\frac{\mathrm{d}}{\mathrm{d}r}\left(r\sin\phi\right) = \Delta P \equiv \frac{2\gamma}{R} \tag{2.3a}$$

$$\tan\phi = \frac{\mathrm{d}z}{\mathrm{d}r} \equiv z'(r) \tag{2.3b}$$

where R denotes the Laplace radius of the interface and ϕ is the tangent angle.

We now derive the boundary conditions for the axisymmetric cases in Fig. 2.2 and 2.3.

2.3.1 Sessile drop with a lens

A detailed view of the axisymmetric compound sessile drop with a lens at the apex is given in Fig. 2.2. Each of the three interfaces satisfy the Young–Laplace equation, eqn (2.3), a second order differential equation that requires two boundary conditions plus one further condition to determine the pressure difference, ΔP or equivalently the Laplace radius, R. Thus all together, 9 conditions are required to determine the shape of the compound sessile drop.

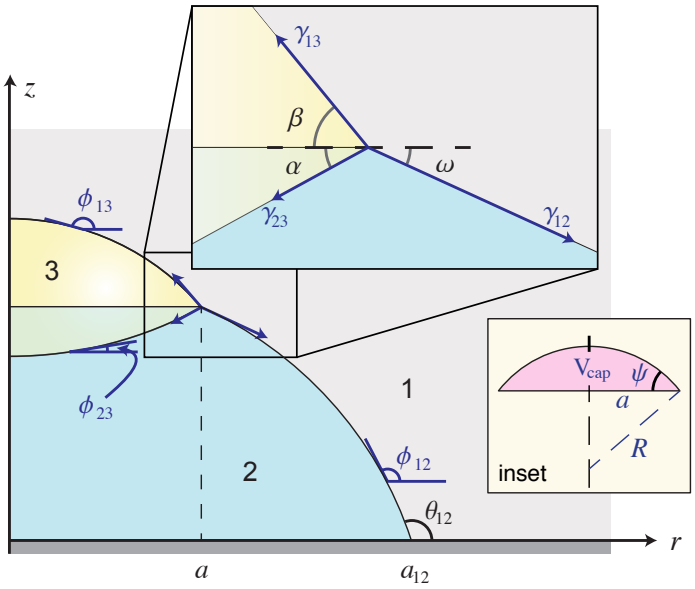

Figure 2.2: A schematic representation of the three-phase contact region of a lens on a sessile drop comprising 3 mutually immiscible fluids with interfacial tensions γ_{12}, γ_{23} and γ_{13}. Inset: A spherical cap of volume V_{cap} with base radius a and subtends an angle ψ.

The symmetry conditions of the 12- and 23-interfaces at $r = 0$ and that the 12-interface meets the substrate at a prescribed contact angle θ_{12} at position $r = a_{12}$ give three conditions

$$z'_{13}(0) = 0 \tag{2.4a}$$

$$z'_{23}(0) = 0 \tag{2.4b}$$

$$z'_{12}(a_{12}) = \tan\theta_{12}. \tag{2.4c}$$

The conditions in eqn (2.4a) and (2.4b) imply that the 13- and 23-interfaces are spherical caps of radii R_{13} and R_{23}, respectively. Balancing the components of the interfacial tension in the directions parallel and normal to the 12-interface at the 3-phase contact line at $r = a$ gives two equations that are equivalent to the Neumann

triangle condition:

$$\gamma_{13}\cos(\beta-\omega)+\gamma_{23}\cos(\alpha+\omega)=\gamma_{12}$$
$$\gamma_{13}\sin(\beta-\omega)-\gamma_{23}\sin(\alpha+\omega)=0.$$

These equations can be solved to give

$$\cos(\alpha+\omega)=(1+x^2-y^2)/2x \tag{2.6a}$$
$$\cos(\beta-\omega)=(1+y^2-x^2)/2y \tag{2.6b}$$

where $x\equiv\gamma_{23}/\gamma_{12}$, $y\equiv\gamma_{13}/\gamma_{12}$. Thus, given the interfacial tensions, these equations allow, for example, the angles β and ω to be expressed in terms of α and the interfacial tensions. The value $\alpha=0$ corresponds to a lens with a planar 23-interface.

Since the change in pressure in crossing the 12- and 23-interfaces is equal to the pressure drop across the 13-interface, we have

$$\Delta P_{12}+\Delta P_{23}=(P_2-P_1)+(P_3-P_2)=P_3-P_1=\Delta P_{13}.$$

Writing this in terms of the Laplace radii gives

$$\gamma_{12}/R_{12}+\gamma_{23}/R_{23}=\gamma_{13}/R_{13}. \tag{2.7}$$

In the absence of gravity, the net normal force F exerted by the compound sessile drop on the substrate must vanish. This force is the sum of a downward pressure acting over the base area of the drop and an upward interfacial tension force acting around the perimeter of the base at $r=a_{12}$ where the 12-interface meets the substrate. This condition can be expressed as:

$$\begin{aligned}F&=\left(\pi a_{12}^2\right)(\Delta P_{12})-(2\pi a_{12})(\gamma_{12}\sin\theta_{12})\\&=2\pi\,\gamma_{12}\,a_{12}\left[\frac{a_{12}}{R_{12}}-\sin\theta_{12}\right]=0\end{aligned} \tag{2.8}$$

and implies that the 12-interface is also a portion of the sphere of radius R_{12} (see Appendix 2.A.1).

Eqn (2.4)–(2.8) provide 7 conditions and the final 2 conditions follow from specifying the volumes of the two phases to be V_2 and V_3. In this configuration, the

shapes of all the interfaces are portions of spherical caps. This therefore gives

$$V_2 = a^3 \left[\left(\frac{\sin\theta_{12}}{\sin\omega} \right)^3 v(\pi - \theta_{12}) - v(\omega) \mp v(\alpha) \right] \tag{2.9a}$$

$$V_3 = a^3 \left[v(\beta) \pm v(\alpha) \right] \tag{2.9b}$$

where $V_{\text{cap}}(a, \psi) \equiv a^3 v(\psi)$ is the volume of a spherical cap of base radius a subtending an angle ψ (see Fig. 2.2 Inset) and

$$v(\psi) \equiv \frac{\pi}{3} \frac{2 - 3\cos\psi + \cos^3\psi}{\sin^3\psi}. \tag{2.10}$$

Now given the interfacial tensions, γ_{ij}, the substrate contact angle, θ_{12} and the drop volumes, V_2 and V_3, eqn (2.6) and (2.9) can be solved for a and α. The remaining geometric parameters of the compound sessile drop with a lens are then given by

$$R_{12} = a/\sin\omega, \quad R_{23} = a/\sin\alpha, \quad R_{13} = a/\sin\beta \tag{2.11a}$$

$$a_{12} = (\sin\theta_{12}/\sin\omega)\, a. \tag{2.11b}$$

2.3.2 Sessile drop with a collar

The three-phase contact region of a drop with a collar is illustrated in Fig. 2.3. The 12-interface and the 23-interface meet the substrate at prescribed contact angles θ_{12} and θ_{23} at $r = a_{12}$ and a_{23}, respectively. These together with the symmetry condition at $r = 0$ for the 13-interface gives three conditions

$$z'_{13}(0) = 0 \tag{2.12a}$$

$$z'_{12}(a_{12}) = \tan\theta_{12} \tag{2.12b}$$

$$z'_{23}(a_{23}) = \tan\theta_{23}. \tag{2.12c}$$

The force balance conditions at the three-phase contact line, eqn (2.6) and the pressure continuity condition, eqn (2.7) also hold for this case.

For the sessile drop with a collar, both phase 2 and phase 3 exert a downward pressure force on the substrate that can be written as

$$\begin{aligned} F_{\text{pressure}} &= \pi(a_{12}^2 - a_{23}^2)\,(\Delta P_{12}) + (\pi a_{23}^2)\,(\Delta P_{13}) \\ &= (\pi a_{12}^2)\,(\Delta P_{12}) + (\pi a_{23}^2)\,(\Delta P_{23}) \\ &= 2\pi \left(\gamma_{12} a_{12}^2 / R_{12} + \gamma_{23} a_{23}^2 / R_{23} \right). \end{aligned}$$

Around the contact lines at $r = a_{12}$ and a_{23} the interfacial tensions exert an upward

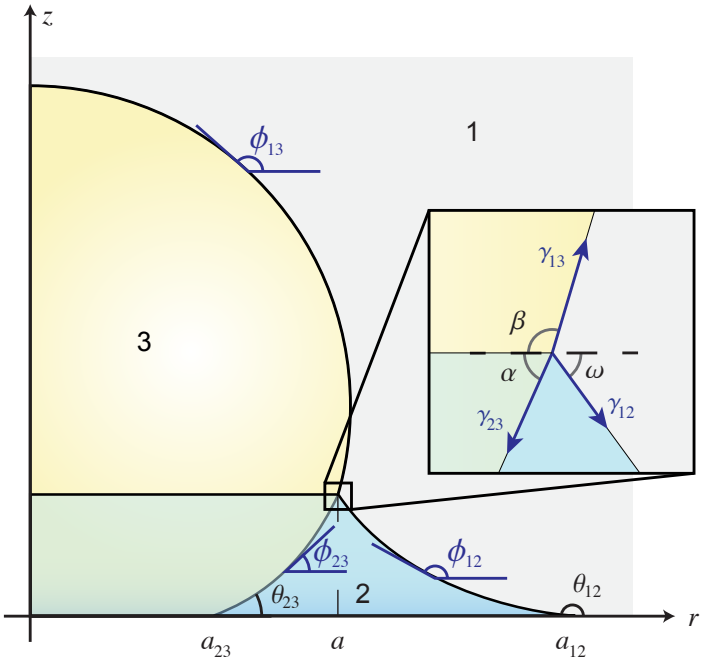

Figure 2.3: A schematic representation of the three-phase contact region of the collar around the base of a sessile drop comprising 3 mutually immiscible fluids with interfacial tensions γ_{12}, γ_{13} and γ_{23}.

force

$$F_{\text{interface}} = -(2\pi a_{23})(\gamma_{23}\sin\theta_{23}) - (2\pi a_{12})(\gamma_{12}\sin\theta_{12})$$

and these two contributions cancel to give

$$\begin{aligned} F &= F_{\text{pressure}} + F_{\text{interface}} \\ &= 2\pi\,\gamma_{12}\,a_{12}\left[\frac{a_{12}}{R_{12}} - \sin\theta_{12}\right] + 2\pi\,\gamma_{23}\,a_{23}\left[\frac{a_{23}}{R_{23}} - \sin\theta_{23}\right] = 0. \end{aligned} \tag{2.13}$$

For the sessile drop with a collar, the 13-interface is a spherical cap due to the boundary condition in eqn (2.12a), whereas the equations for the 12- and 23-interfaces can be expressed in terms of elliptic integrals. The method of solution is the same as that for the compound sessile drop with a lens given in Section 2.3.1.

2.4 Results and discussion

In this section, we demonstrate how the different configurations of compound sessile drops depicted in Fig. 2.1 can be realised by judicious choice of fluid combinations selected from Table 2.1. Where possible, the quantitative geometric features of the compound drops are checked against predictions of the Young–Laplace theory and known surface forces that prevail in each system.

Table 2.1: Specific gravity (SG), refractive index (RI) and interfacial tensions (γ_{ij}) of fluids used in making compound sessile drops. Interfacial tensions involving mercury are taken from the literature [24]. Other values are measured using the pendent drop method or deduced from the Young-Dupré equation.

SG	RI	γ_{ij} / (mN/m)					
			BD	M	PFO	TD	W
0.00	1.00	Air (A)	29.5	470	14	–	72
1.07	1.46	Bromodecane (BD)	–	–	–	–	44
13.5	–	Mercury (M)		–	–	–	428
1.77	1.28	Perfluorooctane (PFO)			–	5.4	52.2
0.76	1.43	Tetradecane (TD)				–	47.2
1.00	1.33	Water (W)					–

2.4.1 Sessile drop with total encapsulation

An example of a compound sessile drop, radius $\sim$ 150 µm, that contains a fully encapsulated inner phase (see Fig. 2.1a) is shown in Fig. 2.4. The perfluorooctane (PFO) sessile drop is immobilised on a hydrophobic glass substrate and immersed in water (W). The fully encapsulated phase is an air (A) bubble. From the values of interfacial tensions given in Table 2.1 we see that since $\gamma_{\mathrm{A/W}} > \gamma_{\mathrm{A/PFO}} + \gamma_{\mathrm{PFO/W}}$, a three phase contact line cannot be formed as it is not possible to satisfy the Neumann triangle condition. As a result, interfacial energies will be minimised when the air bubble is fully encapsulated in the perfluorooctane drop. This is an example of a liquid hydrophobic surface where the surface nanobubble cannot exist as interfacial energy considerations mean that such bubbles will always enter the perfluorooctane phase.

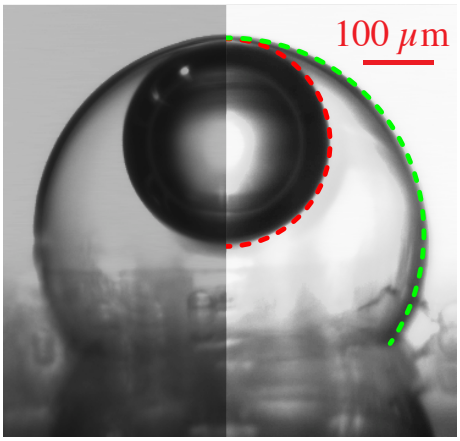

Figure 2.4: A compound perfluorooctane sessile drop on a hydrophobic glass substrate in water with a fully encapsulated air bubble. The contrast of the right side of the image has been reduced and the theoretical predictions of the two interfaces are overlaid for comparison.

Even though the drop sizes are such that all of the interfaces involved are well below their respective capillary lengths, the bubble is located at the apex of the sessile drop to minimise gravitational energy. Since the refractive index of perfluorooctane is intermediate between air and water (see Table 2.1), a repulsive van der Waals interaction will maintain a thin film of PFO between the air-water and air-PFO interfaces, and hence a disjoining pressure in the oil film balances the buoyancy force. This van der Waals repulsion inferred from refractive index differences has been verified with calculations based on the Lifshitz theory that includes electromagnetic retardation effects [21]. The presence of this film is evident as it is sufficiently thin to give rise to visible interference fringes when illuminated with monochromatic light. The repulsive van der Waals interaction across such films has also been measured directly using an atomic force microscope [25] so here we have an unusual example of a balance between fundamental forces on the nanoscale: van der Waals forces of quantum mechanical origin against gravity.

In the following section, we consider the situation in which the interfacial tensions are able to satisfy the Neumann condition to form a three phase contact line, which gives rise to sessile drops with a lens.

2.4.2 Sessile drop with a lens

In Fig. 2.5, we show two characteristic examples of compound sessile drops on a hydrophobic glass substrate under water in which the least dense phase is able to form a floating lens. In each case, this is because the values of the interfacial tensions can satisfy the Neumann condition to form a three phase contact line. In Fig. 2.5a, we show an air bubble that forms a lens at the apex of a bromodecane drop and in Fig. 2.5b, we have a tetradecane lens at the apex of a perfluorooctane drop. These two examples are distinguished by the sign of the curvature of the lens surface inside the sessile drop, giving a biconvex lens for the air-bromodecane case, and a convex-concave lens for the tetradecane-perfluorooctane case. The curvatures are controlled by the relationship between the relative phase volumes and the relative magnitudes of the interfacial tensions that determine the interfacial angles at the three phase contact line, when $r = a$ in Fig. 2.2.

Again the lens is located at the apex of the sessile drop to minimise the gravitational energy because in each case the density of the lens – air or tetradecane – is less than that of the sessile drop – bromodecane or perfluorooctane – and of the surrounding fluid (in each case water).

The refractive index of the lens (air or tetradecane) is intermediate between that of the sessile drop (bromodecane or perfluorooctane) and water (see Table 2.1), therefore the van der Waals interactions of the bromodecane-air-water and perfluoro-

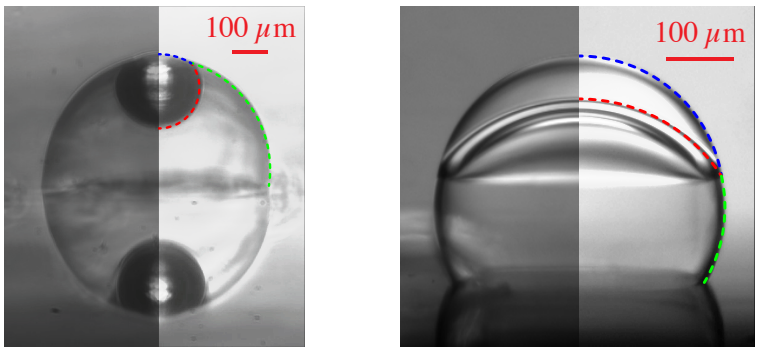

Figure 2.5: (a) An air bubble lens in a bromodecane drop on a hydrophobic glass substrate under water. The reflection of the bubble on the glass substrate is visible in the lower half of the photograph. (b) A tetradecane lens on a perfluorooctane drop on a hydrophobic glass substrate under water in which the lens interfaces have opposite curvatures. The contrast of the right side of the images has been reduced and the theoretical predictions of the interfaces are overlaid for comparison.

octane-tetradecane-water systems are both attractive. This again favours the formation of a three phase contact and the formation of a lens rather than the formation of fully encapsulated drops.

These observations provide simple design rules for creating compound sessile drops with a lens using readily-available material properties. The configurations of such compound drops are determined by four parameters: two ratios of the three interfacial energies, $(\gamma_{23}/\gamma_{12})$ and $(\gamma_{13}/\gamma_{12})$, the contact angle on the substrate, θ_{12}, and the volume ratio, (V_3/V_2). This paradigm, constructed from eqn (2.6), is illustrated in the interfacial energy ratio diagram shown in Fig. 2.6, in terms of the surface energy ratios: $(\gamma_{23}/\gamma_{12})$ and $(\gamma_{13}/\gamma_{12})$ for a base contact angle $\theta_{12} = 90°$ and a volume ratio $V_3/V_2 = 1/4$. Sessile drops with a lens can only form when the surface tension ratios are in the white 'Neumann' region of the diagram where the Neumann condition, eqn (2.1), can be satisfied. In the grey regions, surface energy minimisation means that phase 3 will exist as a separate phase, form a coating film on phase 2 or be encapsulated in phase 2 as indicated. Characteristic shapes of compound sessile drops with a lens are shown at key points in the energy ratio diagram indicated by the inset figures (i)–(viii). The locations of the experimental compound sessile drops demonstrating encapsulation (Fig. 2.4) and lens formation (Fig. 2.5a and b) are also indicated in this diagram. Each contour line in the Neumann region delineates the boundary where the lens is biconcave (to the right) or concave-convex (to the left). The location of this boundary varies with the phase volume ratio (V_3/V_2) as indicated.

When the relative densities and interfacial tensions of the fluids favour either the formation of a fully encapsulated drop or a lens on a sessile drop as depicted in

Fig. 2.1, the surface properties of the substrate only determine the contact angle, θ_{12} (see Fig. 2.2) of the encapsulating drop. However, if the fluid that forms the lens is denser than the surrounding fluid, more complex compound drop configurations can arise. We shall consider these in the following 2 sections.

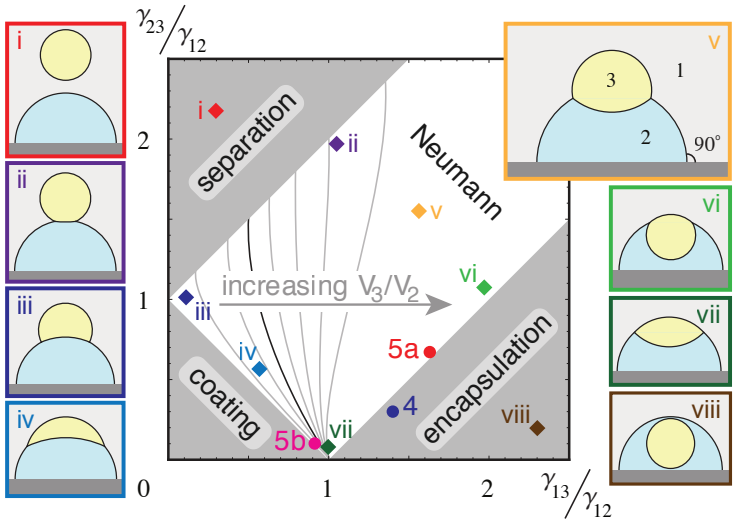

Figure 2.6: A representative interfacial energy ratio diagram based on eqn (2.6), that delineates the domain in which compound sessile drops with a lens can be formed in the Neumann region. The characteristic shapes of the lens in each location of the region are given in the insets (i)–(viii) for the substrate contact angle $\theta_{12} = 90°$ and volume ratio $V_3/V_2 = 1/4$. The locations of the experimental compound sessile drops given in Fig. 2.4, 2.5 are also indicated. The contour lines in the Neumann region locate the boundaries where the lens shape changes from concave-convex (to the left) to biconcave (to the right) at the volume ratios: $V_3/V_2 = 0.01, 0.1, 0.25, 0.5, 1, 2, 5$. (See text for details.)

2.4.3 Sessile drop with an evaporating collar

When the continuous phase is least dense, as in the case of compound sessile drops in air, both phases of the compound drop can be in contact with the substrate. One possibility for a compound sessile drop under such conditions is the axisymmetric configuration shown in Fig. 2.1c in which one phase forms a pendular ring or collar around the base of the sessile drop. The outer interface of the collar shares similarities with a liquid meniscus formed when a sphere is held above a surface [23]. A realisation of this configuration using a sessile mercury drop (radius $\sim$ 400 μm) in air on a hydrophilic glass substrate with a water collar around the base of the mercury drop is shown in Fig. 2.7. The water contact angle on this surface is $<$10 °. The time-lapse sequence of images shows the evaporation of the water collar. Videos of the evaporation of the water collar on a hydrophilic, hydrophobic and a semi-hydrophobic glass substrate are available online. See Appendix 2.B for details.

The evaporation in Fig. 2.7 took about 80 s to complete, and was a quasi-

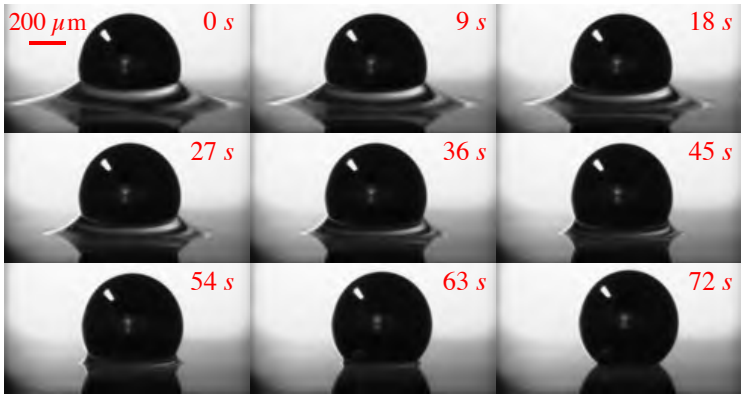

Figure 2.7: A mercury drop in air on a hydrophilic glass substrate (water contact angle <10 °) with a water collar around the base. Time-lapse images taken at 9 s apart show the progress of the evaporating water collar. A video is available via the Internet, see Appendix 2.B for details.

equilibrium process whereby the instantaneous drop and collar shapes can be described accurately by the Young–Laplace equation. In Fig. 2.8, we give a demonstration of the quasi-equilibrium nature of the evaporation of a water collar on a less hydrophilic substrate (water contact angle ~ 30 °) by comparing the collar shapes with the predictions of the Young–Laplace equation. Here the evaporation process is slightly slower because the higher water contact angle on the substrate exposes a smaller air–water interface at which evaporation takes place. In both cases, the water collar maintains axisymmetry as it evaporates; there is no apparent tendency for pinning of the air–water contact line on the substrate during evaporation.

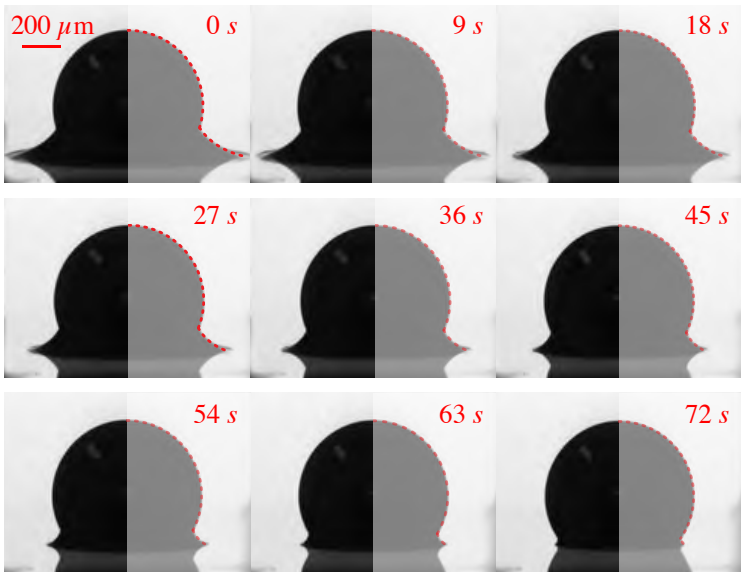

Figure 2.8: Time-lapse images of the evolving shape of a compound sessile drop on a hydrophilic glass substrate that is formed by a mercury drop in air with a water collar around the base (water contact angle ~ 30 °). As the water evaporates, successive images of the drop shapes are compared to the predictions of the Young–Laplace equation.

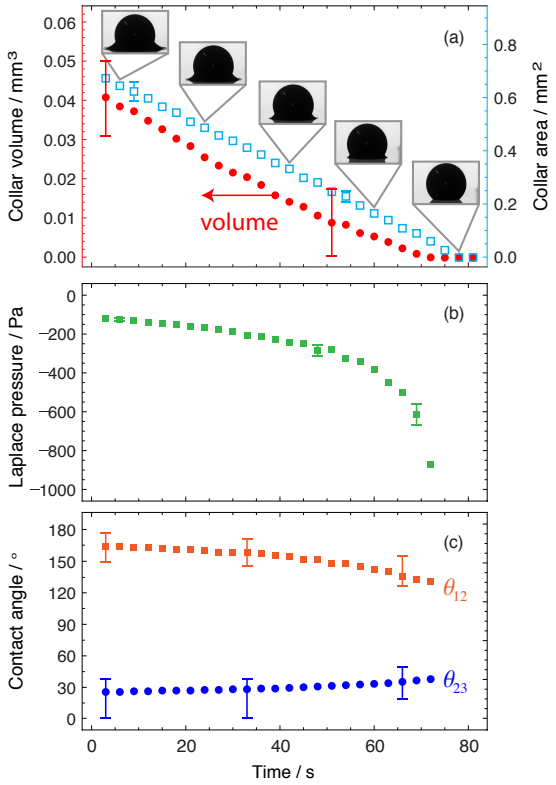

Figure 2.9: Time variations of (a) the collar volume (solid symbols, left hand axis) and collar surface area (open symbols, right hand axis), (b) the Laplace pressure of the evaporating water collar and (c) the contact angles of the mercury-water interface, θ_{23} and of the air-water interface, θ_{12} at the substrate extracted by fitting the collar shape to solutions of the Young–Laplace equation. Representative error bars are shown in each plot.

The dynamics of the evaporation process can be quantified by analysing the sequence of images. By assuming axial symmetry, the time variation of the collar volume, collar surface area, the Laplace pressure difference across the air-water interface and the contact angles at the substrate have been extracted using the Young–Laplace model and the results are shown in Fig 2.9. The rate of evaporation appears to be proportional to the exposed surface area of the evaporating collar, which suggests a dynamic process wherein the drop is not in equilibrium with a saturated vapour phase, but rather the atmosphere is depleted in water vapour. This is in line with the measured relative humidity within the laboratory (40%). Clearly the interfacial tension forces that act on the collar operate on a timescale that is much shorter than the diffusion driven evaporation process, and hence it is quite reasonable to use the Young–Laplace equation to analyse the drop geometry in each quasi-equilibrium image. It is also evident that the Laplace pressure difference across the air–water interface of the water collar is negative and therefore provides a capillary attraction that pulls the mercury drop towards the substrate. Indeed, towards the end of the evaporation process, small adjustments in the position of the mercury drop are observed as the water collar finally disappears. Videos of

evaporation experiments are available via the Internet, see Appendix 2.B for details.

The results shown in Fig 2.9 are likely to be more accurate in the initial 60 s. Thereafter, the volume of the water collar becomes small which increases the uncertainties in the values of the extracted parameters. The relative error in the extracted collar volume is large because the estimation involves the subtraction of quantities of similar magnitude. Within uncertainties in the analysis, the contact angles of the mercury-water interface θ_{23}, and of the air-water interface θ_{12}, at the substrate do not vary appreciably during the evaporation process.

In the following section, we will see that collar formation can arise from a complex competition of different interfacial energies and other forces.

2.4.4 Janus compound drops and collars

The characteristic length scales of all of the compound sessile drops considered so far are significantly below the capillary length. This means that the drop classifications are determined solely by interfacial energies. However, because of density differences between the fluid phases, the drops will adopt the configuration on the substrate that also minimises the gravitational energy. An illustration of this idea is given in Fig. 2.10a where a smaller but denser drop is placed on a large sessile drop. In the absence of gravity, the total surface energy of the system does not change as the location of the smaller drop is varied along the surface of the larger drop, provided it does not make contact with the substrate. However, gravity will cause the small drop to slide down and make contact with the substrate. This results in a Janus sessile drop (Fig 2.1d).

In Fig. 2.10b we show an example of a Janus drop in water that is comprised of a large mercury drop and a small perfluorooctane drop on hydrophilic glass substrate. As perfluorooctane is substantially more dense than the surrounding water, gravity dictates that the drop, although placed at the apex of the mercury drop, will slide down until it rests on the substrate. In contrast, for the air-bromodecane-water compound sessile drop shown in Fig. 2.5a, buoyancy kept the air bubble at the apex of the sessile bromodecane drop. However, if the density of the internal phase is greater than that of the sessile drop and surrounding fluid, it will slide down to the substrate, as for the mercury-perfluorooctane compound drop, resulting in an asymmetric state. An example of this is given in Fig. 2.10c in which the small perfluorooctane drop of the Janus pair is almost entirely engulfed within the larger tetradecane drop.

An interesting geometric transition occurs if one component of a Janus sessile drop can evaporate. In Fig. 2.11 we show a mercury-water Janus drop in air that was formed initially on a relatively hydrophobic substrate. The Janus configuration

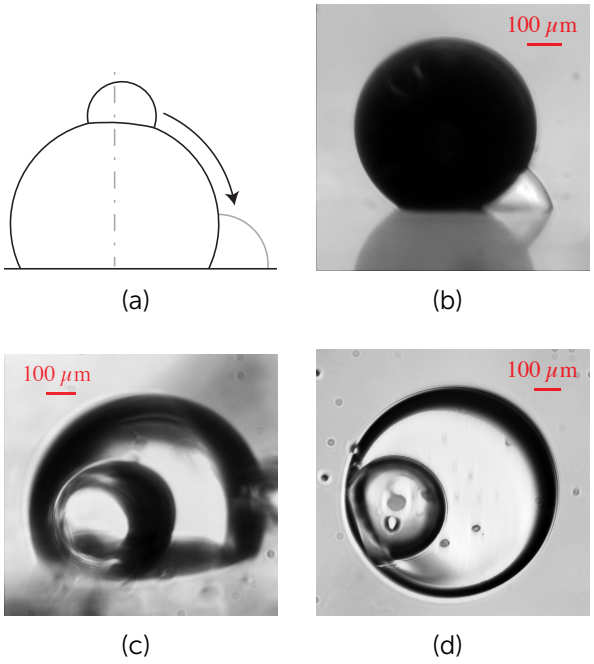

Figure 2.10: (a) A dense phase deposited on top of a sessile drop will slide down to contact the substrate to minimise gravitational energy. (b) A Janus sessile drop comprising a small perfluorooctane drop and a large mercury drop in air. (c) and (d) Two views of a Janus sessile drop in which a perfluorooctane drop appears to reside inside a larger tetradecane in water as viewed from the side (c) and from below (d).

is favoured as it minimises the water-hydrophobic glass contact area although a consideration of Kelvin capillary condensation would suggest that a small water collar around the mercury drop may exist for the initial Janus configuration, even though we cannot resolve it visually. However, as the water evaporates and the water drop volume decreases, the Janus drop undergoes a transition to a sessile mercury drop with a water collar that becomes clearly visible around its base. This occurs because, with a small volume of water, the increase in the energetically favourable water-mercury (hydrophilic) contact area can compensate the energy cost by increasing the water-glass (hydrophobic) contact area. A quantitative analysis of the energetics of such a transition from an asymmetric to an axisymmetric configuration is beyond the scope of the present work; we will address this problem in detail in the next chapter.

2.5 Conclusions

We have shown that three mutually immiscible fluids can form four different classes of compound sessile drops on a flat substrate. By using common material combinations, we demonstrate that these surface-immobilised compound drops can be realised experimentally in the range of drop-sizes where all interfaces are significantly

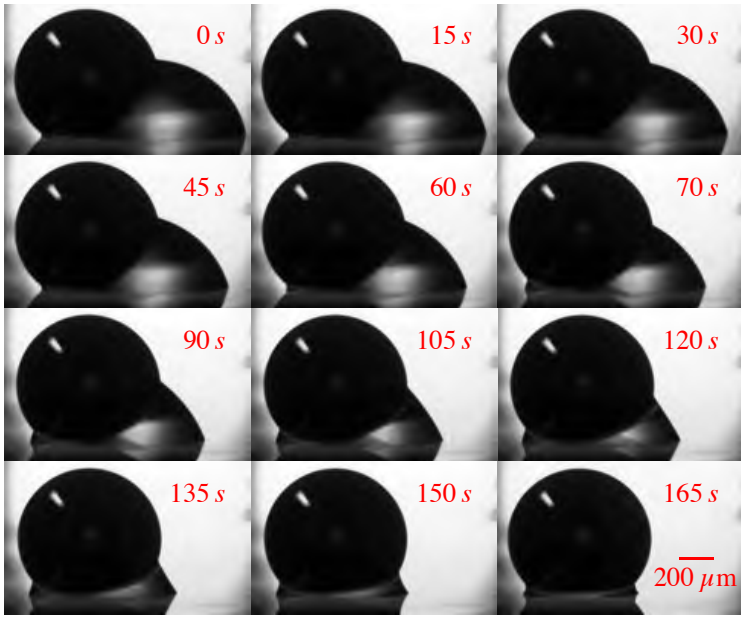

Figure 2.11: A mercury-water Janus sessile drop in air on a hydrophobic glass substrate. As the water evaporates, in changes to the collar configuration to maximise the energetically favourable water-mercury (hydrophilic) contact.

below the capillary length. As a result, the balance of surface energies dictates the shape of the compound drop adopted. Nonetheless, micro-gravity effects and van der Waals forces also play a role in determining the equilibrium configuration of phases.

Through direct image analysis of experimental drops, we show that the Young–Laplace equation provides an accurate description of the observed drop shapes. The characteristic shapes can be placed in a unified context using an interfacial energy diagram, Fig. 2.6. This is a useful design tool that can be used to visualise compound sessile drops with a lens with the desired geometric and optical properties.

By studying the evaporation of one component of a Janus sessile drop, an interesting transition was seen from the asymmetric Janus drop to an axisymmetric compound sessile drop with a collar. This transition appears to arise from the balance between the energy gained by increasing the energetically favourable drop-drop contact area against the unfavourable drop-substrate energy. The evaporation dynamics of a purely axisymmetric state were also studied, showing that evaporation was dependent only on the exposed surface area of the evaporating phase. This system may prove to be useful to examine effects such as evaporative self-assembly.

Thus, we have shown that although compound sessile micro-drops are comparatively easy to make, a wide range of geometries and behaviours exist. Through careful materials choice and suitable additives, such as styrene or siloxane monomers, drops could be made for applications in soft optics, surface photonics and targeted encapsulation and immobilisation on surfaces [26].

Acknowledgement

This project is funded in part by the Australian Research Council through a Discovery Project Grant. M.J.N. is supported by an Australian Postgraduate Research Award. The PFPC is thanked for infrastructure support.

2.6 Bibliography

[1] R. E. Johnson and S. S. Sadhal, *Ann. Rev. Fluid Mech.*, 1985, **17**, 289–320.

[2] P. G. de Gennes, F. Brochard-Wyatt and D. Quere, *Capillarity and Wetting Phenomena - Drops, Bubbles, Pearls, Waves*, Springer, New York, 2004.

[3] J. Guzowski, P. M. Korczyk, S. Jakiela and P. Garstecki, *Soft Matter*, 2012, **8**, 7269–7278.

[4] T. Nisisako and T. Torii, *Adv. Mater.*, 2007, **19**, 1489–1493.

[5] J. M. Andreas, *J. Chem. Ed.*, 1938, **15**, 523.

[6] A. R. Abate and D. A. Weitz, *Small*, 2009, **5**, 2030–2032.

[7] Z. Bei, T. B. Jones and D. R. Harding, *Soft Matter*, 2010, **6**, 2312–2320.

[8] M. Seo, C. Paquet, Z. Nie, S. Xu and E. Kumacheva, *Soft Matter*, 2007, **3**, 986–992.

[9] S. S. Sadhal and H. N. Oguz, *J. Fluid Mech.*, 1985, **160**, 511–529.

[10] D.-H. Lee, Y.-M. Goh, J.-S. Kim, H.-K. Kim, H.-H. Kang, K.-D. Suh and J.-W. Kim, *J. Disp. Sci. Technol.*, 2002, **23**, 491–497.

[11] R. Aveyard and J. H. Clint, *J. Chem. Soc., Faraday Trans.*, 1997, **93**, 1397–1403.

[12] J. C. Burton, F. M. Huisman, P. Alison, D. Rogerson and P. Taborek, *Langmuir*, 2010, **26**, 15316–15324.

[13] C. M. Phan, B. Allen, L. B. Peters, T. N. Le and M. O. Tade, *Langmuir*, 2012, **28**, 4609–4613.

[14] M. Aratono, T. Toyomasu, N. Ikeda and T. Takiue, *J. Colloid Interface Sci.*, 1999, **218**, 412–422.

[15] Y. Shao and T. G. M. van de Ven, *Langmuir*, 1989, **5**, 1234–1241.

[16] O. M. Lavrentevea, L. Rosenfeld and A. Nir, *Phys. Rev. E*, 2011, **84**, 056323.

[17] L. Rosenfeld, O. M. Lavrentevea and A. Nir, *J. Fluid Mech.*, 2009, **626**, 263–289.

[18] R. D. Deegan, O. Bakajin, T. F. Dupont, G. Huber, S. R. Nagel and T. A. Witten, *Nature*, 1997, **389**, 827–829.

[19] I. U. Vakarelski, D. Y. C. Chan, T. Nonoguchi, H. Shinto and K. Higashitani, *Phys. Rev. Lett.*, 2009, **102**, 058303.

[20] R. F. Tabor, F. Grieser, R. R. Dagastine and D. Y. C. Chan, *J. Colloid Interface Sci.*, 2012, **371**, 1–14.

[21] R. F. Tabor, C. Wu, H. Lockie, R. Manica, D. Y. C. Chan, F. Grieser and R. R. Dagastine, *Soft Matter*, 2011, **7**, 8977–8983.

[22] R. F. Tabor, A. J. Morfa, F. Grieser, D. Y. C. Chan and R. R. Dagastine, *Langmuir*, 2011, **27**, 6026–6030.

[23] F. M. Orr, L. E. Scriven and A. P. Rivas, *J. Fluid Mech.*, 1975, **67**, 723–742.

[24] M. C. Wilkinson, *Chem. Rev.*, 1972, **72**, 575–625.

[25] R. F. Tabor, R. Manica, D. Y. C. Chan, F. Grieser and R. R. Dagastine, *Phys. Rev. Lett.*, 2011, **106**, 064501/1–4.

[26] D. Graham-Rowe, *Nature Photon.*, 2006, 2–4.

2.A Mathematical details

The solutions of the Young–Laplace equation for the interfaces of axisymmetric compound sessile drops are outlined in this section.

2.A.1 Sessile drop with a lens

The first integral of the Young–Laplace equation (2.3), that describes an axisymmetric interface is

$$r \sin\phi = \frac{r^2}{R} + C. \tag{2.14}$$

For the 13- and 23-interface, the boundary conditions in eqn (2.4a) and (2.4b) set the constant of integration $C = 0$. Therefore the equation for these interfaces are (see Fig. 2.2)

$$r_{23}(\phi_{23}) = R_{23}\ \sin\phi_{23}, \quad r_{13}(\phi_{13}) = R_{13}\ \sin\phi_{13}. \tag{2.15}$$

These are equations for spherical caps of radii R_{23} and R_{13}.

For the 12-interface the condition that it meets the substrate at $r_{12} = a_{12}$ with contact angle $\phi_{12} = \theta_{12}$ means that the first integral has the form

$$r_{12} \sin\phi_{12} = \frac{r_{12}^2}{R_{12}} - \left[\frac{a_{12}^2}{R_{12}} - a_{12}\ \sin\theta_{12}\right]. \tag{2.16}$$

The force balance condition in eqn (2.8) of the main text implies that the term

$$G \equiv \left[\frac{a_{12}^2}{R_{12}} - a_{12}\ \sin\theta_{12}\right] = 0. \tag{2.17}$$

Therefore the 12-interface is also a spherical cap, of radius R_{12}

$$r_{12}(\phi_{12}) = R_{12}\ \sin\phi_{12}. \tag{2.18}$$

2.A.2 Sessile drop with a collar

The 12- and 23-interface meets the substrate at $r = a_{12}$ or a_{23} with contact angle $\phi = \theta_{12}$ or θ_{23} (see Fig. 2.3). The first integral of the Young–Laplace equation for each of these two interface can be written as

$$r \sin\phi = -\frac{r^2}{R} - \left[\frac{a^2}{R} - a \sin\theta\right] \equiv \frac{r^2}{R} - G \tag{2.19}$$

where we have suppressed the subscripts 12 and 23. This can be solved for $r(\phi)$

$$r(\phi) = \frac{R}{2}\left(\sin\phi \pm \sqrt{\sin^2\phi + \frac{4G}{R}}\right) \tag{2.20}$$

where the choice of sign is taken to ensure $r(\phi = \theta) = a$.

The height, z of the interface above the substrate can be found by integration

$$\begin{aligned} z(\phi) &= \int_\theta^\phi \frac{dz}{dr}\frac{dr}{d\varphi}d\varphi \\ &= \int_\theta^\phi \tan\varphi \left\{\frac{R}{2}\left(\cos\varphi \pm \frac{\sin\varphi\cos\varphi}{\sqrt{\sin^2\varphi + 4G/R}}\right)\right\} d\varphi \\ &= \frac{R}{2}\left[-\cos\varphi \pm \frac{1}{\sqrt{R/(4G)}}\left\{E\left(\varphi\middle| -\frac{R}{4G}\right)\right.\right. \\ &\qquad \left.\left. - F\left(\varphi\middle| -\frac{R}{4G}\right)\right\}\right]_{\varphi=\theta}^{\varphi=\phi} \end{aligned} \tag{2.21}$$

where $F(\varphi|m)$ and $E(\varphi|m)$ denote incomplete elliptic integrals of the first and second kind, defined by

$$F(\varphi|m) \equiv \int_0^\varphi \frac{1}{\sqrt{1 - m\ \sin^2\theta}}\, d\theta \tag{2.22}$$

$$E(\varphi|m) \equiv \int_0^\varphi \sqrt{1 - m\ \sin^2\theta}\, d\theta. \tag{2.23}$$

In general one must consider all possible choices of sign for R and G, however for the 12- and 23-interfaces considered here, R and G have the same sign and so we restrict ourselves to the case $G/R > 0$.

The above expressions for r and z give the position of the 12- and 23-interfaces as functions of the tangent angles ϕ_{12} and ϕ_{23} (see Fig. 2.3)

Although we have established the mathematical relationship between all variables, the method for determining the values of these parameters is very important. We therefore outline the algorithm used to find the given parameters.

To fit these solutions to experimental images of compound sessile drops with a collar, the software package *ImageJ* was used to first binarise the images, and then extract the profile as a list of coordinates. We then minimised the squared residuals as follows:

1. locate the 3-phase contact point, using a local minimum of the profile width, and split the image horizontally
2. use least squared fit to the top half to a sphere to obtain the radius R_{13}, and the horizontal position of the centre of the image

3. calculate the angle β from the height of the 3-phase contact, and the fitted radius, and then determined the radial position, a of the 3-phase contact line and the angle ω
4. pick a value for Laplace radius R_{12}
5. ensuring $r_{12}(\pi - \omega) = a$ sets the value of G_{12}
6. construct the 12-interface using $r_{12}(\phi)$ and $z_{12}(\phi)$, then compare this to experimental data using a 'distance-squared' objective function
7. adjust R_{12} and repeat process until a minimum is obtained
8. vary β within experimental error and repeat steps 5-8.

2.B Supplementary videos

We include three movies of the evaporation of a water collar around a mercury drop:

1. Movie 1 - on a hydrophilic glass substrate
2. Movie 2 - on a semi-hydrophobic glass substrate
3. Movie 3 - on a hydrophobic glass substrate.

These videos are available via the Internet at http://doi.org/10.1039/c2sm26637g.

CHAPTER 3

Particle–drop–substrate systems

The liquid bridge that forms between a particle and a flat surface, and the dynamics of its evaporation are pertinent to a range of physical processes including paint and ink deposition, spray drying, evaporative lithography and the flow and processing of powders. Here, using time-lapse photography, we investigate the evaporative dynamics of a sessile liquid bridge between a particle and a planar substrate. Different wetting characteristics of the particle and substrate are explored, as well as the effects of contact line pinning and stick-slip boundary conditions. A theoretical framework is developed to quantify and analyse the experimental observations. For the size range of particles and drops used in this study, gravity is by far the smallest force in the system when compared to the surface tension and capillary interactions that are present, but in certain circumstances it dictates the key evolution stages of the geometry of the particle-drop-substrate systems. Analysis of evaporation dynamics and capillary forces indicate that at low Bond numbers, surface tension forces dominate and provide unique opportunities for the control of particles on surfaces.

This chapter has been published as Michael J. Neeson, Raymond R. Dagastine, Derek Y. C. Chan and Rico F. Tabor, *Evaporation of a capillary bridge between a particle and a surface*, Soft Matter, 2014, **10**, 8489–8499 — Reproduced by permission of The Royal Society of Chemistry.

The existence of liquid bridges between solids – either as particles or extended flat surfaces – is of considerable interest and importance in a range of fields, which can be crudely separated into three classes based on their geometry: (i) one or more small particles can sit at the interface of a much larger drop, (ii) a small liquid volume sits between two solid surfaces forming a 'capillary bridge' and (iii) the transitional case where the sizes of the drop and particle are of comparable magnitude.

The limit in which the particle radius is much smaller than the drop radius has been investigated extensively, primarily in the context of Ramsden or Pickering emulsions [1, 2], foams, 'dry water' [3] and liquid marbles [4, 5, 6], where many particles are adsorbed at a liquid interface to confer stability [7, 8]. The force between a small particle and a drop (or bubble) interface has been investigated by various groups using the atomic force microscope, and the observed behaviour analysed in terms of wetting and capillarity [9, 10, 11, 12, 13]. Using a perturbation analysis, the lateral capillary interactions between particles in a Pickering emulsion were theoretically investigated [14].

For the case of multiple particles joined by liquid capillary bridges, each bridge can be defined geometrically by its volume and the contact angle at the particle surfaces. This case is of interest when powders are processed and handled, particularly in moist environments or where hygroscopic materials are involved [15, 16]. Common examples include minerals and ceramics processing, foods (*e.g.* starch and whey powders) and permeation and moisture retention in soils and sediments [17, 18]. Recently it was shown that the addition of a tiny amount of a secondary fluid to a suspension causes large capillary networks, greatly altering its bulk rheological behaviour [19].

Capillary bridges are of particular importance since they give rise to the capillary force, which has wide-ranging implications in the study of interfacial forces in atomic force microscopy [20] and particle adhesion [21, 22, 23] through to nanoscale applications such as dip-pen lithography [24] and micro-manipulation [25]. Several studies have experimentally investigated the forces arising from small capillary bridges between a particle and a surface [26].

Orr *et al.* [27] provided a comprehensive theoretical treatment of an axisymmetric capillary bridge between a spherical particle and a flat substrate. More recently Guzowski *et al.* [28] considered the capillary force that acts on a particle attached to an initially spherical interface when subjected to an asymmetric displacement of the particle.

When multiple particles sit on a flat liquid surface, the local interface near each particle is deformed, resulting in a lateral capillary force between particles that can be either attractive or repulsive. The attractive lateral capillary force facilitates the self-assembly of large two-dimensional crystal arrays [29, 30, 31]. Alternatively, col-

loidal self-assembled arrays can be formed by initially suspending multiple particles inside a drop and subsequently evaporating the supporting drop [32, 33, 34, 35, 36]. Since these capillary forces are extremely large when compared to, for example, particle weights, they provide surprising and useful behaviours such as adhesives that mimic gecko adhesion [37] and insects that are able to climb 'uphill' at liquid menisci [38].

Although the behaviour of both a small particle on a much larger spherical drop, class (i), and a small liquid bridge between a large particle and a surface, class (ii), have both been studied extensively, the same cannot be said for the intermediate class (iii), where the characteristic dimensions of both the particle and the drop are comparable. Such configurations share similarities with those for which the particle is replaced by a third mutually immiscible fluid [39].

In this chapter we consider, both theoretically and experimentally, the capillary bridge formed between a spherical particle and a planar substrate. We analyse the cases of pinned contact line as well as constant contact angle boundary conditions at both fluid-fluid-surface contacts, as it is seen that both boundary conditions are observed in the presented experiments.

By comparing the Gibbs free energy for each configuration, we are able to determine the energetically favoured configuration, revealing an important critical volume below which an axisymmetric collar is formed around the base of the particle, exerting an attractive force between the particle and the substrate, whereas above this critical volume the interface is spherical with no capillary force acting between the particle and the substrate.

Having developed a theoretical solution for an equilibrium capillary drop interface, we present a series of experiments with a small particle at the air-water interface of a water sessile or pendant drop. By allowing the drop to evaporate and tracking the evolution of the drop shape by time-lapse photography, we are able to investigate the dependence of system geometry on volume as well as hysteresis effects, using the theoretical model to obtain relevant physical parameters for comparison.

3.1 Theory

When a spherical particle of radius a is placed at the interface of a sessile drop of fluid 2, surrounded by an outer fluid 1, a liquid capillary bridge is formed between the particle, p and the substrate, s (Fig. 3.1). The characteristic dimension of the drop over which gravitational forces can deform the interface is the capillary length $\lambda = \sqrt{\gamma_{12}/\Delta\rho g}$, where γ_{12} is the interfacial tension of the 12-fluid interface, $\Delta\rho$ is the density difference between the two fluid phases and g is the gravitational

acceleration. For drop dimensions well below the capillary length ($\sim$ 2.7 mm for a water drop in air) its shape will be determined by the Young–Laplace equation without the gravitational term,

$$\gamma_{12}\left(\frac{1}{R_1}+\frac{1}{R_2}\right)=\Delta P\equiv P_{\text{in}}-P_{\text{out}} \tag{3.1}$$

that relates the pressure difference, ΔP, across the interface and the principal radii of curvature R_1 and R_2 of the drop. By expressing R_1 and R_2 in terms of the co-ordinates of the interface we obtain a differential equation for the drop shape.

The solution for the drop shape is determined by the drop volume and by the physical condition at the three-phase contact lines at the substrate and at the particle. In the present context of how the shape of the liquid bridge evolves as the drop evaporates, we consider two possibilities: (I) the contact angle at the three-phase contact line remains constant as evaporation progresses and is given by θ_{p} at the particle and by θ_{s} the substrate, according to the Young-Dupré equation, or (II) the position of the contact line is fixed during evaporation. In the latter case, the position of the pinned contact line is prescribed by the angle, α, subtended at the centre of the particle and by the radial position, r_{s}, of the contact line measured along the substrate (see Fig. 3.1).

We can now consider the two possible drop or liquid bridge shapes that can form depending on the location of the particle relative to the sessile drop and the substrate. The characteristic dimension of the drop or liquid bridge is assumed to be small compared to the capillary length so that gravity does not affect the drop shape through the Young-Laplace equation. However, as we shall see, the small gravitational force plays an important role in determining the position of the particle in relation to the substrate through density difference between the particle and the fluid phases.

3.1.1 Spherical drop interface

If the spherical particle does not make contact with the substrate and is located in a symmetrical position about the apex of the sessile drop (Fig. 3.1), the drop interface will be a portion of a sphere with radius $R_1 = R_2 \equiv R = 2\gamma_{12}/\Delta P$, the Laplace radius, see eqn (3.1). The particle can be maintained in this symmetrical position by a gravitational force that is negligible in deforming the interface. We now show that this solution can also satisfy the required boundary conditions at the particle and the substrate.

The spherical liquid interface makes contact with the substrate at the contact radius r_{s} where the contact angle is θ_{s} and also from the cosine rule for the triangle

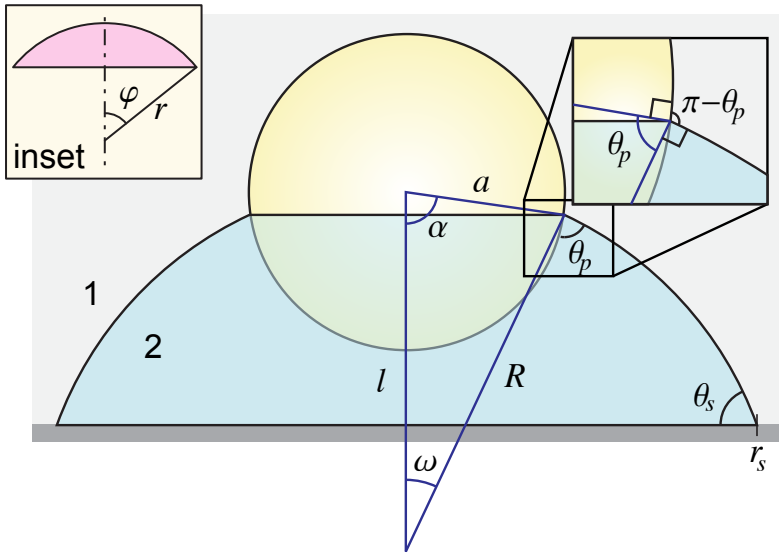

Figure 3.1: A spherical air-water interface, with the particle sitting axisymmetrically at the apex of the drop. Inset: a spherical cap of volume and surface area of v_{cap} and s_{cap}, respectively, with a interface radius r subtending an angle φ.

formed between the centre of the particle, centre of the spherical interface and the three phase contact line at the particle we can obtain the following equations, see Fig. 3.1,

$$r_{\text{s}} = R\sin\theta_{\text{s}} \tag{3.2a}$$

$$l^2 = a^2 + R^2 - 2aR\cos\theta_{\text{p}} \tag{3.2b}$$

$$R^2 = a^2 + l^2 - 2al\cos\alpha \tag{3.2c}$$

where l is the distance between the centre of the particle and the centre of the spherical interface. If the constant contact angle condition holds at the three phase line at the substrate and at the particle, θ_{s} and θ_{p} will be prescribed. Thus eqn (3.2) can be used to determine unknowns $(\alpha, r_{\text{s}}, l, R)$ when the drop volume is specified. On the other hand, if the positions of the contact lines are pinned, then α and r_{s} will be prescribed and eqn (3.2) can be used to determine unknowns $(\theta_{\text{s}}, \theta_{\text{p}}, l, R)$ when the drop volume is specified.

A useful relation between the angles θ_{p} and α can be found by equating the radius of the meniscus contact with the sphere, giving $R\sin[\pi - (\alpha + \theta_{\text{p}})] = a\sin\alpha$. Using eqn (3.2a) allows R to be eliminated, giving

$$r_{\text{s}}\sin[\pi - (\alpha + \theta_{\text{p}})] = a\sin\alpha\sin\theta_{\text{s}}. \tag{3.3}$$

There exists a critical minimum drop or liquid bridge volume at which the particle can remain at the apex of a spherical drop, while it is also in contact with the

substrate. If the drop volume is above this critical volume, the drop interface will be a segment of a sphere and the particle can be located at any point on the interface without affecting the interfacial energy of the system. Thus, the gravitational energy will determine the position of the particle, with the particle either touching the substrate or be located at the apex, depending on the densities of both phases and the particle.* An expression to determine the position of the particle is given in Appendix 3.A. The volume of the drop and the surface areas of the 12-, 2s- and 2p-interfaces can then be written in terms of those of a spherical cap

$$V^{\mathrm{s}} = v_{\mathrm{cap}}(R, \theta_{\mathrm{s}}) - v_{\mathrm{cap}}(R, \omega) - v_{\mathrm{cap}}(a, \alpha) \tag{3.4a}$$

$$A^{\mathrm{s}}_{12} = s_{\mathrm{cap}}(R, \theta_{\mathrm{s}}) - s_{\mathrm{cap}}(R, \omega) \tag{3.4b}$$

$$A^{\mathrm{s}}_{2\mathrm{s}} = \pi \left(R \sin \theta_{\mathrm{s}}\right)^2 \tag{3.4c}$$

$$A^{\mathrm{s}}_{2\mathrm{p}} = s_{\mathrm{cap}}(a, \alpha) \tag{3.4d}$$

where we have introduced $\omega \equiv \pi - (\theta_{\mathrm{p}} + \alpha)$, together with the volume and surface area of a spherical cap, as defined in Fig. 3.1 (inset),

$$v_{\mathrm{cap}}(r, \varphi) \equiv \frac{\pi r^3}{3} \left(2 - 3\cos\varphi + \cos^3\varphi\right) \tag{3.5}$$

$$s_{\mathrm{cap}}(r, \varphi) \equiv 2\pi r^2 \left(1 - \cos\varphi\right). \tag{3.6}$$

If the particle is located at the apex of the drop, the distance of closest approach, h_0, between the particle and the substrate is

$$h_0 = l - (a + R\cos\theta_{\mathrm{s}}). \tag{3.7}$$

As the volume of the supporting drop decreases, the particle will eventually come into contact with the substrate. This volume is the minimal drop volume for which a spherical configuration can exist. Below this, the drop shape will be an axisymmetric collar that we consider next.

3.1.2 Axisymmetric collar

The shape of an axisymmetric capillary bridge between a particle and substrate has been considered by Orr *et al.* [27]. By writing the r and z variables with respect to the angle ϕ between the meniscus and the horizontal, they presented the solution in terms of elliptic integrals. The form of their solution required a choice of sign that is related to the meridional curvature (defined below). For an interface where the

*The particle will not sit at an intermediate point for the same reason a particle submersed in a volume of water will either rise or sink.

meridional curvature changes sign, careful use of limits is required. Here we find it more convenient to parameterise the drop shape with respect to the arc length s, although the result is mathematically identical to the solution of Orr *et al.* [27].

In Fig. 3.2 we show a spherical particle in contact with a substrate with a liquid bridge in the form of an axisymmetric collar around its base. The angle α locates the position of the three phase contact line on the particle surface. In this case, it is convenient to work with the mean curvature $H \equiv \Delta P/2\gamma_{12}$ of the interface that is initially positive and decreases continuously as the drop volume decreases, passing through zero before becoming negative.

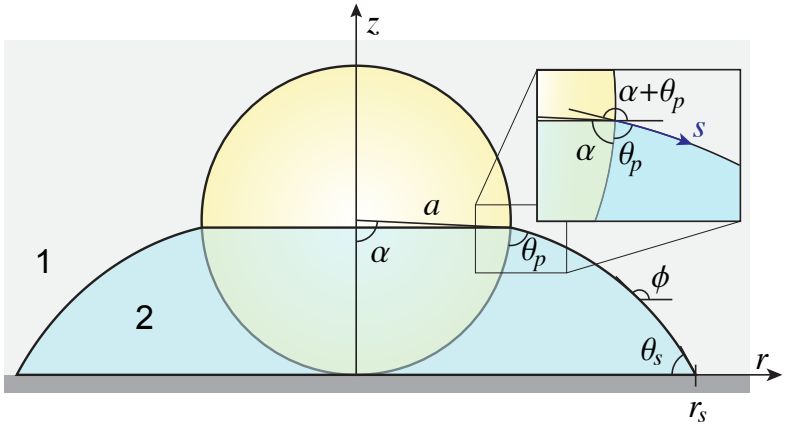

Figure 3.2: A schematic representation of the three-phase contact region of an axisymmetric collar formed around particle-substrate contact.

The meridional curvature, $1/R_1 = -\mathrm{d}\phi/\mathrm{d}s$ and the azimuthal curvature, $1/R_2 = \sin\phi/r$ can be expressed in terms of the tangent angle ϕ, and trigonometry gives $\mathrm{d}r/\mathrm{d}s = -\cos\phi$ and $\mathrm{d}z/\mathrm{d}s = -\sin\phi$. The origin of the arc length $s = 0$ is at the particle, with s increasing away from the particle. Using eqn (3.1) we obtain a system of 3 ordinary differential equations

$$\frac{\mathrm{d}\phi}{\mathrm{d}s} = -\left(2H - \frac{\sin\phi(s)}{r(s)}\right) \tag{3.8a}$$

$$\frac{\mathrm{d}z}{\mathrm{d}s} = -\sin\phi(s) \tag{3.8b}$$

$$\frac{\mathrm{d}r}{\mathrm{d}s} = -\cos\phi(s) \tag{3.8c}$$

to be solved with the following boundary conditions at the particle, p and at the substrate, s

$$\mathrm{p}: \quad \phi = \alpha + \theta_\mathrm{p}, \quad r = a\sin\alpha, \quad z = a(1-\cos\alpha), \quad s = 0 \tag{3.9a}$$

$$\mathrm{s}: \quad \phi = \pi - \theta_\mathrm{s}, \quad r = r_\mathrm{s}, \quad z = 0, \quad s = s_\mathrm{max}. \tag{3.9b}$$

The volume V^{c} of the collar, and the surface areas of the 12-, 2s- and 2p-interface (A^{c}_{12}, $A^{\mathrm{c}}_{2\mathrm{s}}$, $A^{\mathrm{c}}_{2\mathrm{p}}$ respectively) can be calculated from

$$V^{\mathrm{c}} = \pi \int_0^{s_{\max}} r^2 \frac{\mathrm{d}z}{\mathrm{d}s}\,\mathrm{d}s - v_{\mathrm{cap}}(a,\alpha) \tag{3.10a}$$

$$A^{\mathrm{c}}_{12} = 2\pi \int_0^{s_{\max}} r\,\mathrm{d}s \tag{3.10b}$$

$$A^{\mathrm{c}}_{2\mathrm{s}} = \pi \left(a\sin\alpha + \int_0^{s_{\max}} \frac{\mathrm{d}r}{\mathrm{d}s}\,\mathrm{d}s \right)^2 \tag{3.10c}$$

$$A^{\mathrm{c}}_{2\mathrm{p}} = s_{\mathrm{cap}}(a,\alpha). \tag{3.10d}$$

An iterative method is required to solve the coupled differential equations in order to determine the unknown H that is consistent with the prescribed volume and either the prescribed contact positions or contact angles at the two three phase contacts.

We outline an iterative method for generating interfaces for the case where both contact angles are constant. To begin, we pick a value for α and choose an initial value for the mean curvature H_0. An interface can now be generated by solving eqn (3.8), subject to the initial conditions (3.9a). The differential equations are solved numerically until $z = 0$, with the arc length at this point being denoted $s_{\max}$. We now form an objective function based on the boundary condition, in this case $g(H) = \phi(s_{\max}) - (\pi - \theta_{\mathrm{s}})$, which we require to be zero. The quantity H_i can now be updated using the secant method. This process is repeated until the boundary condition at the substrate is satisfied to within a specified tolerance. Changing the filling angle α results in interfaces corresponding to different drop volumes.

3.1.3 Evaporation dynamics

The evaporation rate for a sessile drop undergoing diffusion-driven evaporation was first solved by Picknett and Bexon [40]. By drawing an analogy between the equations governing diffusion-driven evaporation and electrostatic potential, they developed a differential equation for the evaporation rate which involved a contact angle dependant parameter $h(\theta) \equiv C(\theta)/R$, with $C(\theta)$ being the capacitance of a lens of the same shape that can be expressed analytically as an infinite series. For numerical work, Picknett and Bexon [40] presented an approximate polynomial expression for the capacitance of the scaled lens in terms of the angle θ,

$$h(\theta) = \begin{cases} 0.6366\theta + 0.09591\theta^2 - 0.06144\theta^3, & 0 \le \theta \le 0.175 \\ 0.00008957 + 0.6333\theta + 0.1160\theta^2 & \\ \qquad -0.08878\theta^3 + 0.01033\theta^4, & 0.175 \le \theta \le \pi \end{cases} \tag{3.11}$$

that is accurate to within 0.2% of the analytical result. The evaporation rate can then be expressed as

$$\rho \frac{dV}{dt} = -\frac{2\pi r_s D(c_s - c_\infty)}{\sin\theta_s} h(\theta_s) \tag{3.12}$$

where D is the molecular mass diffusion constant, while c_s and c_∞ are the vapour concentrations at the interface and in the far field, respectively. The volume of a sessile drop can be written as

$$V = \frac{\pi r_s^3}{3} \frac{2 - 3\cos\theta_s + \cos^3\theta_s}{\sin^3\theta_s} \equiv \frac{\pi}{3} r_s^3 \, \nu(\theta_s) \tag{3.13}$$

where we have used eqn (3.2a). This expression depends only on the contact radius and the contact angle, one of which is constant depending on the substrate contact condition.

Pinned contact line: For the pinned contact line case, r_s is specified so the drop volume depends only on the contact angle θ_s, and thus combining eqn (3.12) and (3.13) gives the differential equation

$$\frac{d\theta_s}{dt} = -\frac{2D(c_s - c_\infty)}{\rho r_s^2} \frac{(1 + \cos\theta_s)^2}{\sin\theta_s} h(\theta_s). \tag{3.14}$$

Taking the time scale $t_s = \rho r_s^2 / 2D(c_s - c_\infty)$, and t_f as the time when the drop vanishes, the solution of eqn (3.14) can be written as

$$\bar{t}_f - \bar{t} = \int_0^{\theta_s} \frac{\sin\theta'}{(1 + \cos\theta')^2 h(\theta')} \, d\theta' \equiv G(\theta_s) \tag{3.15}$$

where $\bar{t} = t/t_s$ is the scaled time. For more details see Dash and Garimella [41] and Gelderblom *et al.* [42].

Constant contact angle: For the constant contact angle case, θ_s is specified so the solution of eqn (3.12) and (3.13) is

$$r_s^2 = \frac{4D(c_s - c_\infty)}{\rho} \frac{h(\theta_s)}{\nu(\theta_s)\sin\theta_s} (t_f - t) \tag{3.16}$$

which differs from the evaporation rate presented by McHale *et al.* [43] (see their eqn (6)), that neglected the local geometrical behaviour near the three-phase contact line. Taking the length scale as the initial contact radius $L_c \equiv r_s(t = 0)$, together with the time scale

$$t_s = \frac{\rho L_c^2}{4D(c_s - c_\infty)} \frac{\nu(\theta_s)\sin\theta_s}{h(\theta_s)} \tag{3.17}$$

the solution of eqn (3.16) for the constant contact angle case can be written in the simple nondimensional form

$$\bar{r}_s = \sqrt{1 - \bar{t}}. \tag{3.18}$$

Thus the result in eqn (3.15) gives the variation of the contact angle at the substrate with time as the drop evaporates under the pinned contact line condition, whereas the result in eqn (3.18) gives the variation of the position of the contact line at the substrate with time as the drop evaporates under the constant contact angle condition.

3.2 Materials and methods

Water was obtained from a Millipore Direct-Q 5 system (minimum resistivity 18.4 MΩ cm). Polystyrene spheres (Amberlite XAD-4, Sigma) with a radius of ∼150 μm were used as received. Glass microparticles with radii 100–400 μm were obtained from Polysciences, Inc (#18903) and used as received. Poly(methyl methacrylate) (PMMA, 99%, Sigma) was spin-coated onto glass microscope slides at 3000 rpm from a 20 mg·mL^{-1} solution in chloroform. Gold surfaces were generated by sputtering 5 nm of chromium (as an adhesion layer) and 50 nm of gold using a Quorum Q150T-S sputter coater. A polystyrene tissue culture dish was used as the polystyrene substrate and a poly(tetrafluoroethylene) (PTFE) surface was made by stretching a length of PTFE tape over a glass microscope slide.

For each experiment a water pendant or sessile drop was formed on the required substrate. The small gravitational force was used to ensure the initial position of the particle is at the apex of the pendent or sessile drop on the substrate. The evaporation rate depends on the combination of the parameters $D(c_s - c_\infty)$ that varies with temperature and relative humidity (see eqn (3.15) and (3.18)). However, no special steps were taken to control these values in the laboratory.

Experiments were visualised using a CCD camera (Flea3, Point Grey, Richmond, BC, Canada) coupled to a Kozo XJP-300 microscope. The optical system was calibrated with a known size standard, measured using laser diffraction. Diffuse illumination was provided using a white LED source and a diffuser. Each experimental image was first binarised to extract the drop-particle profile, and then a routine developed in Mathematica (Wolfram Research) was used to fit the theoretical solution. A Levenberg–Marquardt optimisation routine was used to ensure rapid convergence of the experimental and theoretical drop profiles. Physical quantities were then extracted from the optimised parameters.

3.3 Results and discussion

Here we present and discuss the geometric and evaporative characteristics of four key systems that serve to illustrate the complex range of behaviours available to particle-drop-substrate systems. Material combinations were chosen to provide a range of different surface wettabilities, in order to explore conditions in which the droplet contact angle and solid-water-air van der Waals force (relevant to the wetting behaviour) vary widely:

1. Silica-water-poly(tetrafluoroethylene), PTFE: the water droplet adopts a spherical solution throughout, and the silica particle does not come into contact with the substrate until the end of the evaporation process.

2. Silica-water-gold: the water droplet transitions from a spherical to axisymmetric collar configuration.

3. Polystyrene-water-polystyrene: the water droplet adopts a collar configuration throughout, including geometries where the meridional curvature of the interface changes sign resulting in an inflection in the function $z(r)$.

4. Silica-water-poly(methyl methacrylate), PMMA: the water droplet transitions from an asymmetric spherical solution to an axisymmetric collar configuration.

In each experiment, a water drop was deposited onto the substrate, forming either a pendant (experiments 1–2) or a sessile (experiments 3–4) drop depending on the orientation of the substrate. A particle was then placed onto the immobilised drop, resulting in either a collar or a spherical configuration. Fig. 3.3 shows time-lapse photographs of the evaporation process for experiments 1–3. Videos of evaporation experiments are available in the Appendix 3.B. As discussed later, the evaporation time-scale is sufficiently slow that each instantaneous configuration can be accurately described by the equilibrium Young–Laplace equation.

Time-lapse images were compared to interfacial profiles predicted by the Young–Laplace equation. The accuracy of the fit was demonstrated by overlaying predicted interfaces on top of time-lapse photographs, as shown in Fig. 3.4.

The extracted data allows the contact radii and contact angles to be calculated at both the particle and the substrate, together with the drop volume, air-water interfacial area and Laplace pressure. Using these quantities, it is then possible to calculate the capillary force $F_{\text{capillary}}$ between the particle and the substrate

$$\begin{aligned} F_{\text{capillary}} &= F_{\text{interfacial tension}} - F_{\text{pressure}} \\ &= (2\pi r_{\text{s}})(\gamma_{12}\sin\theta_{\text{s}}) - (\Delta P)(\pi r_{\text{s}}^2), \end{aligned} \tag{3.19}$$

Figure 3.3: Time-lapse images of the evolution of three different axisymmetric particle-drop-substrate systems. (a) A water pendant drop hanging from a hydrophobic PTFE substrate with a silica particle resting at the apex of the drop, with the particle touching the substrate in the final frame. (b) A water pendant drop hanging below a gold substrate, with a silica particle initially at the apex of the drop. The particle touches the substrate after 285 seconds, after which an axisymmetric collar rests around the particle-substrate contact. (c) A polystyrene particle in contact with a polystyrene substrate with an axisymmetric collar formed around the contact for the duration of the experiment. The blue shaded regions denote the experimental images for which the particle is in contact with the substrate. See Appendix 3.B for videos of each experiment.

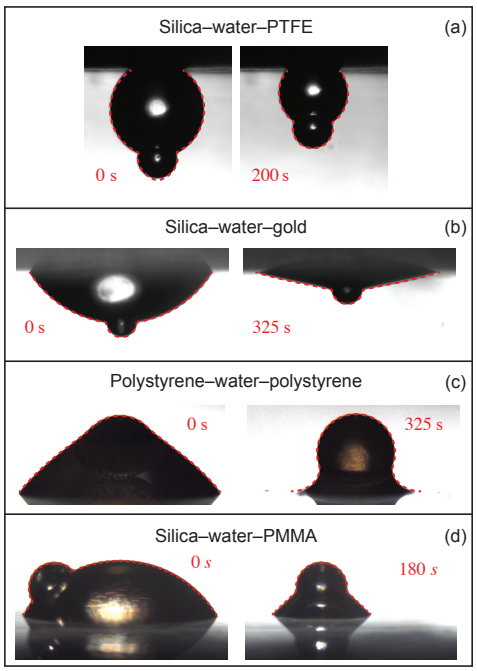

Figure 3.4: Two representative experimental drop profiles for each of the four experiments are compared to the Young–Laplace solution.

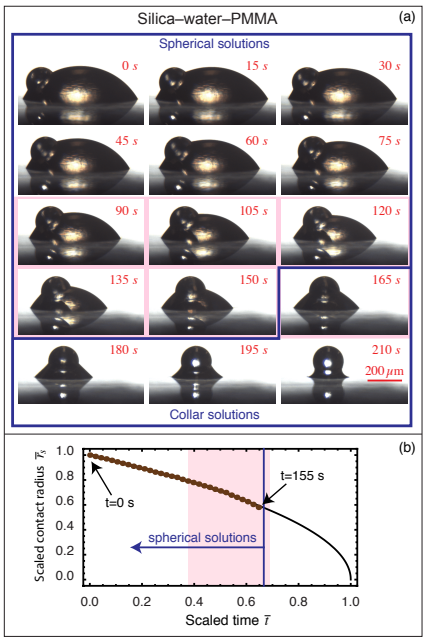

Figure 3.5: (a) A silica particle on a PMMA coated substrate with a water drop around the base. Time-lapse images taken 15 s apart show the progress of the evaporation. The system is initially asymmetric due to the density of silica being greater than water. As the volume of the drop decreases, the system evolves towards an axisymmetric collar, which is achieved at approximately 160 s into the experiment. Thereafter, the system remains in the axisymmetric collar configuration until the water completely evaporates. The shaded red region denotes the region where the experimental interfaces deviate from the theoretically predicted interfaces due to surface non-ideality, while the blue line delimits the region where the interfaces are spherical from those which are axisymmetric collar. (b) The scaled substrate contact radius evolution versus scaled time (brown symbols) for which the interfaces are spherical interfaces. The black line represents the theoretical evolution of the contact radius for diffusion-driven evaporation neglecting the presence of the particle. See Appendix 3.B for a video.

chosen to be positive when the force is attractive. The extracted quantities are plotted against time in Fig. 3.6 and 3.7, and discussed in detail in the sections below.

3.3.1 Initial configuration

When a particle is placed at the interface of a sessile drop, the analysis presented in Section 3.1 predicts that one of two basic configurations will be assumed. If the sessile drop volume is less than the critical volume for spherical drop formation, then an axisymmetric collar around the particle-substrate contact will form, whereas if the volume is above the critical volume the air-water interface will be spherical. This spherical case can be split into energetically equivalent but geometrically resolved homologues, as the particle can sit at any point on the interface without energetic penalty. Therefore the effects of gravity (*i.e.* buoyancy) must be consid-

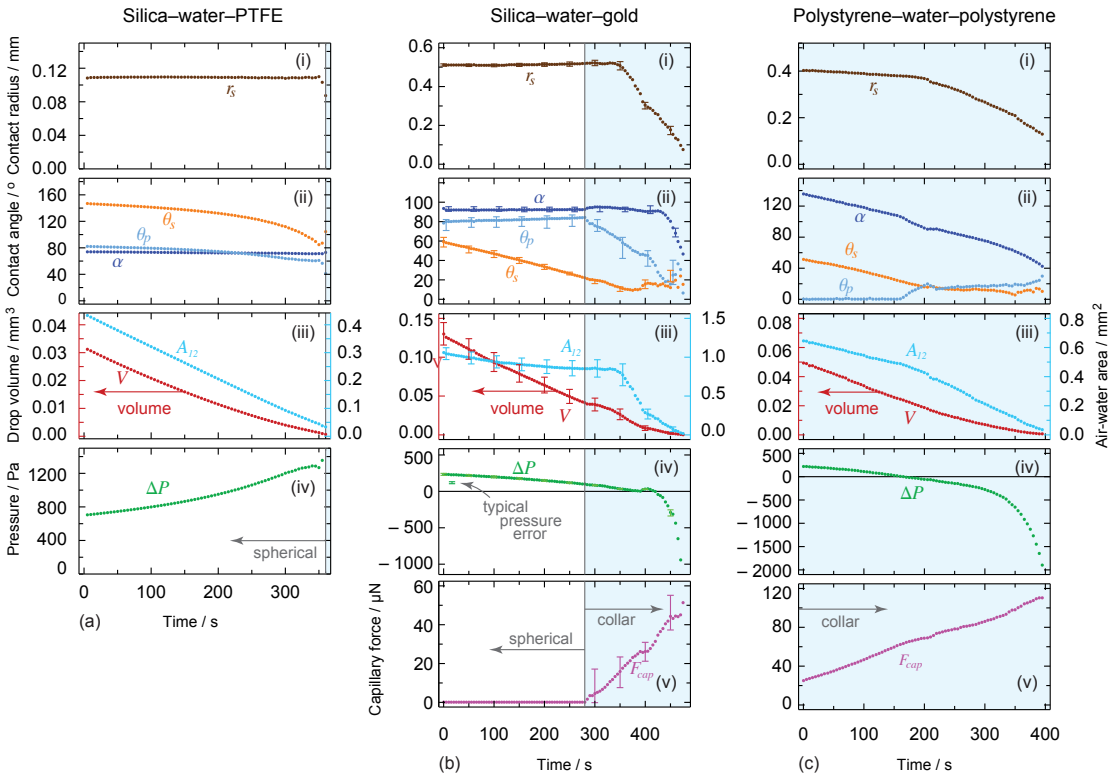

Figure 3.6: Time variations of (i) the drop substrate contact radius, (ii) the contact angles at both the substrate θ_s and particle θ_p together with the filling angle α which the meniscus makes with the centre of the particle measured through the water, (iii) the volume of the water drop (left hand axes) and the air-water interfacial area (right hand axes), (iv) the Laplace pressure across the interface and (v) the (attractive) capillary force between the particle and the substrate for each of the three experiments presented in Fig. 3.3. From left to right, the extracted quantities correspond to the experiments shown in Fig. 3.3a, b and c, respectively. All quantities were extracted by fitting the theoretical solution to the experimental photographs (the blue shaded region represents the evaporation regions where the drop is an axisymmetric collar around the particle-substrate contact). Representative error bars are shown on the centre column plots.

ered, even though the gravitational force is several orders of magnitude smaller than the capillary force (gravitational force / capillary force = Bond number ~ 0.01).[‡]

When the particle is more dense than both liquid phases, the particle will experience a downward net force, positioning it either axisymmetrically at the nadir of a pendant drop, or asymmetrically to the side of a sessile drop. This effect is demonstrated in Fig. 3.3 and 3.5, where experiments 1 and 2 (Fig. 3.3a and b) show a heavy silica particle at the apex of a pendant drop, while Fig. 3.5 shows the particle at the base of a spherical sessile drop. The reverse is true for a particle less dense than both liquid phases. For the intermediate case, it is possible to find a volume dependant expression to determine the particle position. Details of this calculation are provided in Appendix 3.A.

[‡]Bond number $= (L/\lambda)^2$, where λ is the capillary length and L is a typical length scale for the system ($L \sim 200\mu$m).

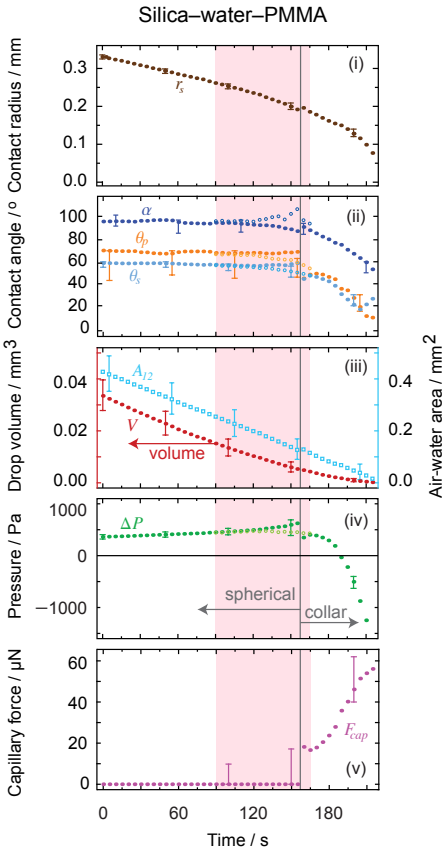

Figure 3.7: Silica-water-PMMA: Time variations of (i) the substrate contact radius, (ii) the contact angle at both the substrate θ_s and at the particle θ_p together with the filling angle α, (iii) the drop volume (solid symbols, left hand axis) and air-water interfacial area (open symbols, right hand axis), (iv) the Laplace pressure of the evaporating drop and (v) the (attractive) vertical capillary force between the particle and the substrate. The vertical line at 160 s separates the spherical interface regime (left hand side) from the axisymmetric collar region (right hand side). The shaded red region represents the region where the experimental system deviates from the theoretical solution due to surface non-ideality. The open circles in this region show quantities extracted by considering the local behaviour of the interface. Representative error bars are shown in each plot.

It is clear that the initial condition adopted is a direct result of both the relative volumes of particle and drop, and the system surface chemistry (that is, the contact angle on both the substrate and particle). Exemplar are the cases of a silica particle and water drop on a PTFE or polystyrene surface (Fig. 3.3a and c). Due to the high water contact angle of the PTFE substrate, a spherical interface with small contact radius is favoured throughout, whereas the less hydrophobic polystyrene results in collars with large contact radii.

3.3.2 Boundary conditions

The theory presented above was derived for the boundary condition of either a pinned contact line where the initial liquid-solid contact line is fixed and evapora-

tion results in a change in air-water-solid contact angle; or a constant contact angle where the liquid-solid contact line is free to move and retain the thermodynamically favoured air-water-solid contact angle. In reality however, the boundary condition for a given system depends largely on the microscopic geometry and surface chemistry of both surfaces, and a combination of both pinned contact line and constant contact angle cases may be observed within the same experiment. For the systems explored here, the situation is further complicated by the different solid geometries (*i.e.* a curved particle and flat substrate) and dissimilar material combinations chosen to emphasise the importance of wetting effects.

For the axisymmetric systems presented, throughout the spherical evaporation process the three-phase contact at the substrate has a pinned contact line (see uppermost panels in Fig. 3.6), while the particle contact condition is not as easily determined with the same precision due to its geometry and freedom of rotation. Given that the particle contact radius remains constant well into the collar mode of evaporation, it appears that the contact line at the particle is also pinned.

Perhaps the clearest case is that of silica-water-PTFE (experimental images shown in Fig. 3.3a, with the extracted physical quantities shown in Fig. 3.6a), where the drop contact radius on the substrate is effectively constant throughout the entire evaporation process, resulting in an increasingly pronounced decrease in substrate contact angle as evaporation proceeds. Similar behaviour is seen for the early, spherical stages of the silica-water-gold experiment (experimental images and extracted physical quantities shown in Fig. 3.3b and 3.6b, respectively), although after the particle touches the substrate and collar configurations become applicable, accompanied with significant changes in the position of the contact line. Most notably, the drop contact line on the substrate de-pins, with the substrate contact condition transitioning to a constant contact angle ($\sim 15\ ^\circ$).

In the case of polystyrene-water-polystyrene (experimental images and extracted physical quantities shown in Fig. 3.3c and 3.6c, respectively), the boundary conditions are not as clearly defined during the experiment, as the contact angles and contact radius both change throughout. Perhaps most interestingly, there is a discontinuity in both of these parameters at a distinct point that appears to be consistent with the inversion of the droplet Laplace pressure from positive to negative. This results in a more rapid retraction of the contact radius, although this may also be connected to the low substrate contact angle ($< 20\ ^\circ$) at this stage.

If the pinned contact line condition applies at both the particle and the substrate, it is possible to find the rate at which the contact angles at the substrate and particle vary with respect to each other by differentiating eqn (3.3), which gives

$$\frac{\mathrm{d}\theta_\mathrm{p}}{\mathrm{d}\theta_\mathrm{s}} = \frac{\tan(\alpha + \theta_\mathrm{p})}{\tan\theta_\mathrm{s}}. \tag{3.20}$$

This useful relation predicts the direction of change of contact angle for given surface chemistries. Importantly, for the silica-water-gold experiment, $\mathrm{d}\theta_\mathrm{p}/\mathrm{d}\theta_\mathrm{s} \sim -0.1$, which implies that for θ_s to decrease by 40 °, the particle contact angle will *increase* by 4 °, accurately matching the presented theory. This relationship also predicts that for the silica-water-PTFE experiment the particle contact angle decreases with decreasing substrate contact angle ($\mathrm{d}\theta_\mathrm{p}/\mathrm{d}\theta_\mathrm{s} \sim 0.6$), which matches experimental data.

Perhaps most curiously, the case of a silica particle-sessile water drop composite on a spun coated poly(methylmethacrylate) (PMMA) surface (Fig. 3.5) shows a constant contact angle during most of its evaporation process, and for all of the states in which the drop adopts a spherical interface (Fig. 3.7). However, the contact angles at both particle and surface appear to pin at the point when collar geometries are formed, associated with both a decrease and sign change in Laplace pressure and a strong capillary force between the particle and surface. The reasons for this change in boundary condition are not entirely clear, but appear to be associated with the evaporation dynamics, as the volume and surface area continue to change smoothly despite the abrupt changes in contact angle and capillary force. It is conceivable that in diffusion-driven evaporation, the system contact angles must adjust to maintain the correct pressure-to-surface area ratio, although further experiments would be required to understand this more fully. A more decisive analysis is thwarted by minor deviations from ideality (shown as the shaded region in Fig. 3.7) wherein uncertainties arise due to minor asymmetric pinning of both the particle and substrate contact lines.

3.3.3 Capillary force

When the drop interface is spherical, there is no force acting on the particle. For an axisymmetric collar, however, the interface exerts a force on the particle. Orr *et al.* [27] showed theoretically that depending on the drop volume, the resulting capillary force could be either attractive or repulsive. The spherical solution separates these two cases, as it results in no capillary force.

As shown in the theory section, when the drop volume is above the critical volume, the configuration can either form a spherical interface, or a collar interface exerting a repulsive capillary force on the particle. Clearly the case of a repulsive capillary force is only physical in the instance that the particle is 'held' onto the surface, otherwise the system will revert to the energetically favoured spherical interface.

We can compare the surface energies of the two configurations by first taking the particle to sit axisymmetrically at the apex of a spherical drop. If the particle is then

moved toward the substrate to form an axisymmetric collar, the potential energy, U, of the system has been increased since $\mathrm{d}U/\mathrm{d}z = -F_{\mathrm{capillary}}$ with the capillary force acting in the opposite direction to the displacement. For an idealised system, conservation of energy results in an increase in the surface energy. Since each of the interfacial areas (and therefore the interfacial energies) for a spherical interface are independent of the position of the particle at the apex or base of the drop, we find the important result that the spherical drop interface is more energetically favourable than the axisymmetric collar for drop volumes above the critical volume. Therefore for a drop volume above the critical volume, a spherical interface will be formed with no capillary force acting on the particle. As the drop volume decreases below the critical volume, an axisymmetric collar is formed with an attractive capillary force between the particle and the substrate.

The capillary force for evaporating particle-drop-substrate geometries analysed here follows expected behaviour based on interfacial curvature (Fig. 3.6). For silica-water-PTFE, the large substrate contact angle results in drop geometries that are spherical and convex until the final experimental photograph shown. It is possible that a very small liquid bridge (that cannot be visually resolved) still remains between the particle and the surface at the end of the experiment. This would explain why the particle remains adhered to the substrate despite the gravitational force acting to remove it. Such microscopic capillary bridges have been indicated before as an explanation for large adhesion forces seen for particles at substrates [44]. For silica-water-gold where the drop is pendant, the system transitions from a spherical interface to a collar, and in doing so experiences an attractive capillary force that rises approximately linearly from 0 to ~ 50 μN. The same is true for a silica particle on a sessile drop upon a PMMA substrate (Fig. 3.7). For polystyrene-water-polystyrene, the droplet configuration is an axisymmetric collar throughout, and thus the particle experiences a continual attractive capillary force, again with a nearly linearly increasing trajectory from $\sim 20 - 110$ μN.

Orr *et al.* [27] calculated the capillary force between a particle and a surface for a liquid bridge whose volume tends to zero. They calculated the maximal capillary force

$$F_{\mathrm{capillary}}^{\mathrm{max}} = 2\pi\gamma a\left(\cos\theta_{\mathrm{s}} + \cos\theta_{\mathrm{p}}\right) \leq 4\pi\gamma a \tag{3.21}$$

giving a maximum value of 75 μN for the silica particle, and 120 μN for the polystyrene particle, which agrees well with the maximum capillary forces calculated for our experiments.

For comparison, the force on the silica particle due to gravity (*i.e.* the weight) $F = \rho V g \sim 50$ nN, which is 3 orders of magnitude smaller than the capillary force. Thus for the length-scales studied here (and below these dimensions), capillary

interactions are enormous compared to gravitational interactions, and even more so for very small capillary bridges. This explains how a comparatively massive particle can be held up by a pendant drop that is a small fraction of its volume. The relative strengths of these interactions are undoubtedly important in the precise evaporative (self) assembly of colloidal particles.

3.3.4 Evaporation dynamics

Having developed a comprehensive theoretical understanding of the configuration of a static particle-drop-substrate system, it is pertinent to extend this to explore the dynamics of the droplet evaporation, a central theme for real-life systems in which particle-drop-surface attachments are encountered.

Starting from the analysis of a 'naked' sessile drop evaporating under diffusion-limited conditions as provided by Picknett and Bexon [40], we can compare our experiments wherein a particle is placed at the interface. For the pinned contact line case, eqn (3.15) gives a universal curve for the contact angle θ_s in terms of the scaled time $\bar{t}$. By taking the time when the drop vanishes to be 0 then gives $\theta_s(\bar{t}) = G^{-1}(-\bar{t})$, which allows the evolution of θ_s for the spherical drops in Fig. 3.3a and b to be compared to the theory for a naked sessile drop. For each experiment, the initial and final contact angles set the initial and final scaled time and hence the time scale, t_s. The substrate contact angle evolution with respect to the scaled time is presented in Fig. 3.8, showing good agreement between theory and both the silica-water-PTFE and silica-water-gold. Similarly, the evolution of the substrate contact radius for the constant contact angle case can be compared to eqn (3.18), and is presented in Fig. 3.5b. Both time scale expressions comprise the unconstrained diffusion rate parameter, $D(c_s - c_\infty)$, with the values used in scaling each of the experiments shown in Table 3.1. It is clear that within the experimental uncertainty inherent in the extraction of parameters from image fitting, the evaporation dynamics of spherical interfaces with a particle present are indistinguishable from the equivalent 'naked' sessile or pendant drops for both gold and PTFE surfaces.

Table 3.1: Diffusion rate parameters used in modelling droplet evaporation rate for the pinned contact line (PCL) and the constant contact angle (CCA) systems.

Experiment	PCL/CCA	$D(c_s - c_\infty)$/kg m^{-1} s^{-1}
Silica-water-PTFE	PCL	0.7×10^{-7}
Silica-water-gold	PCL	1.3×10^{-7}
Silica-water-PMMA	CCA	1.3×10^{-7}

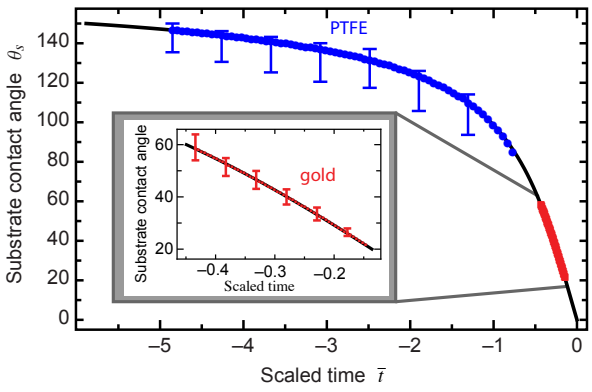

Figure 3.8: The evolution of the substrate contact angle θ_s for a 'naked' sessile drop with a pinned contact line undergoing diffusion-driven evaporation. The black curve represents the universal curve presented in eqn (3.15). The blue symbols are the substrate contact angles for the silica-water-PTFE experiment and the red symbols are the substrate contact angles for the silica-water-gold experiment, showing good agreement between the functional form of the drop-particle substrate contact evolution and that of a plain sessile drop.

Having established that the evaporation of the liquid bridge can be described by the evolution of a 'naked' sessile drop, we consider the evaporation when the liquid bridge is in an axisymmetric collar configuration. The silica-water-gold and silica-water-PMMA experiments demonstrate both spherical and collar configurations at different drop volumes, and illustrate the differences between the two modes of evaporation. During the silica-water-gold experiment, both the particle and substrate contact lines are pinned, with the substrate contact angle decreasing linearly, while the particle contact angle variation is well described by eqn (3.20). Once the particle makes contact with the substrate, the particle contact angle rapidly decreases with both contact lines initially remaining pinned. Soon thereafter, as the pressure decreases to zero, the system reconfigures itself, with the substrate contact radius rapidly decreasing with a concomitant decrease in the air-water interfacial area. Finally, the Laplace pressure changes sign with the particle contact depinning. Throughout the collar phase, the capillary force acting on the particle increases in magnitude.

The polystyrene-water-polystyrene experiment illustrates the collar evaporation further, however the particle contact condition is different. Initially, the polystyrene is completely wetted by the particle, with the contact radius on the particle moving. Similar key behaviours are again observed; namely, the Laplace pressure decreasing to zero causes the system to reconfigure itself, after which point both contact angles remaining relatively constant. The capillary force between the particle and the substrate is also attractive and increasing in magnitude.

For the silica-water-PMMA experiment, the initial configuration is a spherical interface with the particle in contact with the substrate. The substrate contact

angle is initially constant ($\theta_s \sim 60$ °) with both the particle contact angle and radius remain constant within experimental uncertainty. Interestingly, 90 s into the evaporation process the experimental interface deviates from the spherical interface, however the interface is clearly not an axisymmetric collar either. This is apparently caused by pinning at both particle and substrate contacts, together with non-zero horizontal forces between the particle and the substrate, presumably resulting from surface non-ideality. For the frames between 90 s and 155 s, fitting spherical interfaces to these frames provides a broadly accurate estimate of the volume and interfacial area, but does not accurately capture local behaviour such as the contact angles and the curvature (and hence the Laplace pressure). To obtain a more accurate estimate of the contact angle and Laplace pressure, the curvature of the drop profile to the right of the particle was calculated (as pinning occurred primarily on the left side of the silica particle). These extracted quantities are plotted in open circles on both plots, with the pinning region indicated by the shaded red in Fig. 3.5 and 3.7.

The interfacial area decreases linearly with time for the entirety of the experiment, and is notably independent of the Laplace pressure which, unlike a 'naked' sessile drop, changes sign.

3.3.5 Implications and opportunities for surface chemistry

Having analysed the possible geometries available to particle–drop–surface composites, and the dynamics of their evolution as the drop evaporates, it becomes pertinent to highlight the opportunities that are apparent in system design and control.

Clearly surface chemistry and morphology is of overriding importance in determining the parameters that control the drop geometry - that is, contact angles *via* surface chemistry. However, the substrate also acts to determine the boundary condition - either pinned contact line (with a varying contact angle) or constant contact angle (with the contact line free to move). In the cases examined experimentally here we did not purposefully select materials with the expectation of different boundary conditions. For greater precision, it would be possible to use patterned or micro-engineered substrates to introduce surface chemical or physical heterogeneities in order to facilitate contact line pinning of the drop at a certain position. Similarly, particles with hemispheres that exhibit different wettabilities (Janus particles) could be advantageous in controlling the contact line and obtaining specific geometric characteristics.

3.4 Conclusion

We have analysed experimentally and theoretically the configurations available to a particle-droplet-substrate system. The preferred state can be easily predicted for any combination of fluid and particle densities, contact angles and volume ratios. An understanding of this behaviour is of great importance when designing systems that can take advantage of such composite colloids, such as evaporative lithography and microelectromechanical systems.

When comparing the measured geometry of real systems to the theoretical expectation, the effects of non-ideality become clear, and the extent of these departures from prediction vary depending on the surface chemistry of the systems used. In particular, the effects of liquid contact line pinning due to surface inhomogeneities are significant and have a strong influence over the geometries observed. In most cases, despite the effects of pinning, the theory can still be applied to obtain physical parameters with sufficient accuracy for most purposes. Significantly, for all systems, a critical volume is determined, below which a strongly attractive capillary force is 'switched on', providing unique opportunities for surface modification and assembly. In all cases explored here, and indeed for all low Bond numbers, surface tension forces dominate the behaviour of liquid bridges; however, when all other forces are balanced, gravity can still play a role in determining the geometry of the system (*i.e.* whether the particle rests at the base or apex of the drop).

Interestingly, an analysis of the liquid evaporation of these systems indicates that the presence of a particle at the interface has very little influence on the evaporation rate when compared to a 'naked' sessile drop, providing access to a well-understood description of evaporation dynamics. The existence of a remaining microscopic capillary bridge between the particle and surface that cannot be visualised in these experiments is posited, and remains to be experimentally investigated.

3.5 Bibliography

[1] S. U. Pickering, *J. Chem. Soc., Trans.*, 1907, **91**, 2001–2021.

[2] W. Ramsden, *Proc. R. Soc. Lond.*, 1903, **72**, 156–164.

[3] B. P. Binks and R. Murakami, *Nat. Mater.*, 2006, **2**, 865–869.

[4] P. Aussillous and D. Quéré, *Nature*, 2001, **411**, 924–927.

[5] E. Bormashenko, *Curr. Opin. Colloid Interface Sci.*, 2011, **16**, 266–271.

[6] G. McHale and M. I. Newton, *Soft Matter*, 2011, **7**, 5473–5481.

[7] R. Aveyard, B. D. Beake and J. H. Clint, *J. Chem. Soc., Faraday Trans.*, 1996, **92**, 4271–4277.

[8] S. Komura, Y. Hirose and Y. Nonomura, *J. Chem. Phys.*, 2006, **124**, 241104.

[9] H.-J. Butt, *J. Colloid Interface Sci.*, 1994, **166**, 109–117.

[10] P. Mulvaney, J. M. Perera, S. Biggs, F. Grieser and G. W. Stevens, *J. Colloid Interface Sci.*, 1996, **183**, 614–616.

[11] B. A. Snyder, D. E. Aston and J. C. Berg, *Langmuir*, 1997, **13**, 590–593.

[12] M. Preuss and H.-J. Butt, *Int. J. Miner. Process.*, 1999, **56**, 99–115.

[13] G. E. Yakubov, O. I. Vinogradova and H.-J. Butt, *J. Adhes. Sci. Technol.*, 2000, **14**, 1783–1799.

[14] J. Guzowski, M. Tasinkevych and S. Dietrich, *Phys. Rev. E*, 2011, **84**, 031401.

[15] Z. Fournier, D. Geromichalos, S. Herminghaus, M. Kohonen, F. Mugele, M. Scheel, M. Schulz, B. Schulz, C. Schier, R. Seemann and A. Skudelny, *J. Phys. Condens. Matter*, 2005, **17**, S477.

[16] C. Gögelein, M. Brinkmann, M. Schröter and S. Herminghaus, *Langmuir*, 2010, **26**, 17184–17189.

[17] R. K. Niven, *J. Pet. Sci. Eng.*, 2006, **52**, 1–18.

[18] T. K. Tokunaga, *Water Resour. Res.*, 2011, **47**, 8514.

[19] E. Koos and N. Willenbacher, *Science*, 2011, **331**, 897–900.

[20] T. Stifter, O. Marti and B. Bhushan, *Phys. Rev. B*, 2000, **62**, 13667–13673.

[21] J. S. McFarlane and D. Tabor, *Proc. R. Soc. Lond. A*, 1950, **202**, 224–243.

[22] H. Schubert, *Powder Technol.*, 1984, **37**, 105–116.

[23] Y. I. Rabinovich, J. J. Adler, M. S. Esayanur, A. Ata, R. K. Singh and B. M. Moudgil, *Adv. Colloid Interface Sci.*, 2002, **96**, 213–230.

[24] R. D. Piner, J. Zhu, F. Xu, S. Hong and C. A. Mirkin, *Science*, 1999, **283**, 661–663.

[25] K. J. Obata, T. Motokado, S. Saito and K. Takahashi, *J. Fluid Mech.*, 2004, **498**, 113–121.

[26] H.-J. Butt and M. Kappl, *Adv. Colloid Interface Sci.*, 2009, **146**, 48–60.

[27] F. M. Orr, L. E. Scriven and A. P. Rivas, *J. Fluid Mech.*, 1975, **67**, 723–742.

[28] J. Guzowski, M. Tasinkevych and S. Dietrich, *Eur. Phys. J. E*, 2010, **33**, 219–42.

[29] N. D. Denkov, O. D. Velev, P. A. Kralchevsky, I. B. Ivanov, H. Yoshimura and K. Nagayama, *Langmuir*, 1992, **8**, 3183–3190.

[30] N. D. Denkov, O. D. Velev, P. A. Kralchevsky, I. B. Ivanov, H. Yoshimura and K. Nagayama, *Nature*, 1993, **361**, 26–26.

[31] P. A. Kralchevsky and K. Nagayama, *Adv. Colloid Interface Sci.*, 2000, **85**, 145–192.

[32] I. U. Vakarelski, D. Y. C. Chan, T. Nonoguchi, H. Shinto and K. Higashitani, *Phys. Rev. Lett.*, 2009, **102**, 058303.

[33] I. U. Vakarelski, J. O. Marston and S. T. Thoroddsen, *Langmuir*, 2013, **29**, 4966–4973.

[34] V. N. Manoharan, M. T. Elsesser and D. J. Pine, *Science*, 2003, **301**, 483–487.

[35] F. Fan and K. J. Stebe, *Langmuir*, 2004, **20**, 3062–3067.

[36] S. Watanabe, K. Inukai, S. Mizuta and M. T. Miyahara, *Langmuir*, 2009, **25**, 7287–7295.

[37] A. K. Geim, S. V. Dubonos, I. V. Grigorieva, K. S. Novoselov, A. A. Zhukov and S. Y. Shapoval, *Nat. Mater.*, 2003, **2**, 461–463.

[38] D. L. Hu and J. W. M. Bush, *Nature*, 2005, **437**, 733–736.

[39] M. J. Neeson, R. F. Tabor, F. Grieser, R. R. Dagastine and D. Y. C. Chan, *Soft Matter*, 2012, **8**, 11042–11050.

[40] R. Picknett and R. Bexon, *J. Colloid Interface Sci.*, 1977, **61**, 336–350.

[41] S. Dash and S. V. Garimella, *Langmuir*, 2013, **29**, 10785–95.

[42] H. Gelderblom, A. G. Marín, H. Nair, A. van Houselt, L. Lefferts, J. H. Snoeijer and D. Lohse, *Phys. Rev. E*, 2011, **83**, 026306.

[43] G. McHale, S. M. Rowan, M. I. Newton and M. K. Banerjee, *J. Phys. Chem. B*, 1998, **102**, 1964–1967.

[44] J. C. Contreras-Naranjo and V. M. Ugaz, *Nat. Commun.*, 2013, **4**, 1919.

3.A Particle position

In this section we calculate the centre of mass of a particle-spherical interface system, which then determines the force acting on the particle and hence the position of the particle on the spherical interface.

We consider a spherical drop with a particle attached to its interface as depicted in Fig. 3.9. We begin by considering a particle which is sitting at the zenith of the

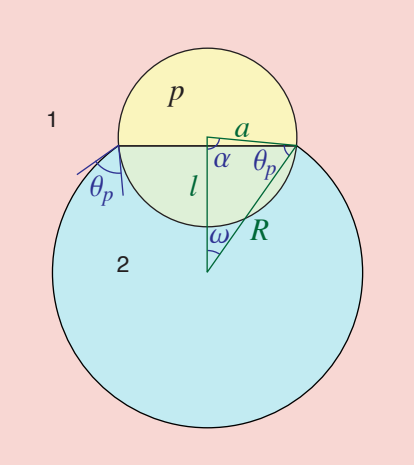

Figure 3.9: A spherical particle p attached to the interface of a spherical drop of fluid 2, surrounded by outer phase 1.

drop. Taking the axes origin to be the centre of the drop, we denote the centre of mass of the system d, measured in the positive z direction. By symmetry about the z-axis, the centre of mass will be $\mathbf{c} = (0, 0, d)$, where

$$\begin{aligned}\mathbf{c} &= \iiint \boldsymbol{x}\,\rho(\boldsymbol{x})\;dV \Big/ \iiint \rho(\boldsymbol{x})\;dV \\ &= \frac{\iiint_{\text{particle}} \boldsymbol{x}\,\Delta\rho_{1\text{p}}\;dV + \iiint_{\text{fluid 2}} \boldsymbol{x}\,\Delta\rho_{12}\;dV}{\Delta\rho_{1p}\iiint_{\text{particle}} dV + \Delta\rho_{12}\iiint_{\text{fluid 2}} dV}\end{aligned} \tag{3.22}$$

where $\Delta\rho_{ij} \equiv \rho_j - \rho_i$ is the difference between the two densities for phase i and j. The quantity d can be written as the weighted average of the centre of mass for both the drop d_2 and the particle d_p

$$d = \frac{\Delta\rho_{1\text{p}} V_\text{p} d_\text{p} + \Delta\rho_{12} V_2 d_2}{\Delta\rho_{1\text{p}} V_\text{p} + \Delta\rho_{12} V_2} \tag{3.23}$$

where V_2 and V_p are the volumes of the drop and the particle, respectively. In the preceding expression the quantity V_2 is the volume of the supporting drop 2. To simplify the expression for d_2 we add and subtract a volume of fluid corresponding to the fluid removed by the presence of the particle (denoted by the $e \equiv e_1 + e_2$),

which is depicted in Fig. 3.10. This allows d to be written

$$d = \frac{\Delta\rho_{1\mathrm{p}} V_{\mathrm{p}} d_{\mathrm{p}} + \Delta\rho_{12}(V_{2+e} d_{2+e} - V_e d_e)}{\Delta\rho_{1\mathrm{p}} V_{\mathrm{p}} + \Delta\rho_{12} V_2}. \tag{3.24}$$

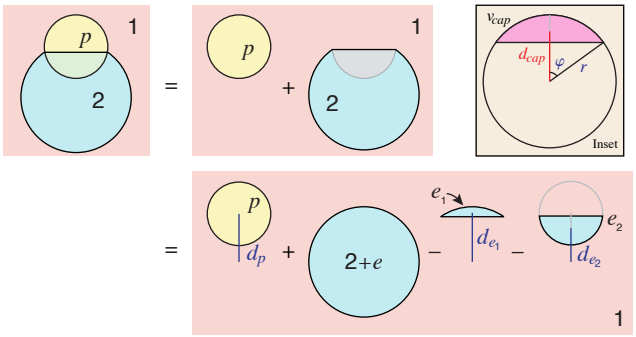

Figure 3.10: A cartoon depicting the initial particle drop system split into a series of different domains to facilitate the calculation of the centre of mass of the system. Inset: A spherical cap with volume v_{cap} and centre of mass d_{cap} formed by taking a portion of a sphere of radius r, with subtended angle φ.

The centre of mass of the newly formed body $2 + e$ is simply the centre of mass of a sphere centred at the origin, which is zero.

All the quantities in the preceding expression for the centre of mass can be expressed in terms of the volume v_{cap} and centre of mass d_{cap} of a spherical cap, which can be written

$$v_{\mathrm{cap}}(r, \varphi) = \frac{\pi r^3}{3}(2 - 3\cos\varphi + \cos^3\varphi) \tag{3.25a}$$

$$d_{\mathrm{cap}}(r, \varphi) = \frac{3r}{4}\frac{(1 + \cos\varphi)^2}{2 + \cos\varphi} \tag{3.25b}$$

where r is the radius of the sphere and φ is the subtended angle, as illustrated in Fig. 3.10.

By applying the law of cosines to the angle formed between the centre of the particle, the centre of the supporting spherical interface, and the three phase contact allows the distance between the two particles l, and the filling angle α to be expressed in terms of the drop radius

$$l^2 = a^2 + R^2 - 2aR\cos\theta_{\mathrm{p}} \tag{3.26a}$$

$$R_2 = a^2 + l^2 - 2al\cos\alpha. \tag{3.26b}$$

Finally, the centre of mass of the system can be expressed as

$$d = \frac{\Delta\rho_{1\mathrm{p}} V_\mathrm{p} d_\mathrm{p} - \Delta\rho_{12}(V_{e_1} d_{e_1} + V_{e_2} d_{e_2})}{\Delta\rho_{1\mathrm{p}} V_\mathrm{p} + \Delta\rho_{12} V_2} \tag{3.27}$$

where the expressions for volume and centre of mass of each of the regions is given by

$$V_\mathrm{p} = \frac{4\pi}{3} a^3 = v_\mathrm{cap}(a, \pi) \qquad d_\mathrm{p} = l \tag{3.28a}$$

$$V_{e_1} = v_\mathrm{cap}(R, \omega) \qquad d_{e_1} = d_\mathrm{cap}(R, \omega) \tag{3.28b}$$

$$V_{e_2} = v_\mathrm{cap}(a, \alpha) \qquad d_{e_2} = d_\mathrm{p} - d_\mathrm{cap}(a, \alpha) \tag{3.28c}$$

$$V_2 = \frac{4\pi}{3} R^3 - (V_{e_1} + V_{e_2}) \qquad d_2 = 0, \tag{3.28d}$$

together with the introduction of the angle $\omega = \pi - (\alpha + \theta_\mathrm{p})$. Substituting these expressions into eqn (3.27), and noting that

$$d_\mathrm{cap}(r, \varphi)\, v_\mathrm{cap}(r, \varphi) = \frac{\pi}{4} r^4 \sin^4 \varphi \tag{3.29}$$

then gives

$$d = l\, \frac{\Delta\rho_{1\mathrm{p}} v_\mathrm{cap}(a, \pi) - \Delta\rho_{12} v_\mathrm{cap}(a, \alpha)}{\Delta\rho_{1\mathrm{p}} V_\mathrm{p} + \Delta\rho_{12} V_2} \tag{3.30}$$

where we have used the equality of $R \sin\omega = a \sin\alpha$ by applying the Law of Sines to the triangle formed in Fig. 3.9.

This configuration can be rationalised as a particle rotating with its centre distance l from the centre of the spherical drop. The centre of mass of this system acts at some distance d from the centre of the drop, with gravity acting on a volume of effective mass $m_\mathrm{eff} = \Delta\rho_{1\mathrm{p}} V_\mathrm{p} + \Delta\rho_{12} V_2$, with a force $m_\mathrm{eff}\, g$. This means that the gravitational force acting on particle will be either upwards or downwards, depending on the sign of the expression $S(\alpha)$, which is

$$S(\alpha) = \Delta\rho_{12} \bar{v}_\mathrm{cap}(\alpha) - \Delta\rho_{1\mathrm{p}} \bar{v}_\mathrm{cap}(\pi), \tag{3.31}$$

where $\bar{v}_\mathrm{cap}(\varphi)$ is the scaled cap volume $\bar{v}_\mathrm{cap}(\varphi) \equiv v_\mathrm{cap}(r, \varphi)/r^3$, and we have used the property that $l > 0$.

This result can be applied to the particle-drop-substrate configuration as follows. If a sessile drop is formed on the substrate, positive S will result in a gravitational force acting upwards on the particle, ultimately positioning the particle axisymmetrically at the drop apex. Conversely, for negative S the particle will experience a force downward, positioning it at the substrate. The opposite result holds for a pendant drop.

Interestingly, the above expression is dependant on the filling angle α, which in turns depends on the drop radius and hence the drop volume. It is therefore possible for a particle initially at the apex of the supporting drop to reposition itself at the substrate partway through the evaporation of the supporting drop.

3.B Supplementary videos

We include four movies of the evaporation of a water capillary bridge formed between a particle and a substrate:

1. Movie 1 – a silica particle below a PTFE substrate
2. Movie 2 – a silica particle below a gold substrate
3. Movie 3 – a polystyrene particle above a polystyrene substrate
4. Movie 4 – a silica particle above a PMMA substrate.

These videos are available via the Internet at http://doi.org/10.1039/c4sm01826e.

CHAPTER 4

Pendant drop tensiometry

The interfacial tension is an important quantity that represents the excess energy associated with molecules at the interface (discussed in Section 6.2). This excess energy causes drops to adopt geometries that tend to minimise their interfacial area. The magnitude of the interfacial tension, therefore, directly affects the resulting drop shape. In addition, when three phases meet, a three-phase contact line is formed with its local geometry determined by the relative magnitudes of the associated interfacial tensions. This is particularly pertinent to compound drops since, as investigated in Chapter 2 and Chapter 3, the local geometry of the three-phase contact plays a crucial role in determining the overall drop configuration.

Given the quantitative importance of the interfacial tension, accurately measuring it is essential. This chapter investigates interfacial tensiometry, beginning with a discussion of a variety of common techniques and their associated advantages and disadvantages. The aim of this section is to emphasise the underlying physics of each method. Consequently, this discussion focuses on 'ideal' systems, with generalisations and correction factors included in the references.

One of the techniques discussed is the pendant drop tensiometer. This method is advantageous as it has wide applicability, requires only a small amount of liquid, operates on versatile timescales and requires a very simple experimental apparatus. However, it is difficult to implement as it requires a robust routine to fit the theoretical drop profile to an experimental photograph.

For the remainder of this chapter, we detail the expressions required to perform this fitting routine, ultimately facilitating pendant drop tensiometry.

4.1 Measuring interfacial tension

We now detail a selection of commonly used and commercially available interfacial tensiometers. Fig. 4.1 provides a schematic of these methods. Each technique relies on a force balance to measure the unknown interfacial force from another known force. The interfacial tension is then determined by equating the inferred interfacial force with the known functional form, which depends on the interfacial tension.

For the Wilhelmy plate and the du Noüy ring, an applied force balances the capillary force. For the maximum bubble pressure and the capillary rise methods, the Laplace pressure is equated to the known pressure across the interface. The spinning drop method balances the centrifugal forces that act to elongate the drop with the interfacial forces that act to minimise the interfacial area, while for a deformed pendant drop, the gravitational deformations due to the drop weight balance the interfacial forces.

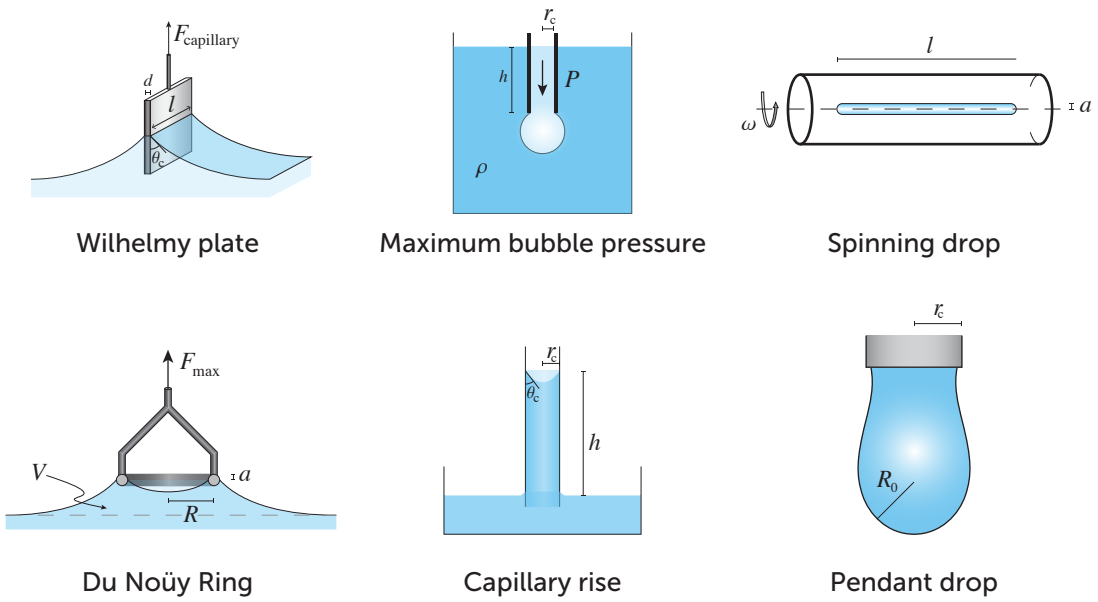

Figure 4.1: A schematic illustrating a variety of commonly used interfacial tensiometers.

In this section we briefly describe each of these techniques to aid our discussion. Detailed reviews are available [1, 2, 3, 4, 5].

Throughout these summaries, the density difference $\Delta\rho \equiv \rho_{in} - \rho_{out}$ is defined to be the inner density minus the outer density, g is the gravitational acceleration and $\lambda_c = \sqrt{\Delta\rho g/\gamma}$ is the capillary length associated with the interface, see Section 6.3.4 for more details. The lengths associated with each method are illustrated in Fig. 4.1.

4.1.1 Wilhelmy plate

The Wilhelmy plate method [6] measures the force exerted by a liquid interface on a plate to determine the interfacial tension. A plate of length l, thickness d and height h is placed vertically into a liquid, with the plate connected to a microbalance. The known form of the capillary force acting on the plate can be equated to the measured capillary force, which is determined through a force analysis.

The weight of the plate is $F_{\text{weight}} = \rho_{\text{p}} g V_{\text{p}}$, where $V_{\text{p}} = lhd$ is the volume of the plate, while the liquid displaced by the plate exerts a buoyancy force $F_{\text{buoy}} = \rho_{\text{l}} g V_{\text{disp}}$, where V_{disp} is the volume of displaced liquid below the horizontal surface. In the preceding terms, ρ_{l} and ρ_{p} denote the density of the liquid and the plate, respectively. Using these expressions, the capillary force on the plate can be expressed in terms of the force measured by the microbalance,

$$F_{\text{capillary}} = F_{\text{measured}} - F_{\text{weight}} + F_{\text{buoy}}. \tag{4.1}$$

The capillary force exerted on the plate is $p\gamma \cos\theta_{\text{c}}$, where p is the perimeter of the contact line and θ_{c} is the contact angle at the plate. Rearranging then leads to an expression for the interfacial tension,

$$\gamma = \frac{F_{\text{capillary}}}{2(l+d)\cos\theta_{\text{c}}}. \tag{4.2}$$

In the preceding expression for the interfacial tension, both γ and the contact angle θ_{c} are unknown. Two common methods avoid the need to determine the contact angle. The first involves the use of a surface that is perfectly wetted by the liquid, resulting in $\cos\theta_{\text{c}} = 1$. However, such a surface will have a high surface energy and therefore is very susceptible to contamination. Platinum is commonly used as its surface can be easily regenerated by exposing it to a flame [1, 7]. The second method is to retract a plate with non-zero contact angle through the liquid, while measuring the capillary force throughout the retraction. The maximum capillary force will occur when the apparent contact angle is zero, thus determining γ.

4.1.2 Du Noüy ring

The du Noüy ring tensiometer [8, 9] determines the interfacial tension by directly measuring the capillary force acting on a thin, circular wire ring. We denote the radius of the ring R, and the ring wire radius a. For the ideal case where, compared to the capillary length λ_{c}, the ring is very large $R/\lambda_{\text{c}} \gg 1$ and the wire is very thin $a/\lambda_{\text{c}} \ll 1$, the maximum force exerted on the ring is equal to the interfacial tension

multiplied the perimeter of the contact line

$$F_{\max} = 4\pi R\gamma. \tag{4.3}$$

Harkins and Jordan [10] found this expression to be in serious error due to non-ideality in the wire ring dimensions. They introduced a correction factor f to account for non-zero wire thickness, and moderate ring radius, leading to the expression

$$\gamma = \frac{F_{\max}}{4\pi R} f\left(\frac{R^3}{V}, \frac{R}{a}\right) \tag{4.4}$$

where V is the volume of liquid above the horizontal liquid interface. Harkins and Jordan [10] calculated f empirically, while Freud and Freud [11] calculated f theoretically, finding good agreement with the empirical work. Huh and Mason [12] later provided a rigorous study of ring tensiometers, extending the range of applicability for the factor f.

4.1.3 Maximum bubble pressure

This method measures the interfacial tension by equating the Laplace pressure across an interface with the known pressures on both sides of the interface. We outline the method for the case of an air bubble, however the method can be extended to liquid-liquid systems.

An air bubble is formed below a capillary that is immersed in a body of liquid. The volume of the bubble is then increased, with the applied pressure measured. The surface tension is then calculated by equating the Laplace pressure across the bubble surface to the known pressures on either side

$$\Delta P \equiv P_{\text{in}} - P_{\text{out}} \tag{4.5}$$

where P_{in} equal to the applied pressure.

If the capillary radius r_{c} is much smaller than the associated capillary length λ_{c}, the bubble surface will form a portion of a sphere with radius R, where R is equal to the Laplace radius. The Laplace pressure is related to the Laplace radius according to

$$\Delta P = \frac{2\gamma}{R}. \tag{4.6}$$

If the capillary is immersed at a depth h within the liquid, the pressure outside the bubble is equal to the hydrostatic pressure $P_{\text{out}} = \rho g h$, where ρ is the density of the liquid.

As the air bubble is formed, the surface is initially close to being flat. Since the bubble interface is spherical, the associated Laplace radius is very large. As the

bubble volume increases, the Laplace radius decreases until it reaches a minimum at $R = r_c$, after which the Laplace radius then increases. Since the Laplace pressure is inversely proportional to R, see eqn (4.6), the maximum Laplace pressure is $\Delta P_{max} = 2\gamma/r_c$. Combining the known expressions for the pressures in eqn (4.5) results in an expression for the surface tension, in terms of the maximum applied pressure P_{max},

$$\gamma = \frac{r_c \left(P_{max} - \rho g h\right)}{2}. \tag{4.7}$$

When the gravitational deformations are not negligible (*i.e.* the capillary radius is comparable to the capillary length), the non-spherical shape of the interface must be accounted for. Correction factors for this method were calculated by Sugden [13], who used tables for the shape of the meniscus developed of Bashforth and Adams [14].

One of the most significant advantages of the maximum bubble method is its suitability for dynamic surface tension measurements. After a bubble reaches its maximum pressure, the pressure within the capillary will force the bubble to detach, thereby creating a fresh interface. This is particularly important for measuring interfacial tension during surfactant adsorption. By adjusting the flow rate within the capillary, the lifetime of a typical bubble, and thus the timescale for a dynamic interfacial tension measurements, can be varied from seconds to milliseconds [15].

4.1.4 Capillary rise

If a thin capillary tube is placed upright in a basin of liquid that wets the inside of the tube, a concave interface will form with a negative Laplace pressure (*i.e.* the pressure within the fluid will be less than the surrounding pressure). The liquid will rise within the tube until the Laplace pressure across the interface $\Delta P = -2\gamma/R$ is balanced by the hydrostatic pressure associated with the liquid rise $\rho g h$, where h is the height that the liquid rises within the capillary, measured to the apex of the drop inside the capillary. If the capillary is very thin (*i.e.* the capillary radius is much smaller than the capillary length, $r_c \ll \lambda_c$), the interface will be spherical with its radius equal to the Laplace radius $R = r_c/\cos\theta_c$, where θ_c is the contact angle within the tube. Equating the Laplace pressure with the hydrostatic pressure gives an expression for the interfacial tension

$$\gamma = \frac{\Delta\rho g h r_c}{2\cos\theta_c}. \tag{4.8}$$

In reality, it may not be possible to accurately determine the contact angle θ_c, in part because the curved capillary tube causes lensing of the interface. To overcome this issue, material choice and treatment is used to ensure the liquid wets the tube.

In the above derivation, the length scale was assumed to be much smaller than the capillary radius, thereby ensuring the sphericity of the bubble interface. However, as the capillary length of many liquids is typically only a few millimetres (for air-water $\lambda_c = 2.7$ mm), this condition may not be physically realisable. In this case, gravitational forces will deform the bubble, resulting in a non-spherical bubble interface. Although the bubble shape changes, the underlying physics remains the same. Lord Rayleigh [16] gave a series approximation in terms of r_c/h for a correction factor to eqn (4.8), valid when $r_c \lesssim h$. For larger capillary radii, Sugden [17] formed a general expression for γ by incorporating the shape of the deformed axisymmetric menisci from the tables of Bashforth and Adams [14].

4.1.5 Spinning drop

The spinning drop method measures the interfacial tension by equating interfacial forces with centrifugal forces. A small drop of liquid is formed within a second, denser liquid inside a cylindrical tube. The cylindrical tube is then rotated with an angular frequency ω of several thousand rotations per minute. This rotation introduces a centrifugal force that acts to elongate the drop. Elongating the drop, however, increases the interfacial area thereby increasing the interfacial energy.

This method was proposed by Vonnegut [18] in the limit where the drop radius a is much smaller than the drop length l, *i.e.* $a/l \ll 1$. To derive an expression for the interfacial tension, Vonnegut minimised the total energy of the drop, resulting in

$$\gamma = \frac{\Delta\rho\,\omega^2 a^3}{4}. \tag{4.9}$$

Later, Princen *et al.* [19] extended Vonnegut's original solution to account for drops with comparable radius and length, *i.e.* $a \sim l$.

This method is particularly well suited to measuring very low interfacial tensions. An example given by de Gennes *et al.* [7] notes, if a drop with volume 1 mm^3, density difference 100 kg m^{-3} and a rotation rate of 1000 rad s^{-1} is extended to a length of 1 cm, the corresponding interfacial tension is ~ 3 mN m^{-1} which is a typical value for oil-water systems in the presence of surfactants.

4.1.6 Pendant drop

In this technique the interfacial tension is determined by fitting the Young–Laplace equation to a pendant drop that is deformed by gravity, thus implicitly balancing the gravitational forces with interfacial forces.

In Section 6.3.5, we present the axisymmetric Young–Laplace equation, together with the non-dimensional Young–Laplace equation, scaled by the drop radius at the

apex R_0. This non-dimensional equation depends on a single dimensionless quantity, the Bond number Bo

$$\mathrm{Bo} = \frac{\Delta\rho g R_0^2}{\gamma}. \tag{4.10}$$

If the Bond number and the apex radius can be determined from the deformed pendant drop, the interfacial tension γ can be calculated from eqn (4.10).

This technique was first proposed over a century ago by Worthington [20, 21], however quantifying the Bond number proved difficult. More recently, advanced computer routines have been developed that fit the Young–Laplace equation to a pendant drop by minimising the sum of squared residuals between the theoretical drop profile, as predicted by the Young–Laplace equation, and the experimental drop profile [22, 23, 24, 25].

Pendant drop tensiometry provides an elegant method to calculate the interfacial tension. While this technique is experimentally straightforward, the computer routine to fit the Young–Laplace equation to an experimental drop photograph is not.

4.1.7 Summary of tensiometers

To conclude the discussion of interfacial tensiometers, Table 4.1 summarises the advantages and disadvantages associated with each method.

The pendant drop technique is particularly appealing as it has very wide applicability, the time scale of the measurement is versatile, it requires a small amount of liquid, and the experimental setup is particularly simple. Although pendant drop tensiometers are expensive, the experiment itself is relatively simple. The main barrier to implement this technique is the computational routine needed to fit the Young–Laplace equation to an experimental photograph of a pendant drop.

For the second part of this chapter, we derive the theoretical solution for the shape of an axisymmetric pendant drop, together with the expressions required to implement the fitting routine discussed in Section 6.4. This enables the pendant drop technique to be used with existing equipment (*i.e.* a camera and a syringe), significantly decreasing the costs of using this technique.

Table 4.1: A summary of the different methods used to measure surface and interfacial tension.

Method	Accuracy	Suitability for interfacial tension	Suitability for surfactants	Timescale	Experiment complexity	Cost of apparatus
Wilhelmy plate	$\sim$0.1 mN m^{-1}	Poor	Limited	10 s–10,000 s	Low	\$10,000–\$100,000
Du Noüy ring	$\sim$0.1 mN m^{-1}	Poor	Limited	10 s–10,000 s	Medium	\$5,000–\$25,000
Maximum bubble pressure	$\sim$0.01 mN m^{-1}	Good	Very good	0.1 s–10,000 s	Medium	\$15,000–\$80,000
Capillary rise	$\sim$0.1 mN m^{-1}	Poor	Good	0.1 s–100 s	Low	< \$100
Spinning drop	$\sim$0.001 mN m^{-1}	Very good	Very good	—	High	\$20,000
Pendant drop	$\sim$0.1 mN m^{-1}	Very good	Very good	10 s–10,000 s	Low	\$10,000–\$100,000

4.2 Pendant drop tensiometry

The ability to determine the interfacial tension from the shape of a deformed pendant drop was first proposed over a century ago [20, 21, 26]. In 1883, Bashforth and Adams [14] formed tables of approximate solutions to the axisymmetric Young–Laplace equation through the use of Taylor series. By varying the Bond number they developed numerical tables in terms of the tangent angle ϕ. Although their integrations were performed by hand, the techniques developed have formed numerical integration routines known as Bashforth–Adams methods.

In the 1940's, Andreas *et al.* [27] devised a simple approach for determining the Bond number. Their method was to calculate the ratio of two easily measured experimental quantities: the maximum drop diameter d_e, and the drop diameter d_s measured at a distance d_e from the apex. The ratio $S = d_s/d_e$ could then be compared to tables to determine the Bond number, from which the interfacial tension could be calculated.

Noting that numerically integrating the Young–Laplace equation is *"very laborious and unsatisfactory"*, Andreas *et al.* [27] developed tables for the ratio S in terms of the Bond number Bo experimentally. A decade later, Fordham [28] and Niederhauser and Bartell [29] independently calculated these tables numerically, showing the previous tables to be in error.

With the advent of computers, routines were developed to fit the Young–Laplace equation to the entire experimental drop profile, greatly increasing the accuracy of the method [22, 23, 24, 25]. These routines fit the Young–Laplace equation to the experimental drop profile by minimising the sum of squared residuals.

The Levenberg–Marquardt algorithm, detailed in Section 6.4.4, is well suited to performing this fitting procedure, as it is both robust and efficient [30, 31, 32, 33]. Implementing this method requires expressions for both the vector or residuals, and the Jacobian matrix.

In the next section we derive expressions for the residual vector and the Jacobian matrix. This allows the Canny edge detection algorithm and the Levenberg–Marquardt optimisation algorithm, both outlined in Section 6.4, to fit the theoretical pendant drop profile to an experimental photograph. The interfacial tension can then be calculated from the fitted parameters.

4.2.1 Theory

When a pendant drop of density ρ_d is formed within an outer phase, with density ρ, the drop interface is determined by the Young–Laplace equation. Introducing the cylindrical coordinates r and z, together with the tangent angle ϕ, allows the Young–Laplace equation to be written as a coupled set of differential equations in

terms of the arc length s. These variables are illustrated in Fig. 4.2.

The scaled axisymmetric Young–Laplace equation can be written as a set of coupled ordinary differential equations

$$\frac{\mathrm{d}\phi}{\mathrm{d}\bar{s}} = 2 - \mathrm{Bo}\,\bar{z} - \frac{\sin\phi}{\bar{r}} \tag{4.11a}$$

$$\frac{\mathrm{d}\bar{r}}{\mathrm{d}\bar{s}} = \cos\phi \tag{4.11b}$$

$$\frac{\mathrm{d}\bar{z}}{\mathrm{d}\bar{s}} = \sin\phi, \tag{4.11c}$$

where the length scale is taken to be the drop radius at the apex. This set of differential equations depends only on the Bond number Bo, defined

$$\mathrm{Bo} \equiv \frac{(\rho_\mathrm{d} - \rho)gR_0^2}{\gamma}. \tag{4.12}$$

A derivation of the scaled axisymmetric coupled differential equations that represent the Young–Laplace equation is included in Section 6.3.5. If the Bond number can be determined from a drop profile then, provided the two densities are known, the interfacial tension γ can be calculated from eqn (4.12). This outlines the mechanics of pendant drop tensiometers.

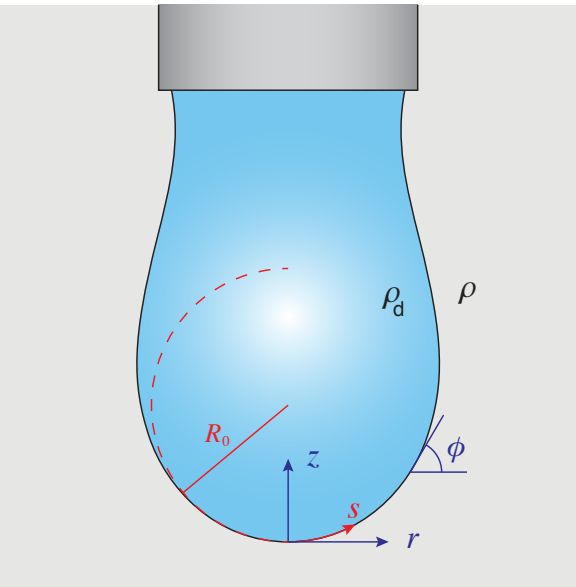

Figure 4.2: A schematic of a pendant drop below a capillary. Pendant drop tensiometers determine the interfacial tension by calculating the Bond number from a pendant drop that is deformed by gravity.

4.2.2 Method overview

Although the pendant drop method is conceptually straightforward, fitting the Young–Laplace equation to an experimental photograph requires a complex computer routine. This procedure can be divided into two subroutines: first, the drop profile is extracted from an experimental photograph, and second, the Young–Laplace equation is fitted to the extracted drop profile. We discuss each of these steps separately.

Determining the drop profile from an image is a standard problem of edge detection. As this is not the focus of the work, we provide a brief discussion of the Canny edge detection algorithm, however further details can be found in Section 6.4.1.

Fitting the Young–Laplace equation to the extracted drop profile is of use both in the present tensiometry work, but also in the other work presented in this thesis, as this process can be adapted to different drop geometries to fit the Young–Laplace equation. As we have shown in the earlier work in Chapter 2 and Chapter 3, important physical quantities can be calculated from the fitted parameters, thereby providing important insight into the physics underlying these systems. We discuss the fitting procedure in detail.

Image analysis

Initially, the experimental drop profile is extracted using the Canny edge detection algorithm [34]. Edges are detected by calculating gradients in the intensity of grayscale images, and returning the list of points where these gradients are sufficiently large. This is a standard edge detection routine and is freely available in many software packages.

To ensure this procedure accurately extracts edges, experiments should be performed to ensure a high contrast in the intensity of the drop and outer phase.

Fitting routine

The second step in the procedure is to fit the axisymmetric Young–Laplace equation to the extracted drop profile. We define the i^{th} residual e_i to be the minimum Euclidean distance between the i^{th} data point (r_i, z_i), and any point on the theoretical profile. We define the associated objective function S as the sum of squared residuals,

$$S = \sum_{i=1}^{n} e_i^2. \tag{4.13}$$

Since each residual is a function of the parameters $\boldsymbol{\beta} = \{X_0, Z_0, \omega, R_0, \mathrm{Bo}\}$, so too is the objective function $S = S(\boldsymbol{\beta})$. Fitting the theoretical profile to the

experimental drop has now been recast as a minimisation of the non-linear function $S(\boldsymbol{\beta})$.

The Levenberg–Marquardt algorithm, discussed in detail in Section 6.4.4, is well suited to perform this minimisation as it is both fast and robust. The variables $\widehat{\boldsymbol{\beta}} = \{\widehat{X}_0, \widehat{Z}_0, \widehat{\omega}, \widehat{R}_0, \widehat{\mathrm{Bo}}\}$ that minimise S are parameter estimates for the true values, where the circumflex denotes fitted parameters.

From the optimised parameters, the interfacial tension can be determined by rearranging eqn (4.12),

$$\gamma = \frac{\Delta\rho g \widehat{R}_0^2}{\widehat{\mathrm{Bo}}}. \tag{4.14}$$

The Levenberg–Marquardt iteratively updates the parameter set according to $\boldsymbol{\beta}^{(k+1)} = \boldsymbol{\beta}^{(k)} + \boldsymbol{\delta}$, where $\boldsymbol{\delta}$ is found by solving

$$\left(\mathbf{J}^{\mathrm{T}}\mathbf{J} + \lambda\,\mathrm{diag}(\mathbf{J}^{\mathrm{T}}\mathbf{J})\right)\boldsymbol{\delta} = -\mathbf{J}^{\mathrm{T}}\boldsymbol{e}. \tag{4.15}$$

In the preceding expression, $\boldsymbol{e}$ is the vector of residuals and $\mathbf{J}$ is the Jacobian matrix. The value of λ is chosen at each step to ensure convergence. A detailed discussion of the choice of λ, and the convergence criteria is given in Section 6.4.4.

In the next section, we derive expressions for the vector of residuals $\boldsymbol{e}$ and the Jacobian matrix $\mathbf{J}$.

4.2.3 Expressions for the residual vector and Jacobian matrix

The residual e_i associated with the i^{th} data point (r_i, z_i) is the minimum Euclidean distance between the given data point and any point on the theoretical drop profile $(r(s), z(s))$. The squared residual can be written in terms of the vertical component e_i^z, and the horizontal component e_i^r,

$$e_i^2 = \min_{\bar{s}} F_i(\bar{s}), \qquad F_i(\bar{s}) \equiv e_i^r(\bar{s})^2 + e_i^z(\bar{s})^2 \tag{4.16}$$

where $F_i(\bar{s})$ is the squared Euclidean distance between the i^{th} data point and a theoretical point at $\bar{s}$. The horizontal and vertical residuals between the (rotated) experimental data point and the theoretical curve are

$$\begin{aligned} e_i^r(\bar{s}) &= |(r_i - X_0)\cos\omega - (z_i - Z_0)\sin\omega| - R_0\,\bar{r}(\bar{s}) \\ &= \pm\{(r_i - X_0)\cos\omega - (z_i - Z_0)\sin\omega\} - R_0\,\bar{r}(\bar{s}) \qquad (4.17a) \\ e_i^z(\bar{s}) &= ((r_i - X_0)\sin\omega + (z_i - Z_0)\cos\omega) - R_0\,\bar{z}(\bar{s}) \qquad (4.17b) \end{aligned}$$

where the ambiguous sign in eqn (4.17a) is taken to ensure the expression in braces is positive. This arises due to axisymmetry of the drop.

We denote the arc length corresponding to the minimised residual for the i^{th} data point $\bar{s}_i$, *i.e.*

$$F_i(\bar{s}_i) \equiv \min_{\bar{s}} F_i(\bar{s}). \tag{4.18}$$

We proceed by deriving expressions for the residual vector and the Jacobian matrix, before discussing an iterative procedure for calculating the arc lengths $\bar{s}_i$ in the next section. The residual vector has elements

$$\boldsymbol{e}_i = \sqrt{e_i^r(\bar{s}_i)^2 + e_i^z(\bar{s}_i)^2} \tag{4.19}$$

while an expression for the Jacobian matrix can be determined from the chain rule

$$\begin{aligned}
\mathbf{J}_{ij} &= \frac{\partial e_i}{\partial \beta_j} && (4.20)\\
&= \frac{1}{2e_i}\frac{\partial}{\partial \beta_j}\left(e_i^2\right) && (4.21)\\
&= \frac{1}{2e_i}\frac{\partial}{\partial \beta_j}\left(e_i^{r\,2} + e_i^{z\,2}\right) && (4.22)\\
&= \frac{1}{e_i}\left(e_i^r\frac{\partial e_i^r}{\partial \beta_j} + e_i^z\frac{\partial e_i^z}{\partial \beta_j}\right) && (4.23)\\
&= \frac{1}{\sqrt{e_i^r(\bar{s}_i)^2 + e_i^z(\bar{s}_i)^2}}\left(e_i^r(\bar{s}_i)\left.\frac{\partial e_i^r}{\partial \beta_j}\right|_{\bar{s}_i} + e_i^z(\bar{s}_i)\left.\frac{\partial e_i^z}{\partial \beta_j}\right|_{\bar{s}_i}\right). && (4.24)
\end{aligned}$$

We now calculate the derivatives $\partial e_i^r/\partial\beta_j$ and $\partial e_i^z/\partial\beta_j$ by differentiating eqn (4.17) with respect to each of the parameters in $\boldsymbol{\beta} = \{X_0, Z_0, \omega, R_0, \mathrm{Bo}\}$:

$$\frac{\partial e_i^r}{\partial X_0} = \mp\cos\omega \tag{4.25a}$$
$$\frac{\partial e_i^z}{\partial X_0} = -\sin\omega \tag{4.25b}$$
$$\frac{\partial e_i^r}{\partial Z_0} = \pm\sin\omega \tag{4.26a}$$
$$\frac{\partial e_i^z}{\partial Z_0} = -\cos\omega \tag{4.26b}$$
$$\frac{\partial e_i^r}{\partial \omega} = \mp\left((r_i - X_0)\sin\omega + (z_i - Z_0)\cos\omega\right) \tag{4.27a}$$
$$\frac{\partial e_i^z}{\partial \omega} = \left((r_i - X_0)\cos\omega - (z_i - Z_0)\sin\omega\right) \tag{4.27b}$$
$$\frac{\partial e_i^r}{\partial R_0} = -\bar{r}(\bar{s}) \tag{4.28a}$$
$$\frac{\partial e_i^z}{\partial R_0} = -\bar{z}(\bar{s}) \tag{4.28b}$$
$$\frac{\partial e_i^r}{\partial \mathrm{Bo}} = -R_0\frac{\partial \bar{r}}{\partial \mathrm{Bo}} \tag{4.29a}$$
$$\frac{\partial e_i^z}{\partial \mathrm{Bo}} = -R_0\frac{\partial \bar{z}}{\partial \mathrm{Bo}} \tag{4.29b}$$

where the ambiguous sign in eqn (4.25a), (4.26a) and (4.27a) match the choice of sign in eqn (4.17a).

Each of these partial derivatives are known explicitly, except for the partial derivatives with respect to the Bond number in eqn (4.29a) and (4.29b). These

derivatives arise due to the implicit dependence the functions $\bar{r}$ and $\bar{z}$ have on the Bond number from eqn (4.11), with

$$\bar{r}(\bar{s}) \equiv \bar{r}(\bar{s}; \mathrm{Bo}), \qquad \bar{z}(\bar{s}) \equiv \bar{z}(\bar{s}; \mathrm{Bo}). \tag{4.30}$$

The partial derivatives with respect to the Bond number, eqn (4.29a) and (4.29b), must be determined by solving a coupled differential equation, formed by differentiating eqn (4.11) with respect to the Bond number Bo, and then interchanging the order of differentiation. This leads to a set of coupled partial differential equations. However, for constant Bo, these derivatives can be integrated numerically as a set of coupled ordinary differential equations

$$\frac{\mathrm{d}}{\mathrm{d}\bar{s}}\left(\left.\frac{\partial\phi}{\partial\mathrm{Bo}}\right|_{\mathrm{Bo}}\right) = -\bar{z} - \left.\frac{\partial\bar{z}}{\partial\mathrm{Bo}}\right|_{\mathrm{Bo}}\mathrm{Bo} - \left.\frac{\partial\phi}{\partial\mathrm{Bo}}\right|_{\mathrm{Bo}}\frac{\cos\phi}{\bar{r}} + \left.\frac{\partial\bar{r}}{\partial\mathrm{Bo}}\right|_{\mathrm{Bo}}\frac{\sin\phi}{\bar{r}^2} \tag{4.31a}$$

$$\frac{\mathrm{d}}{\mathrm{d}\bar{s}}\left(\left.\frac{\partial\bar{r}}{\partial\mathrm{Bo}}\right|_{\mathrm{Bo}}\right) = -\left.\frac{\partial\phi}{\partial\mathrm{Bo}}\right|_{\mathrm{Bo}}\sin\phi \tag{4.31b}$$

$$\frac{\mathrm{d}}{\mathrm{d}\bar{s}}\left(\left.\frac{\partial\bar{z}}{\partial\mathrm{Bo}}\right|_{\mathrm{Bo}}\right) = \left.\frac{\partial\phi}{\partial\mathrm{Bo}}\right|_{\mathrm{Bo}}\cos\phi. \tag{4.31c}$$

The boundary conditions at $\bar{s} = 0$ are $\bar{r} = 0$, $\bar{z} = 0$, $\phi = 0$, leading to boundary conditions for the differential equation (4.31)

$$\left.\frac{\partial\phi}{\partial\mathrm{Bo}}\right|_{\mathrm{Bo}} = 0, \quad \left.\frac{\partial\bar{r}}{\partial\mathrm{Bo}}\right|_{\mathrm{Bo}} = 0, \quad \left.\frac{\partial\bar{z}}{\partial\mathrm{Bo}}\right|_{\mathrm{Bo}} = 0 \qquad \text{at} \qquad \bar{s} = 0. \tag{4.32}$$

Calculating residuals: Newton–Raphson

We now outline the method used to calculate the arc length $\bar{s}_i$ that minimise the associated Euclidean distance between the i^{th} data point and the theoretical drop profile. From these arc lengths, the residual vector and the Jacobian matrix can be determined from eqn (4.19) and (4.24), respectively.

The arc length $\bar{s}_i$ is defined to minimise the Euclidean distance

$$F_i(\bar{s}_i) \equiv \min_{\bar{s}} F_i(\bar{s}) \tag{4.33}$$

where $F_i(\bar{s})$ is defined in eqn (4.16) and (4.17). A necessary condition for $F_i(\bar{s}_i)$ to be minimised is $F_i'(\bar{s}_i) = 0$. Introducing $f_i(\bar{s}) \equiv F_i'(\bar{s})$, together with eqn (4.11) and (4.17), then gives

$$f_i(\bar{s}) \equiv \frac{\mathrm{d}F_i}{\mathrm{d}\bar{s}} = \frac{\mathrm{d}}{\mathrm{d}\bar{s}}\left(e_i^r(\bar{s})^2 + e_i^z(\bar{s})^2\right) = 2\left(e_i^r\frac{\mathrm{d}e_i^r}{\mathrm{d}\bar{s}} + e_i^z\frac{\mathrm{d}e_i^z}{\mathrm{d}\bar{s}}\right) \tag{4.34}$$

$$= -2R_0\left(e_i^r(\bar{s})\cos\phi(\bar{s}) + e_i^z(\bar{s})\sin\phi(\bar{s})\right). \tag{4.35}$$

Minimising the function $F_i(\bar{s})$ is equivalent to calculating the root of $f_i(\bar{s})$. A fast root finding method is the Newton–Raphson algorithm. This algorithm iteratively updates the arc length $\bar{s}_i^{(k)}$ according to

$$\bar{s}_i^{(k+1)} = \bar{s}_i^{(k)} - \frac{f_i(\bar{s}_i^{(k)})}{f_i'(\bar{s}_i^{(k)})} \equiv \bar{s}_i^{(k)} - g_i(\bar{s}_i^{(k)}), \tag{4.36}$$

where we have introduced the function $g_i(\bar{s})$. This iteration is repeated until the arc length converges to within a specified tolerance, *i.e.* $|\bar{s}_i^{(k+1)} - \bar{s}_i^{(k)}| \equiv |g_i(\bar{s}_i^{(k)})| < \text{tol}$.

The iteration step in eqn (4.36) requires an expression for $f_i'(\bar{s})$, thus

$$f_i'(\bar{s}) = 2R_0 \frac{\mathrm{d}}{\mathrm{d}\bar{s}} \left(-e_i^r(\bar{s}) \cos\phi(\bar{s}) - e_i^z(\bar{s}) \sin\phi(\bar{s})\right) \tag{4.37}$$

$$= 2R_0 \left\{ R_0 \frac{\mathrm{d}\bar{r}}{\mathrm{d}\bar{s}} \cos\phi(\bar{s}) + R_0 \frac{\mathrm{d}\bar{z}}{\mathrm{d}\bar{s}} \sin\phi(\bar{s}) + \frac{\mathrm{d}\phi}{\mathrm{d}\bar{s}} \left(e_i^r(\bar{s}) \sin\phi(\bar{s}) - e_i^z(\bar{s}) \cos\phi(\bar{s})\right) \right\} \tag{4.38}$$

$$= 2R_0 \left\{ R_0 + \frac{\mathrm{d}\phi}{\mathrm{d}\bar{s}} \left(e_i^r(\bar{s}) \sin\phi(\bar{s}) - e_i^z(\bar{s}) \cos\phi(\bar{s})\right) \right\} \tag{4.39}$$

where we have used eqn (4.11), (4.17) and (4.35). Combining eqn (4.35), (4.36) and (4.39) leads to an expression for $g_i(\bar{s})$

$$g_i(\bar{s}) = -\frac{e_i^r(\bar{s}) \cos\phi(\bar{s}) + e_i^z(\bar{s}) \sin\phi(\bar{s})}{R_0 + \frac{\mathrm{d}\phi}{\mathrm{d}\bar{s}} \left(e_i^r(\bar{s}) \sin\phi(\bar{s}) - e_i^z(\bar{s}) \cos\phi(\bar{s})\right)}. \tag{4.40}$$

4.2.4 Pendant drop tensiometry example

We provide an example to illustrate this method. In this example, a pendant drop of water is formed below a capillary tube of diameter 1.65 mm. A photograph is taken of the drop, with the edge detected from the Canny algorithm (see Section 6.4.1), returning an integer list of coordinates corresponding to the pendant drop profile.

The Levenberg–Marquardt algorithm then iteratively fits the Young–Laplace equation to this data. In our routine, the parameters are initialised by fitting a circle to the bottom 10% of the drop, setting both the centre (X_0, Z_0) and radius R_0 of the drop apex. The Bond number is then initialised from an expression based on the work of Andreas *et al.* [27]. Finally, the rotation ω is initially set to zero.

However, to demonstrate the robustness of the fit, we initialised the routine manually, with poor guesses for the parameters. The routine iteratively fits the theoretical solution to the experimental drop profile, converging in ~ 5 s. The profile corresponding to the initialised parameter set, and the converged profile (after 6 iterations) are illustrated in Fig. 4.3. The command line output is also shown. The `Error` column in the table is the sum of squared residuals (measured

in pixels) divided by the total number of points ($n = 1282$).

```
-------------------------------------------------------------------------
| Step | Error   | x-center | z-center | Apex R_0 |   Bond    | w degree |
|    1 | 363.86 | 260.0000 |  55.0000 | 160.0000 | 0.50000 |  0.00000 |
|    2 | 39.385 | 270.0581 |  61.9450 | 183.9975 | 0.34628 |  0.15421 |
|    3 | 0.1453 | 270.4592 |  60.6798 | 184.7992 | 0.30211 |  0.16676 |
|    4 | 0.1453 | 270.4593 |  60.6797 | 184.7991 | 0.30211 |  0.16680 |
|    5 | 0.1452 | 270.4163 |  60.6752 | 184.7999 | 0.30208 |  0.17844 |
|    6 | 0.1452 | 270.4163 |  60.6752 | 184.7999 | 0.30208 |  0.17844 |
The routine has converged in 6.03 seconds.
Interfacial tension = 71.17 mN / m  (+/- 2%).
```

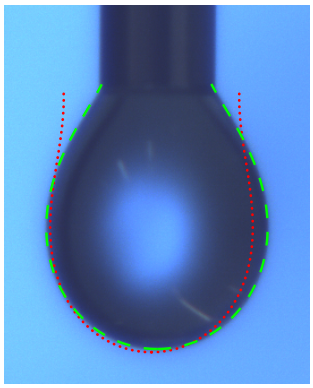

Figure 4.3: The drop photograph is shown, together with the initialised profile (red, dotted curve) and the converged profile after 6 iterations (green, dashed curve).

4.2.5 Limitations

While pendant drop tensiometry provides a simple, elegant method to determine the interfacial tension, the accuracy of this method decreases as the Bond number decreases. Although this reduction in accuracy is well known [35], the physics behind it are rarely discussed.

The accuracy of this method depends on how accurately the Bond number can be determined from experimental data. When the Bond number of a drop is small, the interfacial forces dominate the gravitational forces, with the resulting drop profiles only slightly deformed away from sphericity, as illustrated in Fig. 4.4. In this regime, the sensitivity of the method decreases, since a small change in the drop profile results in a large change in the interfacial tension.

This loss of sensitivity is compounded by errors due to image pixellation (a source of error inherent in any method that extracts data from an image). To demonstrate the effects of pixelation further, a series of synthetic drops were formed for a series of Bond numbers.

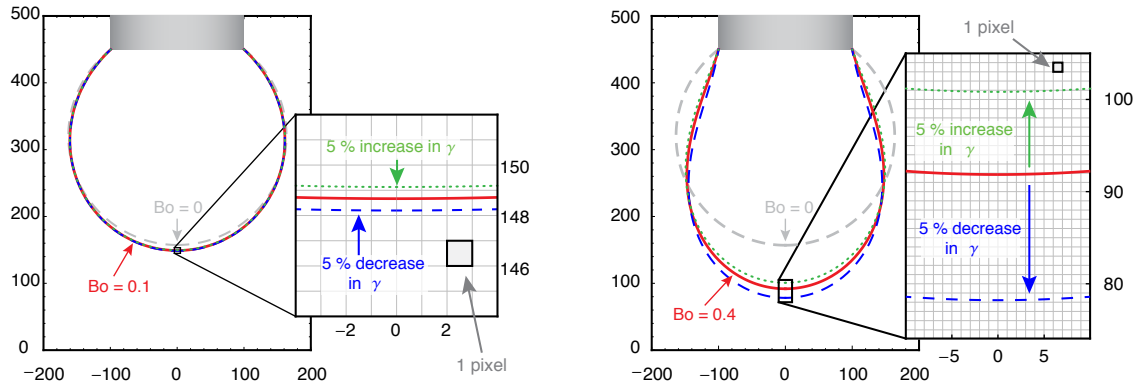

Figure 4.4: A schematic of two drops of the same drop volume, but different Bond numbers. The drop on the left has a Bond number of 0.1, while the drop on the right has a Bond number of 0.4, these interfaces are shown in solid red. In each case the interfacial tension is perturbed by 5%, with a 5% increase in γ shown in dashed blue and a decrease in dotted green. The inset in both images is a zoomed in region near the drop apex, with the grid line spacing equal to the pixel density of the camera used in these experiments. When the Bond number is small, the interfaces are only slightly perturbed, demonstrating the reduced sensitivity in this regime.

A theoretical drop was formed such that its volume was equal to a preset volume, V_{set}, taken to be 20 µL. The drop was then rotated by a random angle, and displaced by a random offset amount. The experimental data was then binarised by rounding each number to form an integer, with the same pixel density as the camera used in these experiments. The resulting pixels form the drop profile that correspond to discrete edge detection with no error.

Once a binarised theoretical drop was formed, the routine developed in this chapter fitted the Young–Laplace equation to the drop, with the interfacial tension calculated from the fitted parameters. This process was performed for 100 synthetic drop profiles, all with the same Bond number. We introduce the relative difference Φ_i between the i^{th} estimate for the interfacial tension, $\hat{\gamma}_i$, with respect to the true value γ, defined

$$\Phi_i \equiv \frac{\hat{\gamma}_i - \gamma}{\gamma} 100\%. \tag{4.41}$$

From the series of values for Φ_i we calculated the associated standard deviation.

This procedure was repeated for a number of different Bond numbers, while keeping the volume of the pendant drop the same, as the initial drop (20 µL). The standard deviation of Φ_i is shown in Fig. 4.5 for varying Bond number, clearly demonstrating the effect pixelation has on the accuracy of the method.

Physically, the pendant drop method measures the interfacial tension by balancing the unknown interfacial forces with the known gravitational forces, which is contained in the Bond number. Using the known expression for the Bond number

then determines the interfacial tension. The small Bond number limitation is a manifestation of the physical limitation arising from the inference of a large unknown quantity from a measured quantity that is much smaller in magnitude.

Sometimes this limitation may be circumvented by making a larger drop, however if the two phases have similar densities this may not be possible. In the next chapter, we provide an important extension to pendant drop tensiometry to accurately access the interfacial tension when the associated Bond number is very small.

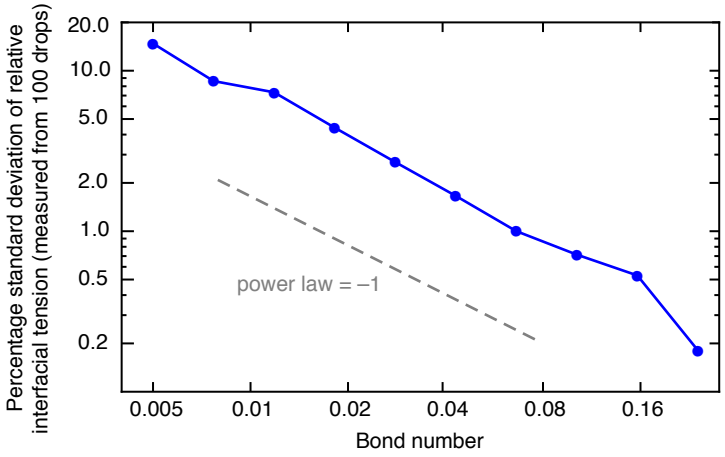

Figure 4.5: The standard deviation for the relative difference in the measured interfacial tension and the true interfacial tension, for different values of the Bond number. As the Bond number decreases, the accuracy of the method decreases due to the pixelation of the drop profile being comparable to the drop deformations away from sphericity. The standard deviation for each Bond number is calculated from a series of 100 synthetic drop, with all synthetic drops having the same drop volume. The dashed line shows a power law of -1.

4.3 Conclusion

In this chapter, we have outlined a variety of methods commonly used in interfacial tensiometry. Each of these methods utilise an important physical force balance to measure the interfacial tension from a measured quantity. One of these methods is the pendant drop tensiometer, where a pendant drop deformed by its own weight is fitted by the Young–Laplace equation. The interfacial tension is then calculated from the fitted parameters. Although the experiment itself is relatively straightforward, fitting the Young–Laplace equation to an experimental photograph is difficult.

The second part of this chapter derives expressions for the residual vector and the Jacobian matrix that, together with the Levenberg–Marquardt algorithm discussed in Chapter 6, allows the Young–Laplace equation to be fitted to an experimental drop photograph. This enables the Bond number to be extracted from an experimental pendant drop photograph, from which the interfacial tension is determined.

When the Bond number of the associated drop is small, gravitational forces are insufficient to deform the drop. This, in turn, leads to a reduction in the accuracy of the calculated Bond number, and thus, a reduction in the accuracy of the interfacial tension. This is a physical limitation due to the disparate size of the two forces, resulting in drop deformations that cannot be accurately determined.

In the next chapter, we introduce a new technique that extends pendant drop tensiometry by adding a small spherical particle to the interface of the drop. This addition facilitates accurate tensiometry for drops with small, and indeed zero, Bond numbers—a regime currently inaccessible to pendant drop tensiometers.

4.4 Bibliography

[1] H.-J. Butt, K. Graf and M. Kappl, *Physics and Chemistry of Interfaces*, John Wiley & Sons, 2003.

[2] J. Drelich, C. Fang and C. White, in *Encyclopedia of Surface and Colloid Science*, Marcel Dekker: New York, 2nd edn., 2002, vol. 3, ch. Measurement of interfacial tension in fluid-fluid systems, pp. 3152–3166.

[3] A. W. Adamson and A. P. Gast, *Physical Chemistry of Surfaces*, John Wiley & Sons, 6th edn., 1997.

[4] J. F. Padday, in *Surface and Colloid Science*, ed. E. Matijević, John Wiley & Sons, 1969, vol. 1.

[5] A. I. Rusanov and V. A. Prokhorov, *Interfacial Tensiometry*, Elsevier, 1996.

[6] L. Wilhelmy, *Annalen der Physik und Chemie*, 1863, **195**, 177–217.

[7] P. G. de Gennes, F. Brochard-Wyatt and D. Quere, *Capillarity and Wetting Phenomena - Drops, Bubbles, Pearls, Waves*, Springer, New York, 2004.

[8] P. L. du Noüy, *J. Gen. Physiol.*, 1919, **1**, 521–524.

[9] P. L. du Noüy, *J. Gen. Physiol.*, 1925, **7**, 625–631.

[10] W. D. Harkins and H. F. Jordan, *J. Am. Chem. Soc.*, 1930, **52**, 1751–1772.

[11] B. Freud and H. Freud, *J. Am. Chem. Soc.*, 1930, **52**, 1772–1782.

[12] C. Huh and S. Mason, *Colloid Polym. Sci.*, 1975, **253**, 566–580.

[13] S. Sugden, *J. Chem. Soc.*, 1922, **121**, 858–866.

[14] F. Bashforth and J. C. Adams, *An attempt to test the theories of capillary action: by comparing the theoretical and measured forms of drops of fluid*, University Press, 1883.

[15] R. Miller, V. B. Fainerman and V. I. Kovalchuk, in *Encyclopedia of Surface and Colloid Science*, ed. A. Hubbard, New York: Dekker, 2002, ch. Bubble and drop pressure tensiometry, pp. 814–828.

[16] Lord Rayleigh (J. W. Strutt), *Proc. R. Soc. Lond.*, 1916, **92**, 184–195.

[17] S. Sugden, *J. Chem. Soc.*, 1921, **119**, 1483–1492.

[18] B. Vonnegut, *Rev. Sci. Instrum.*, 1942, **13**, 6–9.

[19] H. M. Princen, I. Y. Z. Zia and S. G. Mason, *J. Colloid Interface Sci.*, 1967, **23**, 99–107.

[20] A. M. Worthington, *Proc. R. Soc. Lond.*, 1881, **32**, 362–377.

[21] A. M. Worthington, *Philos. Mag.*, 1885, **19**, 46–48.

[22] Y. Rotenberg, L. Boruvka and A. W. Neumann, *J. Colloid Interface Sci.*, 1983, **93**, 169–183.

[23] C. Huh and R. L. Reed, *J. Colloid Interface Sci.*, 1983, **91**, 472–484.

[24] J. W. Jennings and N. R. Pallas, *Langmuir*, 1988, **4**, 959–967.

[25] O. I. del Río and A. W. Neumann, *J. Colloid Interface Sci.*, 1997, **196**, 136–147.

[26] A. Ferguson, *Philos. Mag.*, 1911, **23**, 417–430.

[27] J. M. Andreas, E. A. Hauser and W. B. Tucker, *J. Phys. Chem.*, 1938, **42**, 1001–1019.

[28] S. Fordham, *Proc. R. Soc. Lond. A*, 1948, **194**, 1–16.

[29] D. Niederhauser and F. Bartell, *Annual report of progress–fundamental research on occurrence and recovery of petroleum 1948–1949*, American Petroleum Institute, Baltimore, 1949–1950, pp. 114—146.

[30] K. Levenberg, *Q. Appl. Math.*, 1944, **2**, 164–168.

[31] D. W. Marquardt, *J. Soc. Ind. Appl. Math.*, 1963, **11**, 431–441.

[32] D. D. Morrison, *Methods for nonlinear least squares problems and convergence proofs*, Space Technology Labs., Inc., Los Angeles, CA, United States technical report, 1960.

[33] R. Fletcher, *A modified Marquardt subroutine for non-linear squares*, Atomic Energy Research Establishment, Harwell (England) technical report, 1971.

[34] J. Canny, *IEEE T. Pattern Anal.*, 1986, 679–698.

[35] M. Hoorfar and A. W. Neumann, *Adv. Colloid Interface Sci.*, 2006, **121**, 25–49.

CHAPTER 5

Compound pendant drop tensiometry

A widely used method to determine the interfacial tension between fluids is to quantify the pendant drop shape that is determined by gravity and interfacial tension forces. Failure of this method for small drops or small fluid density differences is a critical limitation in microfluidic applications and when only small fluid samples are available. By adding a small spherical particle to the interface to apply an axisymmetric deformation, both the particle density and the interfacial tension can be simultaneously and precisely determined, providing an accurate and elegant solution to a long-standing problem.

Reproduced with permission from Michael J. Neeson, Derek Y. C. Chan and Rico F. Tabor, *Compound pendant drop tensiometry for surface tension measurement at zero Bond number*, Langmuir, 2014, **30**, 15388–15391.

5.1 Introduction

Capillary phenomena have captured the imagination of great minds for centuries, including those of da Vinci, Young, Newton, Laplace and Maxwell among many others [1]. Capillarity also lies at the foundation of modern nanotechnology because it involves interactions that were described by Maxwell as being "sensible only at insensible distances" [1]. Tensiometry, the measurement of the interfacial tension between fluid phases, directly probes the competition between intermolecular forces that give rise to interfacial tension, and long-range gravitational or applied forces that deform the fluid interface. By measuring the gravitational deformation of a pendant drop [2, 3, 4] and matching that to a solution of the Young-Laplace equation, the interfacial tension can thus be determined. This is one of the most widely used operating principles of current interfacial tension measuring devices.

Bashforth and Adams [5], equally well-known for developing the robust algorithm for integrating ordinary differential equations, showed that the shape of a pendant drop depends only on a single dimensionless quantity, the Bond number $\mathrm{Bo} \equiv \rho g R^2/\gamma$, that characterises the ratio of gravitational to interfacial forces in terms of the density ρ, acceleration due to gravity g, drop size R and interfacial tension γ. With advances in numerical computation and image processing, pendant drop tensiometry appears to be a mature technology [6, 7, 8, 9].

However, there are two regimes in which standard pendant drop tensiometry fails. For situations in which the interfacial tension force is too low to sustain a stable hanging drop, corresponding to Bond number $\mathrm{Bo} \gg 1$, the spinning drop method [10] that exploits fluid inertia to deform the drop can be used.

In the opposite regime, $\mathrm{Bo} \to 0$, surface tension dominates and the drop does not deform. To address this problem, a complex experimental apparatus has been developed in which a droplet is formed between two surfaces that are then separated, allowing gravity to act over a larger length scale, providing a quantifiable deformation to the interface [11, 12, 13]. A complimentary approach to address this problem is the development of more complex optimisation algorithms for image analysis [14]. Although these advances provide some improvements, they cannot circumvent the inherent fundamental physical limitations of the method as $\mathrm{Bo} \to 0$.

5.2 Theory and experiment

In this chapter, we adopt a different strategy by implementing a compound pendant drop technique, achieved simply by adding a spherical particle of known size to the pendant drop. The pendant drop becomes deformed axisymmetrically by the weight and natural positioning of the particle. A significant advantage of this approach is

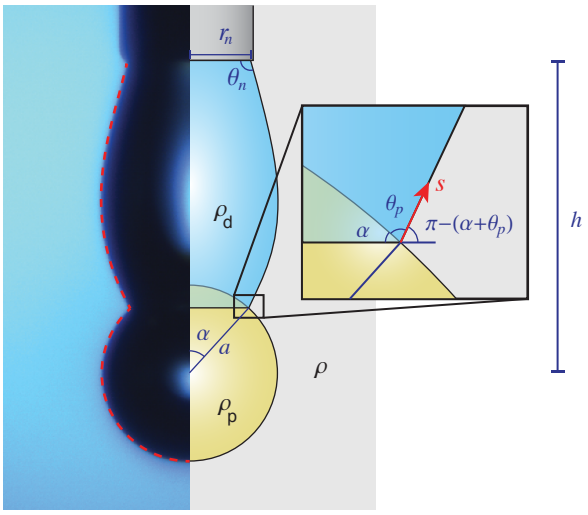

Figure 5.1: Gravitational forces on both the particle and the liquid drop result in coupled drop deformations of a compound pendant drop. Right side: A schematic representation of a spherical particle attached to the interface of an axisymmetric pendant drop emerging from a needle into a bulk fluid phase. Left side: An image of a compound pendant drop from Fig. 5.2 a (v) with the drop shape (red dashed line) found by solving the Young-Laplace equation to determine the drop and particle Bond numbers.

that it does not require new instrumentation, and with the theoretical framework presented here, allows accurate simultaneous determination of the interfacial tension and the particle density. We further demonstrate that the interfacial tension between two fluids that are density matched can be accurately determined, even though the Bond number is zero. The method can also be used to determine the surface tension of pure liquids for which the Bond number is negative.

Consider a pendant drop of density ρ_d emerging from a blunt needle that is used to dispense the drop of varying volume into a bulk external fluid of density ρ. A particle of radius a and density ρ_p is attached to the drop, with gravity naturally positioning it at the bottom of the axisymmetric drop [15], as illustrated in Fig. 5.1.

This system is characterised by a drop Bond number, $\mathrm{Bo_d}$, and a particle Bond number, $\mathrm{Bo_p}$, defined by

$$\mathrm{Bo_d} \equiv (\rho_\mathrm{d} - \rho)\, g a^2/\gamma, \qquad \mathrm{Bo_p} \equiv (\rho_\mathrm{p} - \rho)\, g a^2/\gamma. \tag{5.1}$$

Here, Bond numbers may be positive or negative according to the sign of the density difference.

The pendant drop shape is described by the axisymmetric Young–Laplace equation, that can be written as a system of first order differential equations for the cylindrical coordinates r and z of the drop interface, together with the tangent angle ϕ, in terms of the arc length s, measured from the three phase contact at the particle [5, 15]. These quantities are defined in Fig. 5.1.

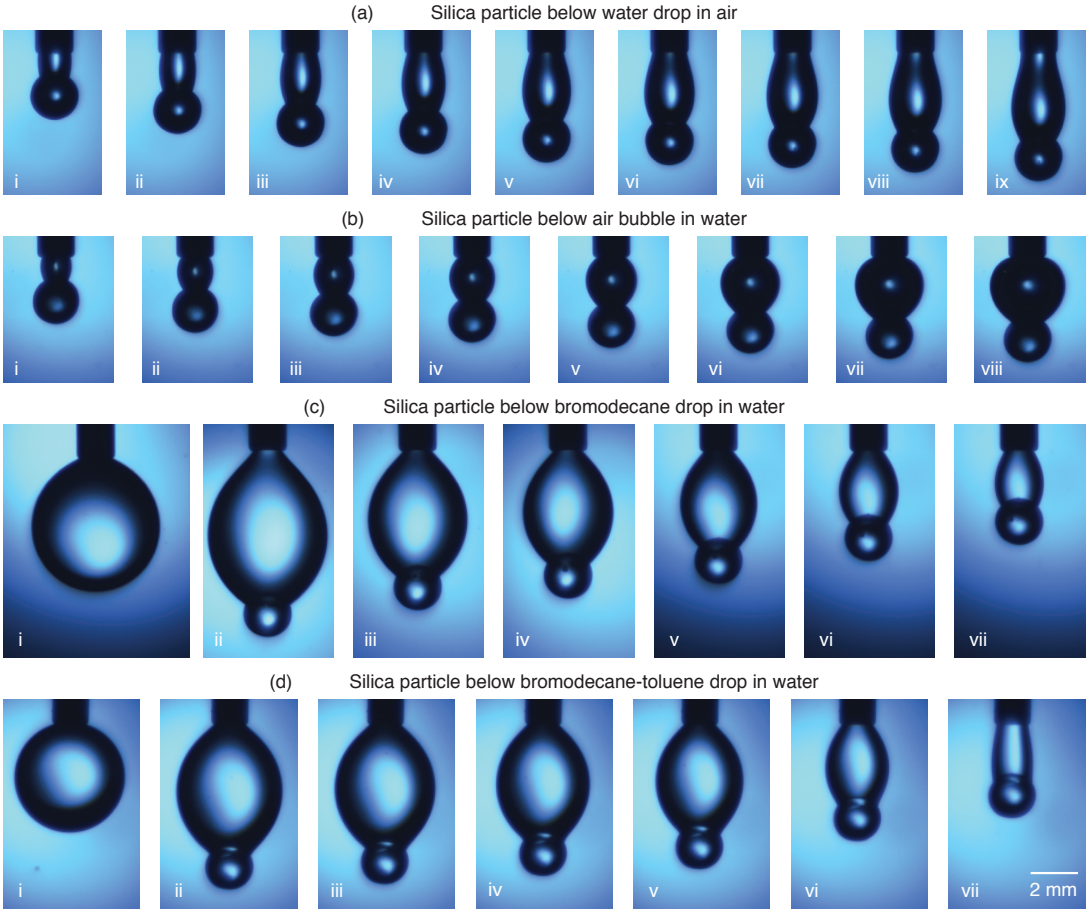

Figure 5.2: (a) A silica particle attached to a pendant water drop in air: (i)-(ix) Gravitational force on the drop and particle elongates the drop as the drop volume increases. (b) A silica particle attached to a pendant air bubble in water: (i)-(viii) Variation of the bubble shape as the volume is increased by injecting air via the needle. The drop Bond number $\mathrm{Bo_d} \sim -1$, so the buoyancy forces on the bubble and the particle act in opposite directions. (c) Bromodecane pendant drop in water with drop Bond number $\mathrm{Bo_d} \sim 0.005$: (i) a near spherical drop shape prior to particle attachment, (ii)-(vii) drop shape after attachment of a silica particle at decreasing drop volume. (d) Density matched bromodecane-toluene pendant drop in water with zero drop Bond number $\mathrm{Bo_d} = 0$: (i) a spherical drop prior to particle attachment, (ii)-(vii) drop shape after attachment of a silica particle at decreasing drop volume. The scale bar shown applies to all images.

With length variables scaled by the particle radius a (as indicated by the overbar), the Young-Laplace equation can be written as a set of coupled ordinary differential equations:

$$\frac{\mathrm{d}\phi}{\mathrm{d}\bar{s}} = 2\bar{H}_0 - \mathrm{Bo_d}\ \bar{z} - \frac{\sin\phi}{\bar{r}} \tag{5.2a}$$

$$\frac{\mathrm{d}\bar{r}}{\mathrm{d}\bar{s}} = \cos\phi \tag{5.2b}$$

$$\frac{\mathrm{d}\bar{z}}{\mathrm{d}\bar{s}} = \sin\phi \tag{5.2c}$$

where $\bar{H}_0 \equiv a\Delta P_0/2\gamma$ is the scaled mean curvature at the point of contact with the particle at $\bar{s} = 0$. ΔP_0 is the pressure difference between the outside and inside of the drop and may be regarded as the Lagrange multiplier that is determined by the volume of the drop.

The boundary conditions at contact with the particle, p, at $\bar{s} = 0$ and with the needle, n, at $\bar{s} = \bar{s}_\mathrm{n}$ are:

$$\mathrm{p}: \bar{s} = 0,\ \bar{r} = \sin\alpha,\ \bar{z} = \cos\alpha,\ \phi = \pi - (\alpha + \theta_\mathrm{p}) \tag{5.3a}$$

$$\mathrm{n}: \bar{s} = \bar{s}_\mathrm{n}\ \bar{r} = \bar{r}_\mathrm{n},\ \bar{z} = \bar{h},\ \phi = \theta_\mathrm{n}. \tag{5.3b}$$

The equilibrium position of the particle is determined by the balance of three forces: (i) the interfacial tension acting around the three phase contact line at the particle, (ii) the pressure difference on different parts of the particle within the drop phase and the bulk fluid phase, and (iii) the gravitational force on the particle. Equating these three contributions gives the the final equation that completes the specification of the problem

$$\sin\alpha\sin(\alpha + \theta_\mathrm{p}) - \bar{H}_0\sin^2\alpha + \mathrm{Bo_d}\,\nu(\alpha) - \mathrm{Bo_p}\,\nu(\pi) = 0 \tag{5.4}$$

where $2\pi a^3\nu(\alpha) \equiv \pi a^3(2 - 3\cos\alpha + \cos^3\alpha)/3$ is the volume of a spherical cap subtending an angle α (see Fig. 5.1).

The pendant drop profile is characterised by the drop Bond number, $\mathrm{Bo_d}$, and the particle Bond number, $\mathrm{Bo_p}$, defined in eqn (5.1). We will focus on results specific to compound pendant drop tensiometry that corresponds to $\mathrm{Bo_p} \sim 1$ and arbitrary values of $\mathrm{Bo_d}$. The limit $\mathrm{Bo_p} \to 0$ corresponds to standard pendant drop tensiometry and will therefore not be considered further.

We now present four experimental cases to illustrate the key features and capabilities of compound pendant drop tensiometry:

Case 1. $\mathrm{Bo_d} \sim 1$, $\mathrm{Bo_p} \sim 1$: The drop is deformed by the combined weight of the particle and the fluid [11, 13]. These two contributions to interfacial deformation

can be decomposed and allows simultaneous measurement of the interfacial tension and the particle weight or the particle density. The experimental system is a silica particle in a water pendant drop in air.

Case 2. $\mathrm{Bo_d} < 0$, $\mathrm{Bo_p} \sim 1$: As the Bond numbers have opposite signs, gravitational forces on the drop and the particle act in opposite directions. If the drop is a "bubble", this is a way to use compound pendant drop tensiometry to measure the surface tension of a bulk liquid-vapour interface. The experimental system is a silica particle in a pendant gas bubble in water.

Case 3. $\mathrm{Bo_d} \ll 1$, $\mathrm{Bo_p} \sim 1$: The drop is mainly deformed by the particle weight, the effect of the drop weight is small. The experimental system is a silica particle in a bromodecane pendant drop in water.

Case 4. $\mathrm{Bo_d} = 0$, $\mathrm{Bo_p} \sim 1$: The interface is only deformed by the weight of the particle. The experimental system is a silica particle in a bromodecane-toluene pendant drop in water. The composition of the miscible bromodecane-toluene mixture is density matched to water to give $\mathrm{Bo_d} = 0$.

5.3 Results and discussion

Photographs of these four experimental systems are shown in Fig. 5.2 for varying drop volumes. For each photograph the theoretical compound pendant drop profile is fitted to the experimental profile (see Fig. 5.1), determining the Bond numbers, $\mathrm{Bo_d}$ and $\mathrm{Bo_p}$, together with the particle radius a. The interfacial tension can be calculated from eqn (5.1), while the ratio of Bond numbers

$$\mathrm{Bo_p}/\mathrm{Bo_d} = (\rho_\mathrm{p} - \rho)/(\rho_\mathrm{d} - \rho), \tag{5.5}$$

determines the particle density, ρ_p. The compound pendant drop profile is extracted from a photo image using a Canny edge detection algorithm [16] after checking that there is no anisotropy in the optical system. Optimal values of the particle radius, a, the filling angle, α, the particle contact angle, θ_p, and the Bond number, $\mathrm{Bo_d}$ and $\mathrm{Bo_p}$, are determined by the Levenberg-Marquardt method [17, 18] (see appendices for details).

In Fig. 5.2a, for **Case 1**: $\mathrm{Bo_d} \sim 1$, $\mathrm{Bo_p} \sim 1$, we show a sequence of pendant water drop shapes in air with an attached silica particle and in Fig. 5.2b, corresponding to **Case 2**: $\mathrm{Bo_d} < 0$, $\mathrm{Bo_p} \sim 1$, we show a sequence of pendant bubble shapes in water with an attached silica particle. The particle density found by analysing the variations of drop shape with drop volume is shown in Fig. 5.3. Also shown for comparison is the mean density calculated by weighing the particles independently with a microbalance. The accuracy of the results for the particle density improves with

increasing drop volume because larger and more complex drop shapes provide more varied data points to facilitate accurate image analysis. The agreement between the three methods of determining the particle density is very good.

The air/water surface tension, $\gamma_{A/W}$, determined by this method is shown in Fig. 5.4 and compares favourably with the literature value of 72 mN/m.

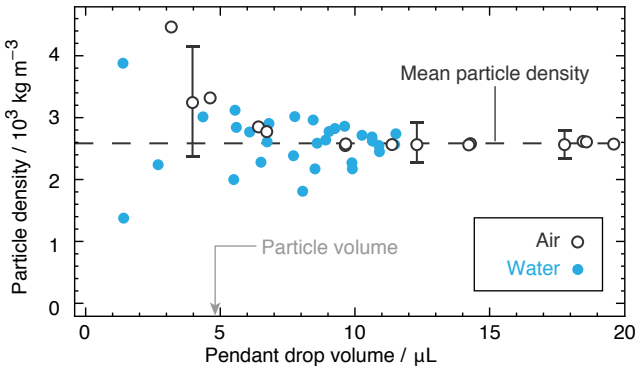

Figure 5.3: Density of the silica particle deduced from the compound pendant water drop in air (filled blue circles) and the compound pendant bubble in water (open white circles) experiments. The mean density calculated by independently weighing the particles with a microbalance is shown as the dashed line. Representative experimental uncertainties are included.

In Fig. 5.2c, for **Case 3**: $Bo_d \ll 1$, $Bo_p \sim 1$, we show a sequence of pendant bromodecane drop shapes in water with an attached silica particle and in Fig. 5.2d, corresponding to **Case 4**: $Bo_d = 0$, $Bo_p \sim 1$, we show a sequence of pendant bromodecane-toluene drop shapes in water with an attached silica particle. The composition of the bromodecane-toluene mixture is adjusted to match the density of water thereby giving a zero drop Bond number, $Bo_d = 0$. From photos (i) of Fig. 5.2c where $Bo_d \sim 0.005$ and of Fig. 5.2d where $Bo_d = 0$, we see that the drop shape is spherical so no information can be deduced about the interfacial tension. The drop shapes at different drop volumes with the silica particle attached is shown in photos (ii)-(vii) in each case.

From such images, variations of the extracted bromodecane/water, $\gamma_{BD/W}$ and bromodecane-toluene/water interfacial tensions with drop volume are shown in Fig. 5.4. The results for bromodecane/water interfacial tension agree very well with the literature value of 44 mN/m for almost all drop volumes [19]. The expected interfacial tension for the bromodecane-toluene system is calculated from the pure components as 40.6 mN/m, as described in the Supporting Information.

5.4 Conclusion

In conventional pendant drop tensiometry, the zero Bond number limit is a physical constraint that cannot be overcome by improving the measurement precision. The

attachment of a particle to a pendant drop to create a compound pendant drop tensiometer, that, together with appropriate theoretical modelling provides a simple and accurate route to measure key physical and thermodynamic parameters at low and zero Bond numbers. From a single drop profile acquisition, the interfacial tension, liquid/solid contact angle and particle density can be obtained. As well as circumventing the limits of conventional pendant drop tensiometry, this present approach can possibly be improved with more sophisticated image analysis. In any case, the compound pendant drop method facilitates access to surface and interfacial tensions with much smaller liquid sample sizes, which is of particular interest when dealing with valuable or scarce biological samples. It additionally provides new opportunities for the study of interfacial dynamics by offering simultaneous acquisition of interfacial tension and contact angle, pertinent to inkjet and 3D printing as well as formulation of smart coatings.

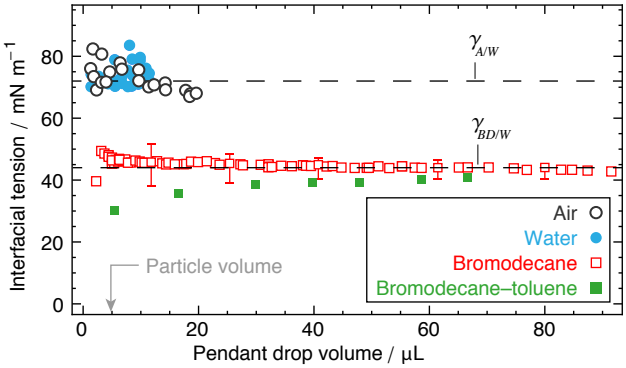

Figure 5.4: Interfacial tension for each of the four particle-drop systems deduced by compound pendant drop tensiometry shown in Fig. 5.2: the air-water interfacial tension calculated from a water drop in air (filled blue circles) and from an air bubble in water (open white circles); a bromodecane drop in water (open red squares) and a bromodecane-toluene drop density matched to water (solid green squares) demonstrates the applicability of the method even at zero Bond number.

Acknowledgements

This work was supported in part by the Australian Research Council through a Discovery Project Grant (DP 140100677) and by the Particulate Fluids Processing Centre at the University of Melbourne.

Supporting Information

See the appendices for a derivation of the theory (Section 5.A), experimental and optimisation details (Sections 5.B and 5.C), a comparison between the sensitivity for the method presented compared with existing pendant drop tensiometry (Section 5.D), and an analogy with classical Hookean springs (Section 5.E).

5.5 Bibliography

[1] J. C. Maxwell, *Capillary action*, Encyclopædia Britannica, 9th edn., 1876, vol. V, pp. 56–71.

[2] A. M. Worthington, *Proc. R. Soc. Lond.*, 1881, **32**, 362–377.

[3] A. M. Worthington, *Philos. Mag.*, 1885, **19**, 46–48.

[4] A. Ferguson, *Philos. Mag.*, 1911, **23**, 417–430.

[5] F. Bashforth and J. C. Adams, *An attempt to test the theories of capillary action: by comparing the theoretical and measured forms of drops of fluid*, University Press, 1883.

[6] Y. Rotenberg, L. Boruvka and A. W. Neumann, *J. Colloid Interface Sci.*, 1983, **93**, 169–183.

[7] C. Huh and R. L. Reed, *J. Colloid Interface Sci.*, 1983, **91**, 472–484.

[8] J. W. Jennings and N. R. Pallas, *Langmuir*, 1988, **4**, 959–967.

[9] O. I. del Río and A. W. Neumann, *J. Colloid Interface Sci.*, 1997, **196**, 136–147.

[10] B. Vonnegut, *Rev. Sci. Instrum.*, 1942, **13**, 6–9.

[11] C. Ferrera, J. Montanero and M. Cabezas, *Meas. Sci. Technol.*, 2007, **18**, 3713—3723.

[12] E. Vega, J. Montanero, M. Herrada and C. Ferrera, *Phys. Rev. E*, 2014, **90**, 013015.

[13] A. Kalantarian, R. David, J. Chen and A. W. Neumann, *Langmuir*, 2011, **27**, 3485–3495.

[14] N. J. Alvarez, L. M. Walker and S. L. Anna, *J. Colloid Interface Sci.*, 2009, **333**, 557–562.

[15] M. J. Neeson, R. R. Dagastine, D. Y. C. Chan and R. F. Tabor, *Soft Matter*, 2014, **10**, 8489–8499.

[16] J. Canny, *IEEE T. Pattern Anal.*, 1986, 679–698.

[17] K. Levenberg, *Q. Appl. Math.*, 1944, **2**, 164–168.

[18] D. W. Marquardt, *J. Soc. Ind. Appl. Math.*, 1963, **11**, 431–441.

[19] M. J. Neeson, R. F. Tabor, F. Grieser, R. R. Dagastine and D. Y. C. Chan, *Soft Matter*, 2012, **8**, 11042–11050.

[20] J. Saien and S. Akbari, *J. Chem. Eng. Data*, 2006, **51**, 1832–1835.

5.A Compound pendant drop theory

Here we provide a detailed derivation of the theory presented in the main text for the shape of a pendant drop with density ρ_d suspended from a surface (in this case a needle), with a particle of density ρ_p hanging axisymmetrically at its apex. The compound pendant drop system is surrounded by a bulk fluid phase with density ρ. A schematic of this configuration is shown in Fig. 5.5.

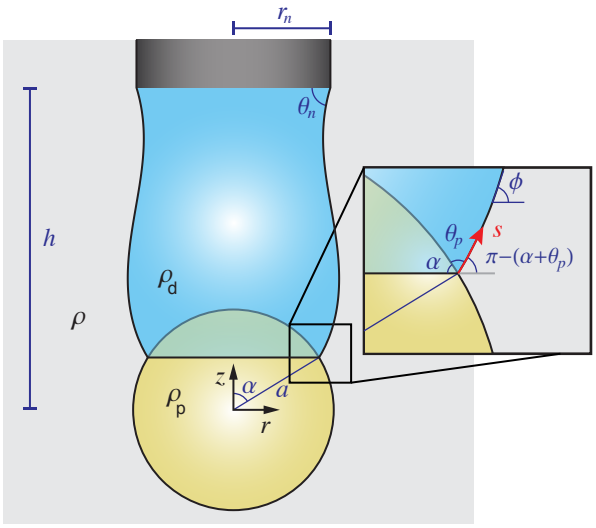

Figure 5.5: A schematic representation of a particle attached to the interface of a pendant drop below a needle. Gravitational forces act on both the particle and the liquid drop, resulting in coupled drop deformations.

We now show that the shape of this system is characterised by a drop Bond number, $\mathrm{Bo_d}$, and a particle Bond number, $\mathrm{Bo_p}$, defined by

$$\mathrm{Bo_d} \equiv (\rho_\mathrm{d} - \rho)\, g a^2/\gamma, \qquad \mathrm{Bo_p} \equiv (\rho_\mathrm{p} - \rho)\, g a^2/\gamma. \tag{5.6}$$

The shape of the fluid interface is described by the axisymmetric Young–Laplace equation, which can be written as a system of first order differential equations for the coordinates r and z of the drop interface, together with the azimuthal angle ϕ, in terms of the arc length s, measured from the three phase contact at the particle. The dimensional Young–Laplace equations are

$$\frac{\mathrm{d}\phi}{\mathrm{d}s} = 2H_0 - (\rho_\mathrm{d} - \rho)gz - \frac{\sin\phi}{r} \tag{5.7a}$$

$$\frac{\mathrm{d}r}{\mathrm{d}s} = \cos\phi \tag{5.7b}$$

$$\frac{\mathrm{d}z}{\mathrm{d}s} = \sin\phi. \tag{5.7c}$$

In the preceding expression, H_0 is the mean curvature at the particle contact. Scaling

by the particle radius a leads to the ordinary differential equations:

$$\frac{\mathrm{d}\phi}{\mathrm{d}\bar{s}} = 2\bar{H}_0 - \mathrm{Bo_d}\ \bar{z} - \frac{\sin\phi}{\bar{r}} \tag{5.8a}$$

$$\frac{\mathrm{d}\bar{r}}{\mathrm{d}\bar{s}} = \cos\phi \tag{5.8b}$$

$$\frac{\mathrm{d}\bar{z}}{\mathrm{d}\bar{s}} = \sin\phi \tag{5.8c}$$

where the Bond number associated with the drop $\mathrm{Bo_d}$ naturally arises, together with the scaled mean curvature $\bar{H}_0 \equiv a\Delta P_0/2\gamma$. The associated boundary conditions at the particle p and needle n contacts are:

$$\mathrm{p} : \bar{s} = 0,\ \bar{r} = \sin\alpha,\ \bar{z} = \cos\alpha,\ \phi = \pi - (\alpha + \theta_\mathrm{p}) \tag{5.9a}$$

$$\mathrm{n} : \bar{s} = \bar{s}_\mathrm{n}\ \bar{r} = \bar{r}_\mathrm{n},\ \bar{z} = \bar{h},\ \phi = \theta_\mathrm{n}. \tag{5.9b}$$

Since the particle is stationary, the net force acting on it must be zero. The net force is the sum of three forces:

(i) the interfacial tension $F_\mathrm{interfacial}$, acting upwards around the perimeter of the three phase contact,

(ii) the pressure inside the drop F_pressure acting downwards on the drop/particle contact area, and

(iii) the weight of the particle F_weight acting downwards.

We now calculate each of these components separately, adopting the notation where a force with a positive sign acts in the positive z-direction.

The force arising from the interfacial tension will act around the perimeter of the three phase contact. By symmetry, the resulting force will act only in the z-direction. Taking the vertical component of the interfacial tension and rotating around the perimeter of the three phase contact line gives

$$F_\mathrm{interfacial} = (2\pi a \sin\alpha)(\gamma \sin(\alpha + \theta_\mathrm{p})). \tag{5.10}$$

The force due to pressure is a double integral over the particle-drop contact area (denoted 'area'),

$$\begin{aligned}\mathbf{F}_\mathrm{pressure} &= -\iint_\mathrm{area} \Delta P\, \mathrm{d}\mathbf{S} \\ &= -\iint_\mathrm{area} \Delta P_0 - (\rho_\mathrm{d} - \rho)\, g\, z\ \mathrm{d}\mathbf{S}.\end{aligned}$$

Although the above expression is a vector quantity, axial symmetry results in a force acting in the z-direction. Changing to spherical coordinates, the signed pressure

force is

$$F_{\text{pressure}} = -\int_0^{2\pi}\int_0^{\alpha} \{\Delta P_0 - (\rho_{\text{d}} - \rho)g(a\cos\varphi - a\cos\alpha)\} \\ a^2 \sin\varphi\cos\varphi \, \mathrm{d}\varphi \, \mathrm{d}\theta \\ = -\pi(a\sin\alpha)^2\Delta P_0 + (\rho_{\text{d}} - \rho)\, g\, v_{\text{cap}}(a,\alpha). \tag{5.11}$$

The first term above is the Laplace pressure at the particle contact acting on the circular cross section of the particle while the second term represents the force due to the weight of displaced fluid, where $v_{\text{cap}}(a,\alpha)$ is the volume of the displaced fluid, where

$$v_{\text{cap}}(a,\alpha) \equiv \frac{\pi a^3}{3}\left(2 - 3\cos\alpha + \cos^3\alpha\right) \\ \equiv 2\pi a^3 \nu(\varphi). \tag{5.12}$$

Finally, the weight of the particle is

$$F_{\text{weight}} = -(\rho_{\text{p}} - \rho)\, V_{\text{p}}\, g = -(\rho_{\text{p}} - \rho)\, g\, v_{\text{cap}}(a,\pi). \tag{5.13}$$

Taking the net force on the particle to be zero gives

$$\bar{F}_{\text{net}} = \sin\alpha\sin(\alpha + \theta_{\text{p}}) - \bar{H}_0\sin^2\alpha + \text{Bo}_{\text{d}}\,\nu(\alpha) - \text{Bo}_{\text{p}}\,\nu(\pi) = 0 \tag{5.14}$$

where we have also introduced the force scale $2\pi a\gamma$, together with the scaled spherical cap volume defined in eqn (5.12).

5.B Fitting experimental and theoretical profiles

In this section we detail the routine developed to fit the theoretical curve to the experimental photograph, thus allowing the Bond numbers, and ultimately the particle density and interfacial tension, to be determined. The routine implemented can be separated into two subroutines: firstly, the compound drop profile is extracted from an experimental photograph via image analysis, and secondly, the theoretical curve is fitted to the extracted experimental drop profile. This is illustrated in Fig. 5.6.

We now detail each of the subroutines.

5.B.1 Image analysis

For a given experimental photograph, noise is initially reduced using a Gaussian filter. The compound pendant drop profile is then extracted using a Canny edge

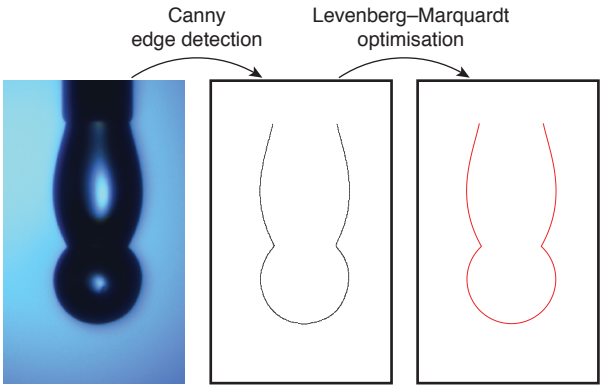

Figure 5.6: An example of an experimental photograph that has been fitted with the theoretical solution presented. The compound drop profile is extracted using the Canny edge detection algorithm. This profile is then fitted with the theoretical solution by minimising the sum of least squares, using the Levenberg–Marquardt algorithm. The three profiles correspond to the experiment Fig. 2 a (v) from the main text.

detection algorithm [16], returning a list of integer (r, z) coordinates corresponding to pixels of the compound pendant drop profile.

Next the theoretical curve is fitted to this data.

5.B.2 Levenberg–Marquardt algorithm

From the presented theory, a compound pendant drop profile depends on five parameters; the particle radius a and filling angle α, the particle contact angle θ_p, and finally two Bond numbers, $\mathrm{Bo_d}$ and $\mathrm{Bo_p}$. From this set of parameters, all other quantities associated with the interface can be determined from eqn (5.8), (5.9) and (5.14).

For a given experimental photograph, there are three additional parameters; two associated with the position of the axes, (R_0, Z_0), and finally, a possible small rotation ω associated with a small camera rotation.

The theoretical curve was fitted to the experimental drop profile using a numerical optimisation algorithm (Levenberg–Marquardt) similar to those used in current pendant drop tensiometers. We minimise the sum of the distance squared between each data point and the theoretical function, which is a function of the unknown parameters $\boldsymbol{\beta} = \{a, \alpha, \theta_\mathrm{p}, \mathrm{Bo_d}, \mathrm{Bo_p}, R_0, Z_0, \omega\}$.

Given a parameter set $\boldsymbol{\beta}$, a theoretical profile can be generated. For each data point (r_i, z_i), the squared residual (the minimal squared distance between the given point and the theoretical curve) can be calculated as follows: the data point is rotated according to the new axes origin (R_0, Z_0), and axes rotation ω. If the rotated data point is above the particle contact line, $\{(r_i - R_0)\sin\omega + (z_i - Z_0)\cos\omega\} > a\cos\alpha$, the residual is calculated by finding the minimum distance between the rotated point and the theoretical curve for the drop interface. Thus, the residual e_i

can be calculated as

$$e_i^2 = \min_s F_i(s), \tag{5.15}$$

where $F_i(s)$ is the squared distance between the data point (r_i, z_i) and the theoretical point $(r(s), z(s))$ at arc length s (see Fig. 5.7)

$$F_i(s) = e_i^r(s)^2 + e_i^z(s)^2 \tag{5.16}$$

where

$$e_i^r(s) = |(r_i - R_0)\cos\omega - (z_i - Z_0)\sin\omega| - r(s) \tag{5.17}$$

$$e_i^z(s) = ((r_i - R_0)\sin\omega + (z_i - Z_0)\cos\omega) - z(s) \tag{5.18}$$

are the horizontal and vertical distances between the (rotated) experimental data points and the theoretical curve, respectively. In the preceding expression $r = a\,\bar{r}$ and $z = a\,\bar{z}$.

If the rotated data point is below the particle contact line,

$$\{(r_i - R_0)\sin\omega + (z_i - Z_0)\cos\omega\} \leq a\cos\alpha,$$

the residual is calculated by comparing the point to the particle, which gives

$$e_i = \left|\sqrt{(r_i - R_0)^2 + (z_i - Z_0)^2} - a\right|. \tag{5.19}$$

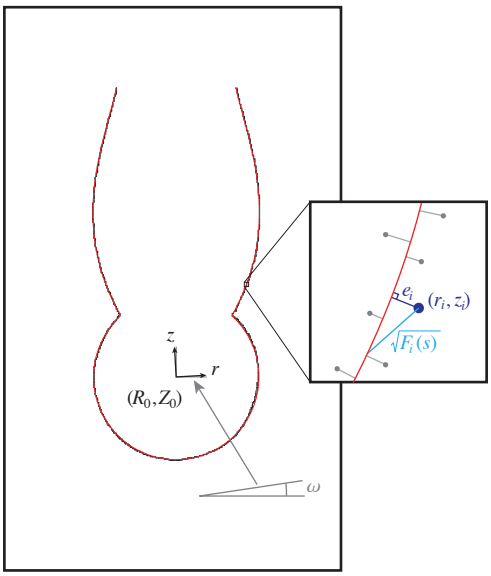

Figure 5.7: The residual e_i for a given data point (r_i, z_i) from the drop interface, found by minimising the squared distance (the function $F_i(s)$) between the data point and the interface. The axes origin with respect to the experimental photograph (R_0, Z_0), together with the angular offset ω are also shown.

The residual e_i is calculated for each experimental data point, thus giving the objective function that we minimise, the sum of squares E, defined

$$E = E(\boldsymbol{\beta}) \equiv \sum_{i=1}^{n} e_i^2. \tag{5.20}$$

For a given experimental photograph, this objective function is explicitly a function of the parameters $\boldsymbol{\beta}$ used in generating a theoretical profile.

A robust and efficient iterative procedure to minimise an m-dimensional nonlinear function (with $m = 8$) is the Levenberg–Marquardt optimisation routine. To implement the method, the residual vector $\boldsymbol{e}$ (with elements e_i) and the Jacobian matrix $\mathbf{J}$ are evaluated for each data point, with the Jacobian defined

$$\mathbf{J}_{ij} = \frac{\partial e_i}{\partial \beta_j}. \tag{5.21}$$

The Jacobian can be calculated numerically by individually perturbing each parameter and calculating a numerical derivative, *i.e.* for $h \ll 1$

$$\frac{\partial e_i}{\partial \beta_j} = \frac{e_i(\beta_1, \ldots, \beta_j + h, \ldots, \beta_m) - e_i(\boldsymbol{\beta})}{h}. \tag{5.22}$$

The Levenberg–Marquardt optimisation routine iteratively updates the parameter vector $\boldsymbol{\beta}^{(k)}$ according to

$$\boldsymbol{\beta}^{(k+1)} = \boldsymbol{\beta}^{(k)} + \boldsymbol{\delta} \tag{5.23}$$

where $\boldsymbol{\delta}$ is calculated by solving

$$\left(\mathbf{J}^{\mathrm{T}}\mathbf{J} + \lambda \operatorname{diag}(\mathbf{J}^{\mathrm{T}}\mathbf{J})\right) \boldsymbol{\delta} = -\mathbf{J}^{\mathrm{T}}\boldsymbol{e}, \tag{5.24}$$

where $\operatorname{diag}(\mathbf{J}^{\mathrm{T}}\mathbf{J})$ is the diagonal matrix with diagonal elements taken from $\mathbf{J}^{\mathrm{T}}\mathbf{J}$, while λ is a parameter which varies at each of the iteration. If the objective function E reduces, the parameter λ is reduced (typically $\lambda = \lambda/10$). Conversely, if the objective function increases in magnitude, the parameter is increased (typically $\lambda = 10\lambda$).

This iterative process is repeated until either:

i. the objective has converged, $E < \mathrm{tol}_1$
ii. the parameters have converged, $\|\boldsymbol{\beta}^{(k+1)} - \boldsymbol{\beta}^{(k)}\| < \mathrm{tol}_2$
iii. the number of iterations has exceeded a specified threshold, $n_{\mathrm{steps}} > \mathrm{tol}_3$.

The optimised parameter set includes the two Bond numbers, as well as the particle radius. Provided one of these Bond numbers is not zero, this Bond number

can be used to express the interfacial tension in terms of the physical quantities associated with the system (from eqn (5.6)). If both Bond numbers are non-zero, their ratio can be used to express the particle density ρ_p in terms of the two fluid densities,

$$\rho_p = \rho + (\rho_d - \rho)\mathrm{Bo}_p/\mathrm{Bo}_d. \tag{5.25}$$

Further information is included in Section 6.4.4.

5.C Experimental details

Water was obtained from a Millipore Direct-Q 5 system (minimum resistivity 18.4 MΩ cm). Silica spheres with a radius of ∼1 mm were made hydrophobic by sputtering 5 nm of copper and subsequently soaking in decanethiol. For each experiment a pendant drop was formed below the needle, with the particle attached by bringing the drop into contact with the particle.

Experiments were visualised using a CCD camera (Flea3, Point Grey, Richmond, BC, Canada) coupled to a Kozo XJP-300 microscope. The optical system was calibrated using the known needle diameter. Diffuse illumination was provided using a white LED source and a diffuser. A routine developed in Mathematica (Wolfram Research) was used to extract the profile and fit the theoretical solution.

The interfacial tension for the bromodecane/toluene mixture was calculated from literature values for bromodecane of 44 mN/m [19], and toluene of 37 mN/m [20], assuming ideal mixing. The molar ratio used was 1.00:0.97 (bromodecane:toluene) giving a predicted interfacial tension of 40.6 mN/m.

5.D Sensitivity

Ultimately the sensitivity of a tensiometer which relies on fitting a theoretical curve to an experimental drop profile depends on its ability to distinguish between different drop profiles. To illustrate the sensitivity of the method presented in this chapter compared with existing pendant drop tensiometers, we compared theoretical drop profiles formed with the same physical quantities as those in Experiment 3, for a bromodecane drop surrounded by water (*i.e.* the same fluid densities, interfacial tension, needle diameter, particle size and particle density).

Firstly, a theoretical pendant drop profile was formed, which was then compared to a pendant drop of the same volume but with an interfacial tension that differed by 10%. This process was repeated for the compound pendant drop system (with a silica particle attached). The associated Bond number for the system is $\mathrm{Bo}_d \sim 0.02$. All four interfaces are shown in Fig. 5.8. The unperturbed interfaces are shown

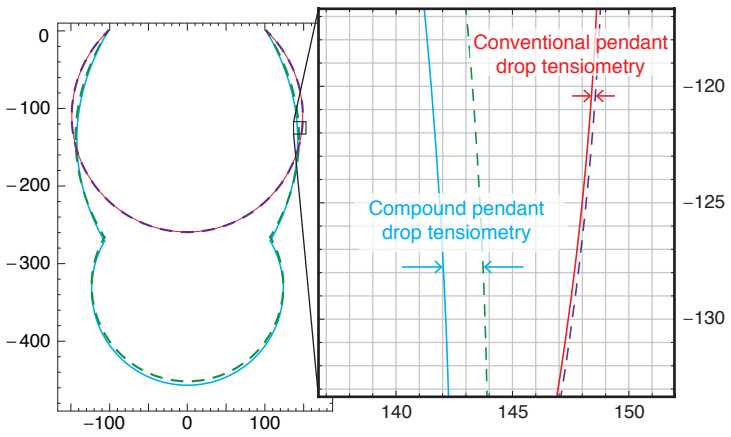

Figure 5.8: A comparison between the sensitivity of the compound pendant drop tensiometry method presented here to conventional pendant drop tensiometry. The image on the left shows a bromodecane drop (red), and a compound silica-bromodecane drop (blue). Both drops have the same volume and all other physical quantities are taken from our experiments. Two more simulated plots illustrate a 10% increase in the interfacial tension (dashed purple for the plain drop, dashed green for the compound pendant drop). The figure on the right illustrates the profile change, with the grid lines showing the pixel density of the camera used in this work.

in blue (compound pendant drop) and red (pendant drop), with the increase in interfacial tension of 10% shown in dashed green and dashed purple, respectively.

5.E Analogy with Hookean springs

We draw an analogy between the system presented and that for a more classical spring scale. A well know method for calculating the mass of an object is to attach it to a spring with a known spring constant k and measure the displacement x. Using Hooke's law for small deformations, the applied force can be calculated and then equated to the gravitational force, *i.e.* $F = -kx = mg$. To calibrate the spring constant, a precisely known mass is attached to the spring. This analogy illustrates the case where the particle Bond number is appreciable, while the drop Bond number is negligible ($\mathrm{Bo_d} \ll 1$, $\mathrm{Bo_p} \sim 1$), where γ takes the role of the spring constant, while the 'displacement' is no longer an easily extracted value, but rather it is related to the deformation profile and can be calculated by fitting the theoretical curve to the experimental data.

The method corresponding to both Bond numbers being appreciable ($\mathrm{Bo_d} \sim 1$, $\mathrm{Bo_p} \sim 1$) is slightly more involved, and can be thought of as a spring with its own mass. Thus, the spring will itself deform due to its own weight. If a mass is added to this new 'heavy' spring, this mass will further deform the spring, however these two deformations will result in fundamentally different deformation profiles. The attached mass deformation will deform the spring constantly throughout, however

the spring weight will deform the top of the spring *more* than the bottom. By using knowledge of the spring mass will then enable the spring constant to be calculated, which in turn can be used to calculate the weight of the added mass. Similarly, if a pendant drop is deformed with both the drop and particle Bond numbers being appreciable, it is possible to calculate both the interfacial tension and the particle density simultaneously.

CHAPTER 6

Theoretical foundations

Throughout this thesis we have considered the shape of immiscible fluid interfaces and the thermodynamic reasons for their existence. In this chapter we provide a concise overview of the physics of fluid interfaces, together with a detailed description of the image analysis and fitting routine used to fit the presented theory to experimental drop photographs.

We introduce the ideal interface between two immiscible fluids. For the case where the phases comprise a liquid and a gas, we consider the intermolecular cohesive forces within the liquid, leading to an energetic interpretation of the surface tension. For the general case of an interface separating two continuous phases, the related interfacial tension is also discussed.

Having energetically introduced the interfacial tension, we consider the free energy associated with a volume of an inner phase immobilised on a surface, surrounded by a continuous immiscible outer phase. By minimising the energy associated with this system, we derive the both the Young–Laplace equation, that determines the shape of the immiscible fluid interface, and the possible boundary conditions associated with the three-phase contact at the surface. Finally, we discuss the three-phase contact condition between three mutually immiscible fluid interfaces.

After discussing the physics of immiscible fluid interfaces, we detail the computational procedures used throughout this thesis. Both the edge detection algorithm used to extract drop profiles from experimental images, and the non-linear fitting algorithm used to fit the theory to the extracted data, are discussed. Fitting the theoretical and experimental drop profiles serves two purposes. First, it demonstrates the applicability of the theory, and second, it allows physical quantities to be determined, providing important insight into the physics of compound drops.

6.1 Surfaces and interfaces

The region that separates two phases is known as an interface. These phases can be comprised of a solid, a liquid or a gas. When one phase is a liquid and the other is a gas, the interface is also known as a surface.

Gibbs proposed an ideal interface between two phases as a region of zero volume [1, 2]. In reality however, this region is not ideal and instead occupies a non-zero volume, as illustrated in Fig. 6.1. While this has been considered [3, 4], our work is based on Gibbs' ideal interface.

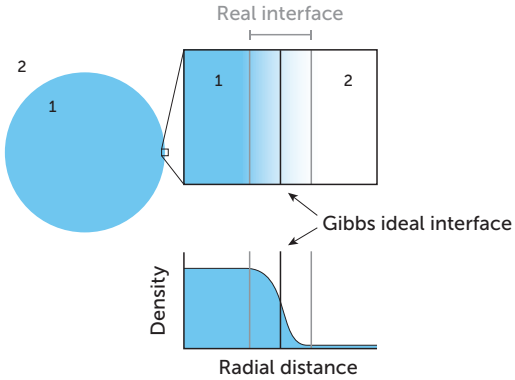

Figure 6.1: Schematic of the interface between two phases. The expanded view illustrates the Gibbs ideal interface which is infinitesimally thin together with the actual interface where the density change is continuous. Adapted from Butt *et al.* [5].

6.2 Surface and interfacial tension

6.2.1 Surface tension

Intermolecular forces arise from a number of physical origins such as covalent bonding, hydrogen bonding and van der Waals forces. For molecules within a condensed phase it is energetically favourable for each of the molecules to be surrounded by other molecules. If this were not the case the condensed phase would not exist to begin with. Thus, the intermolecular forces decrease the total energy of the system.

A schematic representation of a surface between a condensed liquid phase and a vapour phase is shown in Fig. 6.2. A molecule within the bulk has more neighbouring molecules (and thus more intermolecular forces) compared to a molecule at the liquid surface. Since these intermolecular forces decrease the total energy of the system, it is energetically unfavourable for a molecule to exist at the surface. It is this energetic 'penalty' associated with surface molecules that gives rise to the surface tension γ. The surface tension can thus be interpreted as the energy required to bring a molecule from inside the bulk to the liquid surface. The surface energy can

be written as γA, where A is the area of the liquid-vapour surface, and thus, the surface energy acts to minimise the surface area of the liquid phase [5].

As the surface tension is related to the surface energy and area ($\mathrm{d}E = \gamma\,\mathrm{d}A$), its associated units are J m^{-2}, which can equivalently be written N m^{-1}. Throughout this thesis we use units mN m^{-1}.

The strength of the intermolecular forces affects the magnitude of the interfacial tension. For example, since mercury atoms are subject to covalent bonds, the surface tension is relatively large ($\gamma = 485$ mN m^{-1}). Water molecules experience hydrogen bonding, and thus the surface tension is moderate ($\gamma = 72$ mN m^{-1}), while the intermolecular forces within oils are the relatively weak van der Waals force, resulting in lower surface tension values ($\gamma \sim 20$–50 mN m^{-1}).

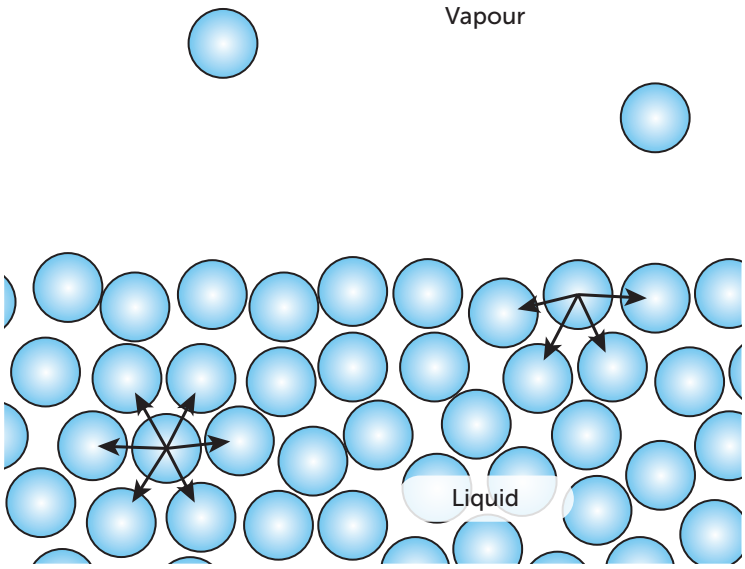

Figure 6.2: Schematic of the intermolecular forces within a condensed liquid phase. Molecules at the surface experience less energetically favourable intermolecular forces, thereby increasing the free energy. The surface tension γ can be interpreted as the energy required to bring a molecule from within the bulk to the surface.

6.2.2 Interfacial tension

For the case when two fluids are separated by an immiscible fluid interface, a somewhat equivalent quantity, the interfacial tension γ, is defined. While the surface tension arises from cohesive forces (forces between like molecules), the interfacial tension involves both cohesive and adhesive forces (forces between dissimilar molecules). However, despite the difference in the physical origins of the two tensions, their associated energetic properties are the same, *viz.* both quantities increase the energy of a system according to $\mathrm{d}E = \gamma\,\mathrm{d}A$.

6.3 The Young–Laplace equation

The Young–Laplace equation relates the Laplace pressure across an interface with the curvature of the interface and the interfacial tension, and can be written

$$\gamma\left(\frac{1}{R_1}+\frac{1}{R_2}\right)=\Delta P\equiv\Delta P_0-\Delta\rho g z \tag{6.1}$$

where R_1 and R_2 are the principal radii of curvature, while $\Delta P\equiv P_{\text{in}}-P_{\text{out}}$ is the Laplace pressure across the interface. This can be written in terms of a reference pressure ΔP_0 at $z=0$ and a hydrostatic pressure $\Delta\rho g z$.

The initial derivations of Young [6] and Laplace [7] were based on a force balance, however Gauss [8] later provided an energetic derivation by minimising the free energy of a system. The latter derivation also specifies the possible boundary conditions associated with the three-phase contact between the two phases and the solid surface.

Although many derivations of the Young–Laplace equation exist, we present an energetic derivation using the calculus of variations. We consider the total energy of an axisymmetric interface of the form $z(r)$, where r is the radial direction, and z is directed vertically upwards. For a system to be in equilibrium its energy must be minimised which is ensured when any infinitesimal perturbation to the interface does not change the energy of the system.

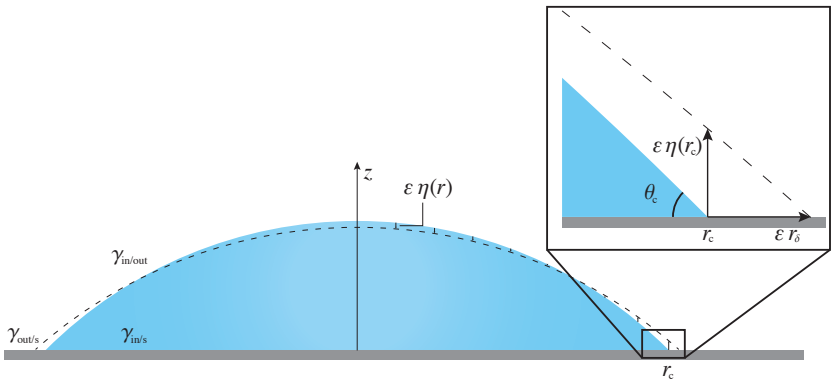

Figure 6.3: Schematic of a drop deposited on a surface, surrounded by a continuous phase. The interfacial tensions are included, together with an infinitesimal functional perturbation $\varepsilon\,\eta(r)$ to the axisymmetric drop interface.

Consider a fixed volume of inner phase V_{in} with density ρ_{in} that sits on a solid surface, surrounded by an outer phase of density ρ_{out}, with the system in thermodynamic equilibrium. The total energy of the system is comprised of two components; the interfacial energy $E_{\text{interfacial}}$ which is the sum of each of the interfacial energy for each interface (in/out, in/S, out/S), together with the gravitational energy $E_{\text{gravitational}}$ of the two phases.

6.3.1 Calculus of variations

We denote the interfacial tension of the inner and outer phases γ, inner phase and the solid $\gamma_{\text{in/S}}$ and the outer phase and the solid $\gamma_{\text{out/S}}$, with associated surface areas $A_{\text{in/out}}$, $A_{\text{in/S}}$ and $A_{\text{out/S}}$, respectively. This leads to the expression for the interfacial energy

$$E_{\text{interfacial}} = \gamma\, A_{\text{in/out}} + \gamma_{\text{in/S}}\, A_{\text{in/S}} + \gamma_{\text{out/S}}\, A_{\text{out/S}} \tag{6.2}$$

$$= 2\pi \int_0^{r_c} \left(\gamma\sqrt{1+z'(r)^2} + \gamma_{\text{in/S}} - \gamma_{\text{out/S}}\right) r\,\mathrm{d}r + \gamma_{\text{out/S}} A_{\text{S}} \tag{6.3}$$

where A_{S} is the total area of the solid surface. Writing the expression eqn (6.3) for the interfacial energy implicitly assumes the contact angle of the drop is less than 90°. If this contact angle was greater than 90°, we must write this in terms of two expressions: an integral from 0 to $r_{\max}$, where $r_{\max}$ is the maximum drop radius, plus an integral from $r_{\max}$ to r_{c}. We therefore restrict this derivation to contact angles less than 90°, however, we note that the result holds for the more general case.

The gravitational energy has two contributions: the gravitational energy associated from the inner fluid and the gravitational energy from the outer fluid. These two contributions lead to an expression for the gravitational energy $E_{\text{gravitational}}$,

$$E_{\text{gravitational}} = \int_{V_{\text{in}}} \rho_{\text{in}} g z\,\mathrm{d}V + \int_{V_{\text{out}}} \rho_{\text{out}} g z\,\mathrm{d}V \tag{6.4}$$

$$= \int_{V_{\text{in}}} \rho_{\text{in}} g z\,\mathrm{d}V - \int_{V_{\text{in}}} \rho_{\text{out}} g z\,\mathrm{d}V + \int_{V_{\text{entire}}} \rho_{\text{out}} g z\,\mathrm{d}V \tag{6.5}$$

$$= \pi \int_0^{r_c} \Delta\rho g z(r) r^2 z'(r)\,\mathrm{d}r + \int_{V_{\text{entire}}} \rho_{\text{out}} g z\,\mathrm{d}V \tag{6.6}$$

where $\Delta\rho \equiv \rho_{\text{in}} - \rho_{\text{out}}$, while the second term is constant and can be regarded as a reference energy. The total energy is the sum of the interfacial and gravitational contributions,

$$E = E_{\text{interfacial}} + E_{\text{gravitational}}. \tag{6.7}$$

We now wish to minimise the free energy subject to the constraint $V = V_{\text{in}}$. To achieve this we introduce the Lagrange multiplier λ, thus forming a function F that we wish to minimise

$$F = E + \lambda(V - V_{\text{in}}), \qquad V = \pi \int_0^{r_c} r^2 z'(r)\,\mathrm{d}r. \tag{6.8}$$

For F to by minimised, all partial derivative must be zero. In particular, $\partial F/\partial\lambda = 0$ enforces the volume constraint. We wish to minimise the energy F with respect to

$z(r)$. This is equivalent to minimising the functional

$$\min_{z(r)} 2\pi \int_0^{r_s} \Phi(r, z, z')\,\mathrm{d}r \tag{6.9}$$

where the function $\Phi(r, z, z')$ is

$$\Phi(r, z, z') \equiv r(\gamma\sqrt{1 + z'(r)^2} + \gamma_{\mathrm{in/S}} - \gamma_{\mathrm{out/S}}) + (\lambda + \Delta\rho g z(r))r^2 z'(r)/2. \tag{6.10}$$

This problem can be solved using the calculus of variations. We consider axisymmetric perturbations to the interface of the form $\varepsilon\,\eta(r)$, for small values of ε. The perturbed functions are

$$z(r) \mapsto z(r) + \varepsilon\,\eta(r), \qquad z'(r) \mapsto z'(r) + \varepsilon\,\eta'(r), \qquad r_\mathrm{c} \mapsto r_\mathrm{c} + \varepsilon\,r_\delta. \tag{6.11}$$

Ensuring the interface meets the surface at the perturbed contact radius gives the condition $z(r_\mathrm{c} + \varepsilon\,r_\delta) = 0$. Expanding to leading order in ε, we have

$$\begin{aligned} z(r_\mathrm{c} + \varepsilon\,r_\delta) &= z(r_\mathrm{c} + \varepsilon\,r_\delta) + \varepsilon\,\eta(r_\mathrm{c} + \varepsilon\,r_\delta) && (6.12)\\ &= z(r_\mathrm{c}) + \varepsilon\,(\eta(r_\mathrm{c}) - r_\delta \tan\theta_\mathrm{c}) + O(\varepsilon^2). && (6.13) \end{aligned}$$

However, $z(r_\mathrm{c}) = 0$, which results in the leading order relation between the contact radius perturbation r_δ and the interface perturbation η,

$$\eta(r_\mathrm{c}) = r_\delta \tan\theta_\mathrm{c}. \tag{6.14}$$

For a system to be in equilibrium, an infinitesimal perturbation to the system does not affect its energy,

$$\left.\frac{\partial E}{\partial \varepsilon}\right|_{\varepsilon=0} = 0. \tag{6.15}$$

Inserting the functional perturbations into the expression for E leads to

$$\begin{aligned} \left.\frac{\partial E}{\partial \varepsilon}\right|_{\varepsilon=0} &= \left.\frac{\partial}{\partial \varepsilon}\left(\int_0^{r_\mathrm{c}+\varepsilon\,r_\delta} \Phi(r, z(r) + \varepsilon\,\eta(r), z'(r) + \varepsilon\,\eta'(r))\,\mathrm{d}r\right)\right|_{\varepsilon=0} && (6.16)\\ &= r_\delta\,\Phi(r, z(r_\mathrm{c})), z'(r_\mathrm{c})) + \int_0^{r_\mathrm{c}} \left(\eta(r)\frac{\partial \Phi}{\partial z} + \eta'(r)\frac{\partial \Phi}{\partial z'}\right)\,\mathrm{d}r. && (6.17) \end{aligned}$$

Integration by parts, together with eqn (6.14), results in the equilibrium condition

$$\int_0^{r_\mathrm{c}} \eta(r)\left\{\frac{\partial \Phi}{\partial z} - \frac{d}{dr}\left(\frac{\partial \Phi}{\partial z'}\right)\right\}\,\mathrm{d}r + \eta(r_\mathrm{c})\left(\frac{\Phi(r_\mathrm{c}, z(r_\mathrm{c}), z'(r_\mathrm{c}))}{\tan\theta_\mathrm{c}} + \left.\frac{\partial \Phi}{\partial z'}\right|_{r_\mathrm{c}}\right) = 0.$$

This expression must be zero for all functional perturbations η, thereby setting

both the first and second expressions to zero. For the first expression to be zero for all perturbations η, the term inside the braces must be identically zero, leading to the Euler–Lagrange equation

$$\frac{\partial \Phi}{\partial z} - \frac{d}{dr}\left(\frac{\partial \Phi}{\partial z'}\right) = 0 \tag{6.18}$$

while the second term must also be zero,

$$\eta(r_\mathrm{c})\left(\frac{\Phi(r_\mathrm{c}, z(r_\mathrm{c}), z'(r_\mathrm{c}))}{\tan\theta_\mathrm{c}} + \left.\frac{\partial \Phi}{\partial z'}\right|_{r_\mathrm{c}}\right) = 0. \tag{6.19}$$

Finally, the functional derivatives of Φ are

$$\frac{\partial \Phi}{\partial z} = \frac{\Delta\rho g r^2 z'}{2} \tag{6.20a}$$

$$\frac{\partial \Phi}{\partial z'} = \gamma r \frac{z'}{\sqrt{1+z'^2}} + \frac{(\lambda + \Delta\rho g z) r^2}{2} \tag{6.20b}$$

$$\frac{d}{dr}\left(\frac{\partial \Phi}{\partial z'}\right) = \gamma \frac{z'}{\sqrt{1+z'^2}} + \gamma r \frac{z''}{\sqrt{(1+z'^2)^3}} + (\lambda + \Delta\rho g z) r + \frac{\Delta\rho g r^2 z'}{2}. \tag{6.20c}$$

6.3.2 Axisymmetric Young–Laplace equation

Substituting the expressions for the functional derivatives from eqn (6.20) into the Euler–Lagrange equation (6.18) leads to the axisymmetric Young–Laplace equation

$$\gamma\left(\frac{z'}{r\sqrt{1+z'^2}} + \frac{z''}{\sqrt{(1+z'^2)^3}}\right) = -\lambda - \Delta\rho g z. \tag{6.21}$$

From trigonometry, the term in brackets is the sum of the reciprocals of the meridional and azimuthal radii of curvatures. At the drop apex these two curvatures are equal, which sets the left hand side to be $2\gamma/R_0$, where R_0 is the radius of curvature at the drop apex. This is simply the Laplace pressure, and thus taking the reference height to be zero at the drop apex gives $-\lambda \equiv \Delta P_0$. Combining the two terms on the left hand side of the above expression leads to the axisymmetric Young–Laplace equation

$$\frac{\gamma}{r}\frac{d}{dr}\left(\frac{r z'}{\sqrt{1+z'^2}}\right) = \Delta P_0 - \Delta\rho g z. \tag{6.22}$$

6.3.3 Three-phase contact conditions

When three mutually immiscible phases all meet, a three-phase contact line is formed. Using the magnitudes of the respective interfacial tensions, a Neumann triangle can be constructed, which determines each of the three contact angles between liquid pairs.

For the case where one of the phases is a solid, two possibilities arise. If the surface is both geometrically and chemically homogenous, the contact line will be free to move along the surface. In this ideal case, the free energy associated with the surface can be considered, determining the contact condition for which the free energy is minimised. Alternatively, if the surface is not ideal, the contact line may remain at a fixed position. This case is known as contact line pinning. When the contact line remains pinned, the system is prevented from achieving a global energy state due to a thermodynamic 'energy barrier'.

From the previous energetic minimisation, we found two terms had to independently be zero. The first term resulted in the Young–Laplace equation, while the second term can be used to determine the boundary condition. The condition

$$\eta(r_\mathrm{c}) \left(\frac{\Phi(r_\mathrm{c}, z(r_\mathrm{c}), z'(r_\mathrm{c}))}{\tan\theta_\mathrm{c}} + \left.\frac{\partial \Phi}{\partial z'}\right|_{r_\mathrm{c}} \right) = 0 \tag{6.23}$$

leads to two possible boundary conditions. Either $\eta(r_\mathrm{c}) = 0$ or the term in brackets is zero.

Young–Dupré equation

If the contact line is free to move, the perturbed height $\eta(r_\mathrm{c})$ need not be zero, and so the 'natural' boundary condition, arising from the preceding calculus of variations, is enforced. This specifies the contact angle in terms of the three associated interfacial tensions. Inserting $z(r_\mathrm{c}) = 0$ and $z'(r_\mathrm{c}) = -\tan\theta_\mathrm{c}$, together with eqn (6.20), into eqn (6.23) leads to the Young–Dupré equation,

$$\gamma\cos\theta + \gamma_{\mathrm{in/S}} - \gamma_{\mathrm{out/S}} = 0. \tag{6.24}$$

As with the Young–Laplace equation, this condition can be derived using a force balance, equating the horizontal components of the interfacial tensions.

Pinned contact line

For the case where the surface is not homogeneous, the contact line may not be free to move. This is known as contact line pinning. Pinning may be the result of surface imperfections, or may be a desired property achieved by treating regions of the surface differently, for example Janus particles. When a contact line is pinned the Young–Dupré equation will not hold, and the resulting interface need not be axisymmetric.

If the contact line is axisymmetric, the energetic analysis considered earlier holds, thereby requiring eqn (6.23) to be zero. However, since the contact line is pinned, $z(r_\mathrm{c}) = 0$, leading to the essential boundary condition $\eta(r_\mathrm{c}) = 0$.

In reality, many surfaces will experience pinning to some degree. For a moving contact line (*i.e.* the contact line associated with an evaporating drop), it is possible that the three-phase contact line will alternate between both constant contact angle and pinned contact line. This property was investigated in Chapter 3.

Neumann triangle

The final contact condition occurs when three mutually immiscible fluids form a three-phase contact. In this case the interface is free to move. The contact angles can be determined using Neumann's construction, which can be interpreted as a force balance of the three interfacial tensions as shown in Fig. 6.4.

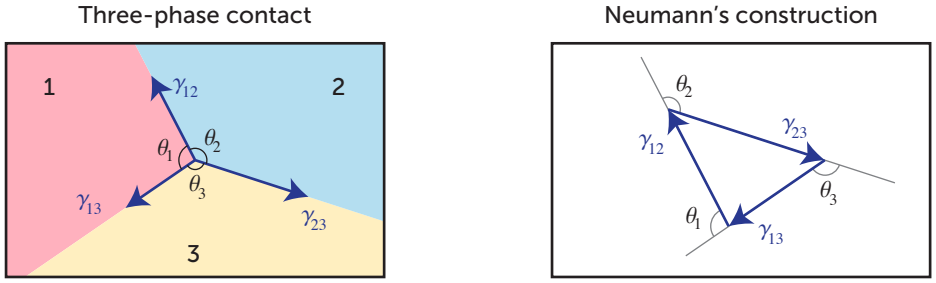

Figure 6.4: Schematic of the three-phase contact between three immiscible fluid interfaces. Left side: Contact angles and interfacial tensions for each of the three phases are shown. Right side: Neumann's construction determines the three contact angles from interfacial tensions and basic trigonometry.

For the case where Neumann's triangle cannot be constructed, a three-phase contact cannot form. Energetically, this results in an interesting phenomena where two interfaces are energetically more favourable than a single interface. For example, if $\gamma_{12} > \gamma_{13} + \gamma_{23}$, the interfacial energy is minimised when a thin film of phase 3 separates phases 1 and 2. This phenomena was investigated in Chapter 2.

6.3.4 The Bond number and capillary length

Physically, interfacial forces act to minimise the total interfacial energy γA, where A is the interfacial area, while gravitational forces act as a hydrostatic pressure through the drop. The relative magnitude of these two competing forces determine to what extent the drop is deformed by gravitational forces.

In order to be able to determine the extent of interfacial deformations, we introduce the Bond number Bo, which is the ratio of body forces to interfacial forces. The body force is typically the force due to gravity, and thus the associated Bond number is

$$\mathrm{Bo} = \frac{\Delta\rho g L_\mathrm{c}^2}{\gamma} \equiv \left(\frac{L_\mathrm{c}}{\lambda_\mathrm{c}}\right)^2 \tag{6.25}$$

where we have also introduced the capillary length λ_c, defined as

$$\lambda_c = \sqrt{\gamma/\Delta\rho g}. \tag{6.26}$$

Physically, the capillary length represents the length scale at which gravitational forces become sufficient to deform the interface. The capillary length is typically around 2 mm (*i.e.* for an air-water interface the capillary length is $\lambda_c \sim 2.7$ mm).

Scaling the Young–Laplace equation (6.1) by a characteristic length scale L_c results in

$$\frac{1}{\bar{R}_1} + \frac{1}{\bar{R}_2} = 2\bar{H}_0 - \mathrm{Bo}\,\bar{z} \tag{6.27}$$

where the overbar denotes scaled variables, while $H_0 \equiv 1/R_0$ is the mean curvature at height $z = 0$.

Thus, if the length scale L_c is much smaller than the capillary length, then $\mathrm{Bo} \ll 1$ from eqn (6.25), and so the gravitational contribution to eqn (6.27) can be neglected. However, as discussed in Chapter 2 and Chapter 3, although gravity does not deform interfaces in this regime, gravity is still critical in determining compound drop configurations.

In Chapter 5 we show that it is possible to introduce an alternative body force, which introduces an additional Bond number. Through judicious choice of this body force, the resulting configuration can be designed to have advantageous properties.

6.3.5 Axisymmetric Young–Laplace equation

For the special case where an axisymmetric fluid interface is formed, the principal radii of curvature can be expressed in terms of the radial component r and the meridional angle ϕ. The two curvatures can be written

$$\frac{1}{R_1} = \frac{\sin\phi}{r}, \qquad \frac{1}{R_2} = \frac{\mathrm{d}\phi}{\mathrm{d}s} \tag{6.28}$$

where s is the arc length of the interface, measured from the reference height at $z = 0$. All quantities are shown in Fig. 6.5.

Trigonometry gives the relations $\mathrm{d}r = \cos\phi\,\mathrm{d}s$ and $\mathrm{d}z = \sin\phi\,\mathrm{d}s$, and thus the Young–Laplace equation (6.1) can be written as a set of coupled ordinary differential equations

$$\frac{\mathrm{d}\phi}{\mathrm{d}s} = \frac{2}{R_0} - \frac{\Delta\rho g}{\gamma} z - \frac{\sin\phi}{r} \tag{6.29a}$$

$$\frac{\mathrm{d}r}{\mathrm{d}s} = \cos\phi \tag{6.29b}$$

$$\frac{\mathrm{d}z}{\mathrm{d}s} = \sin\phi \tag{6.29c}$$

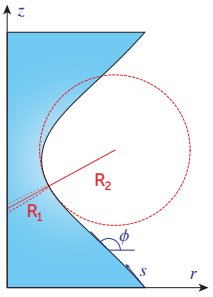

Figure 6.5: A schematic illustrating the principal radii of curvature R_1 and R_2 for an axisymmetric drop satisfying the Young–Laplace equation. The functions r, z and ϕ are expressed in terms of the arc length s.

where $R_0 \equiv 2\gamma/\Delta P_0$ is the Laplace radius of the interface at $z = 0$.

Scaling the axisymmetric Young–Laplace equation by the radius R_0 results in the non-dimensional equations

$$\frac{\mathrm{d}\phi}{\mathrm{d}\bar{s}} = 2 - \mathrm{Bo}\,\bar{z} - \frac{\sin\phi}{\bar{r}} \tag{6.30a}$$

$$\frac{\mathrm{d}\bar{r}}{\mathrm{d}\bar{s}} = \cos\phi \tag{6.30b}$$

$$\frac{\mathrm{d}\bar{z}}{\mathrm{d}\bar{s}} = \sin\phi \tag{6.30c}$$

where the Bond number $\mathrm{Bo} \equiv \Delta\rho g R_0^2/\gamma$ naturally arises. By defining the density difference $\Delta\rho \equiv \rho_{\mathrm{in}} - \rho_{\mathrm{out}}$, and taking the z-axis vertically upwards, we avoid the introduction of a choice of sign.

If the interface is axisymmetric, the three-phase contact conditions at the surface can be written as

$$\phi(0) = \pi - \theta_{\mathrm{c}}, \qquad \bar{r}(0) = \bar{r}_{\mathrm{c}}, \qquad \bar{z}(0) = 0 \tag{6.31}$$

with either θ_{c} being fixed (Young–Dupré equation), or $\bar{r}_{\mathrm{c}}$ being fixed (pinned contact line). Different values of the unfixed quantity correspond to different drop volumes.

6.4 Fitting theory and experiments

Throughout this thesis we considered a variety of compound drop systems both experimentally and theoretically. Where possible, we compared experimental photographs with theoretically predicted interfaces. In addition to demonstrating the applicability of the theory, this enabled important physical quantities to be extracted from an experimental drop profile. The extracted quantities included the Laplace pressure, contact angles, the capillary force, and, in some cases, the particle mass and the interfacial tension of an interface.

We outline the method used to fit the theoretical drop profiles to a given experimental photograph. There are two steps involved in this process: first the experimental drop profile must be extracted from the photograph, and then the theoretical solution must be fitted to the extracted profile. We outline each of these steps separately.

6.4.1 Edge detection

To detect edges for a given experimental photograph we use the Canny edge detection algorithm [9]. This algorithm was developed in 1986 to provide a computational approach to edge detection, based on three criteria:

1. Good detection. The probabilities associated with false positives and false negatives should be low (this condition is equivalent to maximising the signal-to-noise ratio),
2. Good localisation. Detected edges should be as close as possible to the centre of the true edge,
3. Only one response to a single edge.

The Canny edge detector can be derived by finding the optimal mathematical operator for a step edge that satisfies these conditions [9].

6.4.2 Fitting routine

The systems considered throughout rely on solutions to the Young–Laplace equation, which is a non-linear equation. In this section we derive the theory associated with minimising a non-linear function. As a distinction from the least squares methods typically implemented, we minimise the perpendicular residuals rather than the vertical residuals. This is necessary since our data does not have dependant and independent variables. Minimising the perpendicular residuals is equivalent to minimising the Euclidean distance between an experimental point (r_i, z_i) and the theoretical curve (r, z), as illustrated in Fig. 6.6. To avoid ambiguity with the i^{th} radial data point (r_i, z_i) we denote the associated residual e_i.

The objective function that we wish to minimise is the sum of least squares S, defined

$$S = S(\boldsymbol{\beta}) \equiv \sum_{i=1}^{n} e_i^2. \tag{6.32}$$

For a given set of experimental data, the associated residuals depend only on the parameters used to generate the theoretical profile. Thus the objective function S is explicitly a function of the parameters $\boldsymbol{\beta}$.

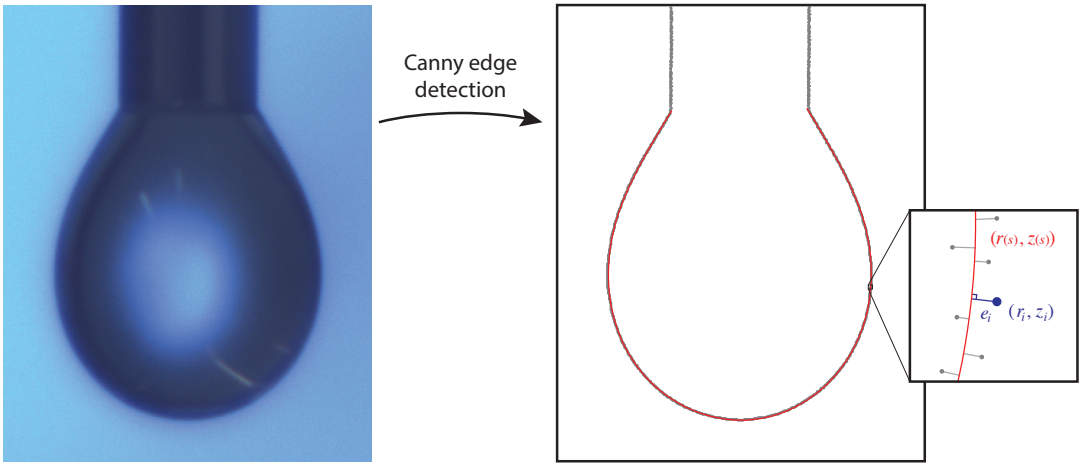

Figure 6.6: An experimental image of a drop is converted to a list of dat points using Canny edge detection. The residual i^{th} residual e_i for the data point (r_i, z_i) is defined as the minimum Euclidean distance between the given data point and the theoretical profile $(r(s), z(s))$.

Fitting the theoretical curve to experimental data is equivalent to minimising the objective function S. To achieve this we implement the non-linear Levenberg–Marquardt–Fletcher algorithm, which is an extension of the Gauss–Newton algorithm. This optimisation procedure is commonly used in pendant drop tensiometry [10]. We provide a derivation of Newton's method, and Gauss' approximation, before detailing the improvements made by Levenberg, Marquardt and Fletcher.

6.4.3 Gauss–Newton algorithm

A well known method to minimise an m-dimensional non-linear function is the Gauss–Newton algorithm. This method is an iterative procedure that updates the parameter set $\boldsymbol{\beta}$ by approximating the objective function with a second order Taylor series. Minimising this approximation then provides an update to the current parameter set. This process iteratively updates the parameter set until convergence.

To derive the algorithm, consider a Taylor series for our objective function, around the current parameter set $\boldsymbol{\beta}$,

$$S(\boldsymbol{\beta}+\boldsymbol{\delta}) = S(\boldsymbol{\beta}) + (\boldsymbol{\nabla}S)^{\mathrm{T}}\,\boldsymbol{\delta} + \frac{1}{2}\boldsymbol{\delta}^{\mathrm{T}}\left(\boldsymbol{\nabla}^2 S\right)\boldsymbol{\delta} + O(\|\boldsymbol{\delta}\|^3) \tag{6.33}$$

$$\simeq S(\boldsymbol{\beta}) + \boldsymbol{v}^{\mathrm{T}}\boldsymbol{\delta} + \frac{1}{2}\boldsymbol{\delta}^{\mathrm{T}}\mathbf{H}\boldsymbol{\delta} \tag{6.34}$$

where we have introduced the Hessian $\mathbf{H} \equiv \boldsymbol{\nabla}^2 S$ and the gradient $\boldsymbol{v} \equiv \boldsymbol{\nabla}S$. Setting the gradient of the approximating quadratic Taylor series of S to zero results in Newton's method, which allows the parameter update $\boldsymbol{\delta}$ to be calculated according

to

$$\mathbf{H}\boldsymbol{\delta} = -\boldsymbol{v}, \tag{6.35}$$

from which the parameter set $\boldsymbol{\beta}$ can be iteratively updated according to

$$\boldsymbol{\beta}^{(k+1)} = \boldsymbol{\beta}^{(k)} + \boldsymbol{\delta}. \tag{6.36}$$

The gradient vector $\boldsymbol{v}$ from eqn (6.35) can be written

$$\boldsymbol{v} \equiv \frac{\partial S}{\partial \beta_j} = \frac{\partial}{\partial \beta_j}\left(\sum_{i=1}^{n} e_i^2\right) = 2\sum_{i=1}^{n} \frac{\partial e_i}{\partial \beta_j} e_i \equiv 2\mathbf{J}^{\mathrm{T}}\boldsymbol{e} \tag{6.37}$$

where repeated indices are implicitly summed over. In addition, we have introduced the residual vector $\boldsymbol{e}$ and the Jacobian matrix $\mathbf{J}$, defined

$$\boldsymbol{e}_i = e_i, \qquad \mathbf{J}_{ij} = \frac{\partial e_i}{\partial \beta_j} \tag{6.38}$$

while the Hessian can also be calculated

$$\mathbf{H} \equiv \frac{\partial^2 S}{\partial \beta_j \partial \beta_k} = 2\sum_{i=1}^{n} \frac{\partial}{\partial \beta_j}\left(\frac{\partial e_i}{\partial \beta_k} e_i\right) \tag{6.39}$$

$$= 2\sum_{i=1}^{n}\left(\frac{\partial e_i}{\partial \beta_j}\frac{\partial e_i}{\partial \beta_k} + e_i \frac{\partial^2 e_i}{\partial \beta_j \partial \beta_k}\right) \tag{6.40}$$

$$\equiv 2\left(\mathbf{J}^{\mathrm{T}}\mathbf{J} + \mathbf{Q}\right), \tag{6.41}$$

where $\mathbf{Q}$ is the matrix of second derivatives, with $\mathrm{Q}_{jk} \equiv e_i\, \partial^2 e_i / \partial \beta_j \partial \beta_k$.

The method outlined above is Newton's method. Gauss approximated the full Hessian by neglecting the matrix of second order derivatives, $\mathbf{Q}$. This approximation is valid when

$$\left| e_i \frac{\partial^2 e_i}{\partial \beta_j \partial \beta_k} \right| \ll \left| \frac{\partial e_i}{\partial \beta_j}\frac{\partial e_i}{\partial \beta_k} \right| \tag{6.42}$$

which is ensured provided at least one of the following conditions is met:

1. the residuals e_i are small — a condition that can be reasonably expected to hold near the minimum, or
2. the function S is only "mildy" non-linear.

Under these assumptions the Hessian $\mathbf{H}$ can be approximated by

$$\mathbf{H} \simeq 2\mathbf{J}^{\mathrm{T}}\mathbf{J}. \tag{6.43}$$

Finally, inserting the above approximation to the Hession into eqn (6.35) and rear-

ranging gives the Gauss–Newton algorithm for $\boldsymbol{\delta}$,

$$\left(\mathbf{J}^{\mathrm{T}}\mathbf{J}\right)\boldsymbol{\delta} = -\mathbf{J}^{\mathrm{T}}\boldsymbol{e}. \tag{6.44}$$

This method is much less computationally expensive as it requires the computation of n first order derivatives, compared with an additional n^2 second order derivatives required to calculate the full Hessian. Thus, provided the approximation is valid, the Gauss–Newton method is more efficient than the full Newton method, while retaining the same convergent behaviour.

Convergence

The parameters $\boldsymbol{\beta}^{(k)}$ can be updated according to eqn (6.36) and (6.44) until convergence. There are three convergence criteria:

i. convergence in the objective function, $S/(n-m+1) < \mathrm{tol}_1$
ii. convergence in the parameters, $\max_j |\beta_j^{(k+1)} - \beta_j^{(k)}| < \mathrm{tol}_2$
iii. convergence in the gradient, $\max_j |\mathrm{J}_{ij}^{\mathrm{T}}\, e_i| < \mathrm{tol}_3$

with the addition of a maximum number of allowed iterations.

6.4.4 Levenberg–Marquardt–Fletcher algorithm

When the Gauss-Newton algorithm converges, its convergence is rapid, however, it may diverge. An alternative algorithm is the method of steepest descent. This method provides greater stability in convergence, while sacrificing speed. Parameters are updated according to the direction in which the objective function decreases most rapidly (*i.e.* the negative of the gradient of the objective function, $-\mathbf{J}^{\mathrm{T}}\boldsymbol{e}$).

Levenberg, Morrison and Marquardt's method

An alternative method to Gauss–Newton was independently proposed by Levenberg [11] and Morrison [12]. The method was later extended by Marquardt [13], and we will follow his motivation.

Although the Gauss–Newton method achieves quadratic convergence, it may not converge if the initial guess is poor. By introducing a term $\lambda\,\mathbf{I}$ into the Gauss–Newton algorithm, eqn (6.44)

$$\left(\mathbf{J}^{\mathrm{T}}\mathbf{J} + \lambda\,\mathbf{I}\right)\boldsymbol{\delta} = -\mathbf{J}^{\mathrm{T}}\boldsymbol{e}, \tag{6.45}$$

where λ is an adjustable parameter, Levenberg proposed a method that essentially interpolates between Gauss–Newton and steepest descent. Clearly for $\lambda = 0$, this

method reduces to Gauss–Newton, while for large values of λ, this method approaches

$$\lambda\,\boldsymbol{\delta} = -\mathbf{J}^{\mathrm{T}}\boldsymbol{e} \tag{6.46}$$

which is a step parallel to the steepest descent. The value of λ is iteratively updated, based on the convergence behaviour of the objective function S.

Although the method of steepest descent has greater stability compared to Gauss–Newton, it is sensitive to poor scaling [14]. For this reason Marquardt replaced the identity matrix $\mathbf{I}$ with the diagonal matrix of the approximating Hessian, $\mathrm{diag}(\mathbf{J}^{\mathrm{T}}\mathbf{J})$, thereby scaling the problem. The equation that determines the step $\boldsymbol{\delta}$ is now

$$\left(\mathbf{J}^{\mathrm{T}}\mathbf{J} + \lambda\,\mathrm{diag}(\mathbf{J}^{\mathrm{T}}\mathbf{J})\right)\boldsymbol{\delta} = -\mathbf{J}^{\mathrm{T}}\boldsymbol{e}. \tag{6.47}$$

The final requirement for the routine is to outline criteria to choose the value of λ. Marquardt provided a simple method for updating the value of λ at each step, based on the whether the objective function S reduces. Marquardt's method was to initialise the value of λ to be small (he suggested $\lambda = 0.01$). At each step, the objective function $S^{(k)}$ is compared to the previous value $S^{(k-1)}$. The value of λ is then multiplied by either ν or $1/\nu$, depending on whether the objective function had increased or decreased, respectively. Marquardt suggested the value of the multiple $\nu = 10$.

There are two issues associated with this procedure. First, if the Gauss–Newton algorithm is initially poor, several steps may be required before λ is sufficiently large to allow the system to step in a direction that reduces S. Second, since λ is always greater than zero the algorithm is prevented from converging according to the Gauss–Newton algorithm, resulting in a convergence rate is super-linear, compared with quadratic convergence from Gauss–Newton [15].

Fletcher's refinement

Fletcher improved on Marquardt's criteria for updating λ by comparing the reduction in S, with the theoretically predicted reduction if the algorithm was converging as predicted by Gauss–Newton [15].

Fletcher's implementation also includes a series of computational improvements in efficient resource management, while designing an algorithm that sparingly calculates computationally expensive quantities. For many non-linear data fitting problems, the number of data points n may be quite large (for our systems $n \sim 2000$), while the number of parameters that are being used in the fit are comparatively small (for our systems $m \leq 8$), such that $m \ll n$. This results in a large Jacobian $\mathbf{J}$, which has dimensions $m \times n$. However the Jacobian is only used to calculate two quantities, $\mathbf{A} = \mathbf{J}^{\mathrm{T}}\mathbf{J}$ and $\boldsymbol{v} = \mathbf{J}^{\mathrm{T}}\boldsymbol{e}$, which have much smaller dimensions, $m \times m$ and

$m \times 1$, respectively. Computationally, these two quantities can be evaluated within a `for` loop without having to explicitly calculate $\mathbf{J}$, vastly reducing the storage requirements.

Fletcher's major improvement was to provide a systematic method for updating the value λ. In his method, he introduced the ratio R of the actual reduction in the objective $S - S'$ to the predicted reduction from eqn (6.34),

$$R = \frac{S - S'}{-2\boldsymbol{\delta}^{\mathrm{T}}\boldsymbol{v} - \boldsymbol{\delta}^{\mathrm{T}}\mathbf{A}\boldsymbol{\delta}}. \tag{6.48}$$

This ratio quantifies the rate of convergence for the algorithm. By comparing this rate to two predetermined values ρ and σ (with $0 < \rho < \sigma < 1$), Fletcher is able to determine if the convergence is sufficiently rapid, $R > \sigma$, or whether convergence is poor, $R < \rho$. If the convergence is sufficiently rapid ($R > \sigma$), the value of λ is reduced by a factor of 2, while if the convergence is poor ($R < \rho$), the value of λ is increased. For intermediate convergence rates ($\rho \leq R \leq \sigma$), the value of λ is left unchanged. Fletcher suggests taking $\rho = 0.25$ and $\sigma = 0.75$, but notes the rate of convergence is largely insensitive to these values.

For the case where the convergence is poor ($R < \sigma$), Fletcher updates λ through a clever quadratic interpolation of the objective function S in the direction of the predetermined quantity $\boldsymbol{\delta}$. The interpolation function $\phi(\alpha) \equiv S(\boldsymbol{\beta} + \alpha\boldsymbol{\delta})$ is straightforward to calculate, since $\phi(0) = S$, $\phi(1) = S'$ and $\phi'(0) = \boldsymbol{\delta}^{\mathrm{T}}\boldsymbol{v}$ are all known. Minimising with respect to α then gives the optimal step size based on this interpolation,

$$\alpha = \frac{1}{2 - (S' - S)/(\boldsymbol{\delta}^{\mathrm{T}}\boldsymbol{v})}. \tag{6.49}$$

Fletcher uses this to form the multiple $\nu \equiv 1/\alpha$ that is used to update λ. This multiple is replaced by 2 or 10 if it is less than 2 or greater than 10, respectively.

The final improvement of Fletcher is the introduction of a 'cut-off' value λ_{c}, below which λ is set to zero, thereby allowing the algorithm to adopt the complete Gauss–Newton algorithm. Fletcher provides a theoretical justification for the choice of λ_{c} to be the reciprocal of the smallest eigenvalue of $\mathbf{A}^{-1}$. As this is computationally expensive, he uses an underestimate $\|\mathbf{A}^{-1}\|_{\infty}$

$$\lambda_{\mathrm{c}} = \frac{1}{\|\mathbf{A}^{-1}\|_{\infty}} \equiv \frac{1}{\max|\mathbf{A}^{-1}|}. \tag{6.50}$$

and only calculates this when λ is increased from zero. The complete Levenberg–Marquardt–Fletcher algorithm is illustrated in Fig. 6.7 (adapted from Fletcher [15]).

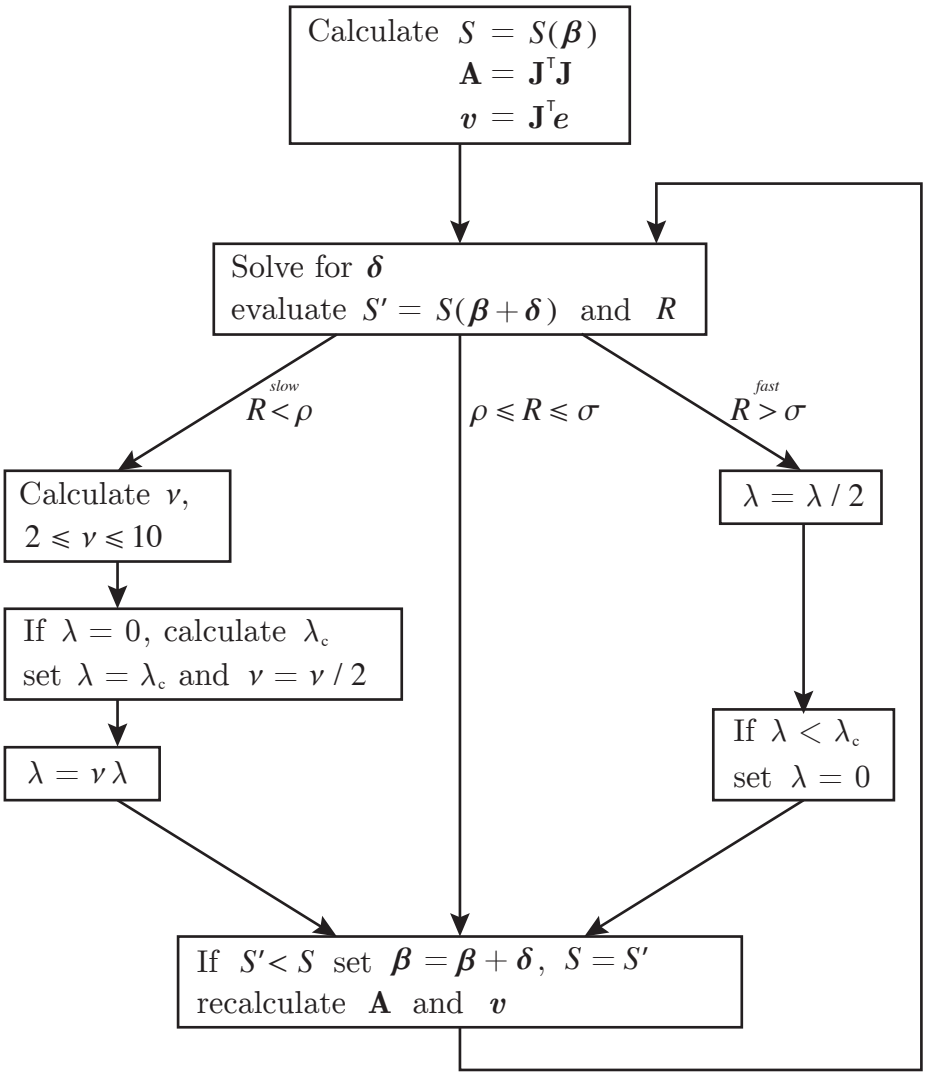

Figure 6.7: Flow chart for the Levenberg–Marquardt–Fletcher algorithm. When $R > \sigma$, convergence is rapid resulting in a smaller value of λ, biasing the system towards the Gauss–Newton algorithm, whereas for poor convergence, $R < \rho$, the value of λ is increased, thereby biasing the system towards steepest descent. Adapted from Fletcher [15].

6.5 Bibliography

[1] J. W. Gibbs, *Trans. Conn. Acad. Arts Sci.*, 1974–1978, **3**, 343–520.

[2] J. W. Gibbs, *The Collected Works of J. Willard Gibbs*, Longmans, Green and Company, 1928, vol. 1.

[3] E. A. Guggenheim, *Trans. Faraday Soc.*, 1940, **35**, 397–412.

[4] E. A. Guggenheim, *Thermodynamics: an advanced treatment for chemists and physicists*, North-Holland Physics Publishing, 7th edn., 1985.

[5] H.-J. Butt, K. Graf and M. Kappl, *Physics and Chemistry of Interfaces*, John Wiley & Sons, 2003.

[6] T. Young, *Phil. Trans.*, 1805, **95**, 65–87.

[7] P. S. Laplace, *Traité de Mécanique Céleste*, de l'Imprimerie de Crapelet, 1805, vol. 4.

[8] C. F. Gauss, *Principia generalia Theoriae Figurae Fluidorum in statu Aequilibrii*, Göttingen, Dieterichs, 1830.

[9] J. Canny, *IEEE T. Pattern Anal.*, 1986, 679–698.

[10] O. I. del Río and A. W. Neumann, *J. Colloid Interface Sci.*, 1997, **196**, 136–147.

[11] K. Levenberg, *Q. Appl. Math.*, 1944, **2**, 164–168.

[12] D. D. Morrison, *Methods for nonlinear least squares problems and convergence proofs*, Space Technology Labs., Inc., Los Angeles, CA, United States technical report, 1960.

[13] D. W. Marquardt, *J. Soc. Ind. Appl. Math.*, 1963, **11**, 431–441.

[14] S. Wright and J. Nocedal, *Numerical optimization*, Springer New York, 1999.

[15] R. Fletcher, *A modified Marquardt subroutine for non-linear squares*, Atomic Energy Research Establishment, Harwell (England) technical report, 1971.

CHAPTER 7

Conclusion

In this thesis, we have provided a comprehensive analysis of a variety of compound drop systems. Two compound drop systems were considered in depth: (i) a compound drop comprised of two immiscible phases that is immobilised on a solid surface, surrounded by a third mutually immiscible phase, and (ii) a spherical particle attached to an immobilised drop surrounded by an immiscible phase. For each of these systems, we investigated the possible configurations available both theoretically and experimentally, and observed good agreement between the two.

It was shown that the interfacial tension is extremely important in determining the configurational behaviour of each of these compound drops. Given its importance, we discussed a variety of commonly used interfacial tensiometry techniques, before providing a comprehensive derivation of the pendant drop method. Finally, we showed that the accuracy of the method decreased when the interfacial forces dominated gravitational forces.

In the final work we developed a new technique to measure the interfacial tension by analysing the profile of a compound pendant drop formed by attaching a spherical particle to a pendant drop. Fitting the presented theory to an experimental photograph determines the interfacial tension. Importantly, this technique circumvented the physical limitations associated with the conventional pendant drop method.

We now provide a discussion of the conclusions drawn from the work.

7.1 Conclusions

Compound sessile drops

When a compound drop of fluid is sessile on a solid surface, a compound sessile drop is formed. In Chapter 2 we investigated these configurations in the limit where the drop dimensions are much smaller than their capillary lengths. In this regime, gravitational forces are insufficient to deform the interface, however it was shown that gravitational forces are crucial in determining the resulting configuration of the system.

By considering the possible solutions to the Young–Laplace equation, we have shown that these compound drops form one of four distinct configurations. We derived a solution to each of these configurations, thereby providing a theoretical framework for these drops.

By comparing a series of experimentally observed drop profiles with the theoretically predicted profiles, we demonstrated the accuracy and applicability of this theoretical framework. Furthermore, we demonstrated that important physical quantities could be extracted from the fitted profiles, such as the Laplace pressure across the interface, the volume of the collar and the interfacial areas, together with the contact angles at the surface.

In addition, an interfacial energy phase plot was presented that demonstrated the configurational dependence on the relative magnitude of the interfacial tensions.

This work has shown that although compound micro-drops are comparatively easy to produce, they exhibit a wide range of geometries and behaviours. Importantly, despite gravitational forces being much smaller than interfacial forces, the gravitational forces play a crucial role in determining the configurations of these drops.

Particle-drop-substrate systems

Chapter 3 investigated the configurations available to particle-drop-substrate systems formed when a particle is added to the interface of a sessile or pendant drop on a solid surface. As with the previous chapter, we investigated these configurations in the limit where the drop dimensions were well below the capillary length (*i.e.* low Bond number), resulting in interfaces that are not deformed by gravity.

By developing an appropriate theoretical model, we were able to easily predict the energetically preferred configuration for these drops, based on the associated fluid and particle densities, contact angles and volume ratios.

In each experiment the supporting water drop was allowed to evaporate over time. A series of time-lapse photographs were obtained from this process. Fitting

the presented theory to the experimental photographs allowed the configurational behaviour to compared with the theoretical model for varying drop volumes. Furthermore, we were able to extract important physical quantities that provide significant insight into the underlying physics associated with these drops.

Significantly, for all of the systems presented, a critical drop volume was determined, below which an axisymmetric collar configuration formed which applied a strongly attractive capillary force to the particle. This capillary force was shown to be three orders of magnitude larger than the weight of the particle.

As in Chapter 2, we show that although the Bond number is very small, with interfacial forces dominating gravitational forces, gravity still plays an important role in determining the configuration of the system. This was further demonstrated through surface orientation, where we showed that a silica particle sits at the lowest possible position (*i.e.* either sitting axisymmetrically at the apex of a pendant drop, or asymmetrically at the solid surface for a sessile drop).

Interfacial tensiometry

The final two chapters investigated interfacial tensiometry. Chapter 4 discussed a variety of different methods used to measure the interfacial tension. One particularly appealing method is the pendant drop tensiometer, as it is widely applicable, very accurate and requires a simple experimental setup. In this method, the interfacial tension is determined by equating the gravitational forces that act to deform a drop, with the interfacial forces that act to minimise the interfacial area.

We provided a detailed derivation of the expressions required to implement this method and demonstrated its applicability. We then discussed the major physical limitation associated with this technique—the decreases in sensitivity in the low Bond number regime.

Compound pendant drop tensiometry

In Chapter 5 we again consider a spherical particle attached to a pendant drop, revisiting the work presented in Chapter 3. In this later work we relax the small Bond number limit resulting in a drop that is deformed by gravity. By providing a careful theoretical analysis of the resulting configuration we are able to perform interfacial tensiometry in the limit of zero Bond number, thereby circumventing the inherent physical limitation associated with pendant drop tensiometry, presented in Chapter 4. We demonstrate the applicability of this method with four experimental systems.

In conventional pendant drop tensiometry, the zero Bond number limit is a physical constraint that cannot be overcome by improving the measurement preci-

sion. The attachment of a particle to a pendant drop, together with appropriate theoretical modelling, creates a compound pendant drop tensiometer that provides a simple and accurate method to measure the interfacial tension at low and zero Bond number.

This extends the region of applicability of the pendant drop method, enabling accurate interfacial tension measurements for interfaces between fluids of comparable densities, or for much smaller liquid sample sizes.

7.2 Further work

The work presented in Chapter 2 and Chapter 3 investigated the shape of compound drops with dimensions much less than the capillary length, or equivalently, drops in the limit of zero Bond number. In this limit, gravitational forces are insufficient to deform the interface. While the particle-pendant drop system presented in Chapter 3 has been extend to non-zero Bond number in Chapter 5, the case where the compound drop is comprised of two immiscible fluids as shown in Chapter 2 has not. Extending the multiphase theory to this regime may prove useful.

The compound pendant drop tensiometer presented in Chapter 5 provides a simple and accurate method to determine the interfacial tension of an interface in the limit of small drop Bond number. There are, however, several aspects of this method that would benefit from more experimental and theoretical examination.

Like the pendant drop tensiometers considered in Chapter 4, this method fits a theoretical solution to an experimental drop profile to measure interfacial tension and particle density. A detailed analysis of the uncertainties associated with the extracted parameters is of fundamental importance in the application of such a tensiometer. The uncertainties associated with the fitting routine arise from both the edge detection and the accuracy of the fitting routine. Exploring the error associated with determining the position of the interface and the statistical analysis of the residuals would facilitate a complete understanding of the uncertainties associated with the compound pendant drop tensiometer.

It would be advantageous to benchmark this new technique with respect to the physical quantities associated with the compound drop, such as the size and mass of the attached particle, the volume of the pendant drop and the interfacial tension. This would be particularly useful to experimentalists if design rules could determine the optimal particle size and density to ensure accurate interfacial tensiometry.

Throughout this work, we extracted compound drop profiles from experimental photographs which we then used in fitting our presented theory. To achieve this we implemented the Canny edge detection algorithm. However, there are a variety of alternative routines which may offer some improvements.

Conceptually, this method applies a known force to a drop and then equates this to the capillary force, as determined from the drop profile. This capillary force contains a single unknown quantity, the interfacial tension γ. Although the applied force in this work was the weight of a spherical particle, the theory presented is sufficiently general to incorporate alternative forces, provided the resulting drop profile is axisymmetric. Investigating other applied forces may provide additional advantages.

The conventional pendant drop method is a simple method that can be used to determine the interfacial tension. In this work we have derived the routines required to implement this method, enabling the method to be performed with standard laboratory equipment. More generally, this work has fitted the Young–Laplace equation to a variety of drop profiles to extract important physical quantities. In addition to the interfacial tension, we were able to accurately quantify the Laplace pressure across an interface, as well as drop volumes, interfacial areas, contact conditions and the capillary force. As we have shown, this offers significant quantitative insight into the physics of compound drops and related phenomena.

As such, it would be extremely valuable to disseminate this material openly. We intend to make the routines developed in this thesis accessible and open source.

7.3 Concluding remarks

This work has laid the theoretical foundations for the quantitative study of compound immiscible fluid systems. Throughout the thesis, the agreement between the theoretically predicted and experimentally observed drop profiles was very good. Fitting the presented theory to each of the experiments facilitated important physical quantities to be extracted from experimental photographs. This in turn has provided significant insight into the underlying physics associated with compound drop systems. Finally, by developing a theoretical model for the shape of a compound pendant drop, we developed a simple, elegant method to determine the interfacial tension for systems currently inaccessible to pendant drop tensiometers.